

博士論文

Dynamic Acoustic Manipulation of
Macroscopic Objects and Its Applications

(空中超音波による巨視的物体の
動的 3次元制御技術とその応用)

古本 拓朗

Copyright © 2020, Takuro Furumoto.

Acknowledgment

First of all, I would like to thank my advisor Hiroyuki Shinoda. He gave me an opportunity to work on this exciting research. He always makes time to discuss research directions even though he is very busy. His advice often helps me concentrate on important problems instead of trivial matters. I was impressed by his dedication to achieving great and meaningful works.

I would like to thank prof. Yasutoshi Makino for a lot of advice, especially on applications and interactions. I respect him for his wide variety of novel and interesting ideas, which gave me a lot of insights. He also kindly encouraged me to submit my work to academic conferences and demos.

I would like to thank prof. Takeshi Imamura, prof. Takeshi Morita, and prof. Hiroshi Kori for serving on my thesis committee. Their feedback has made my thesis sound.

I would like to thank Masahiro Fujiwara. He advised me a lot in many aspects including technical matters, presentation techniques, and so on. I also thank him for his effort in laboratory management to improve productivity. Thanks to his effort, many events such as group meetings, lecture programs, and mentoring programs went smoothly.

I would like to thank Keisuke Hasegawa, who is currently an assistant professor at Nara laboratory, the University of Tokyo, for discussing research ideas. That helped me organize my thoughts, gave me new points of view, and encouraged me so much.

I would like to express my gratitude to the members of Shinoda Makino laboratory. They not only gave me a lot of advice from their own perspectives but also made my research life in the Kashiwa campus enjoyable. Especially I would like to

ii Acknowledgment

thank: Thanks to their friendliness, I was able to get used to Shinoda Makino laboratory in a short time. I also learned from them how to enjoy difficult situations in research life. I thank Yuichi Masuda, who is a project researcher, for taking us to restaurants for lunch. I really enjoyed the foods and talks at lunchtime. I thank Takaaki Kamigaki, who is currently a project researcher. He introduced nice restaurants around the Kashiwa campus. In addition, I have learned from him to have humor in tough situations. I thank Shun Suzuki, who is currently a doctoral student. I was impressed by his speed of learning and augmenting the meme of Shinoda Makino lab. He also animated our communications in Slack. I hope the talent be used in a correct and quiet manner. I thank Yutaro Toide and Takumi Kasai, with whom I collaborated as a part of mentoring programs. Mr. Toide developed a virtual reality software for the encounter-type haptic display application. Mr. Kasai developed an acoustic direction control system of a planar object, which is referred to as the future work. They also helped me run demos.

I would like to thank Ms. Yasuko Konagai. Her support makes my research life comfortable, allowing me to concentrate on my research.

Finally, I would like to thank my family: Hiroyuki, Nanayo, and Tetsuro Furumoto for years of support and encouragement.

This research was supported by JSPS KAKENHI Grant Number JP18J13314 during the last two years.

Abstract

In this thesis, the author proposes a dynamic acoustic manipulation system for macroscopic light-weight spheres whose dimensions are much larger than the wavelength of the sound, within a human-scale workspace.

The author envisions non-contact manipulation of such scale will open up new applications such as a three-dimensionally controllable floating display, an externally actuated aerial robot, and a structure-less manipulator in a microgravity environment.

In contrast to conventional acoustic manipulations, which stabilizes an object in the air by generating an acoustic *trap*, our manipulation method stabilizes it dynamically using sensor-feedback control of acoustic fields. The proposed method demonstrated manipulation of spheres of 20 cm diameter at a height of more than one meter.

Manipulation by single-sided arrays is also demonstrated. This provides its lateral scalability of the workspace and good visual and haptic access to the floating object.

As an application system, we developed a floating display system and an encounter-type haptic feedback system. The floating display can present an image in an arbitrary three-dimensional position in full-body spatial augmented reality applications. It projects an image onto a helium-filled balloon that is manipulated using the dynamic acoustic manipulation system. Because the total power is supplied from the environment, this system has a long operational time, which is limited only by the helium loss. This feature allows it to present static objects in the air such as menus, icons, and avatars in a calm manner.

Contents

Acknowledgment	i
Chapter 1 Introduction	1
1.1 Background and Motivation	1
1.2 Related Works	3
1.3 Organization	7
Chapter 2 Acoustic Radiation Force Model	9
2.1 Physics of Acoustic Radiation Force	9
2.2 Airborne Ultrasound Phased Array (AUPA)	12
2.3 Acoustic Radiation Force Model for Macroscopic Sphere	16
2.4 Analysis on Plane Wave Beam: Experimental Approach	25
Chapter 3 Balancing Control by Multiple Phased Array Units	28
3.1 Dynamics	28
3.2 Control	30
3.3 Manipulation Experiment	36
3.4 Discussion	39
Chapter 4 Manipulation by Single-sided Array for Scalable Workspace	47
4.1 Design of Lattice	47
4.2 Manipulation of Multiple Objects	53
4.3 Translation Maneuver Experiment	54
Chapter 5 Floating Balloon Display for Body-scale Augmented Reality	58

5.1	Background and Motivation	58
5.2	System Overview	61
5.3	Tracking System	61
5.4	Natural User Input System	66
5.5	Projection System	66
5.6	Stereoscopic Image Rendering	71
5.7	Preliminary Experiment on Visibility	73
5.8	Demo at Siggraph Asia 2019	76
5.9	Application Scenarios	77
5.10	Discussion	79
Chapter 6	Encounter-type Haptic Feedback System Using an Acoustically Manipulated Floating Object	81
6.1	Background	81
6.2	System Configuration	82
Chapter 7	Conclusion	84
7.1	Summery of Contributions	84
7.2	Future Works	85
	Bibliography	88

List of Figures

1.1	Application scenarios.	3
1.2	Noncontact versatile manipulator for microgravity environment.	4
1.3	Schematic illustration of dynamic acoustic manipulation.	4
2.1	Waveform synthesis by airborne ultrasound phased array	14
2.2	Appearance of the aerial ultrasonic phased array.	14
2.3	Input voltage to transducers.	14
2.4	Plane wave incident on a planar surface.	15
2.5	Calculation of acoustic radiation pressure on a macroscopic sphere based on ray-acoustics. (Left) Step1: Wave propagation to focal plane. (Right) Step2: Calculation of acoustic radiation pressure based on geometric reflection of incident ray of intensity I	17
2.6	Comparison of ARF calculation results based on ray-acoustics approach and wave-acoustics approach for absorption coefficient (Upper: 0 Neper/m. Middle: 0.3 Neper/m. Lower: 0.5 Neper/m).	18
2.7	Geometric Relationship among incident points and reflection angles of the incident acoustic rays.	21
2.8	Comparison of ray-acoustics-based model and measured value (Upper): Pressure field is numerically propagated considering the directivity of the transducers. (Lower): Pressure field is analytically propagated using a Fourier transform assuming a continuous rectangular aperture.	23
2.9	Measurement of acoustic radiation force on a sphere. (Right) Schematic illustration. (Left) Actual setup.	24

2.10	Measured intensity of acoustic radiation force of focusing beam whose focus is at the center of the sphere.	24
2.11	Measured intensity of acoustic radiation force of focusing beam whose focus is on the surface of the sphere.	25
2.12	(Left)Schematic diagram of the setup for measuring ARF on a rigid sphere. (Right) Actual settings for the experiment.	26
2.13	Measured magnitude of acoustic radiation force on a rigid sphere of 200 mm in diameter for various distances from the aperture of the AUPA device. The black dots indicate the measured values. The dotted line indicates the polynomial approximate curve fitting the data points.	27
3.1	Linear dynamics model of a sphere in balancing control algorithm.	29
3.2	Cubic polynomials fitted to ARF measurement data of focus on the surface (upper) and focus on the center (lower).	32
3.3	Two-dimensional Example problem of finding duties that apply desired force on a sphere. (Left) Desired force. (Middle) Invalid solution yielded without consideration of constraints on duties. That contains pulling force by AUPA 1. (Right) Valid solution yielded with consideration on constraints on duties which consists of repulsive forces only.	33
3.4	Two-dimensional Example problem of finding duties that apply desired force on a sphere. (Left) Desired force. (Middle) Invalid solution yielded without consideration of constraints on duties. That contains pulling force by AUPA 2. (Right) Valid solution yielded with consideration on constraints on duties which consists of repulsive forces only. Note that this is not the only solution.	34

3.5	Workspace of the prototype system. The object has three translational DoF inside the white area. The work volume for an object of 1.3 mN in weight is shown in the left-side column, namely, (a-1), (a-2), and (a-3), and that for an object of 3.1 mN in effective weight is shown in the right-side column, (b-1), (b-2), and (b-3). The top, middle, and bottom images show the workspaces at an altitude of 885, 1085, and 1285 mm, respectively	41
3.6	Definition of coordinate system and arrangement of AUPA devices in the prototype system	42
3.7	Recorded trajectory in the case only proportional gain was applied. Black and gray lines indicate recorded and target values respectively.	42
3.8	Recorded trajectory during the stationary suspension task	43
3.9	A spherical object suspended at a fixed position.	44
3.10	Route in the translation task	44
3.11	Record of positions (left) and control variables (right) during the translation task. The black lines indicate the recorded position of the object. The gray lines in the left figure indicate the target position.	45
3.12	A sphere suspended at a position $r = [0 \ 250 \ 1285]^T$ mm	45
3.13	Translation sequence for workspace analysis.	46
3.14	Average position error at distances from the origin at various altitudes.	46
4.1	Acoustic manipulation by single-sided AUPA devices arranged in lattice.	48
4.2	Available force set.	49
4.3	Inner and outer radii of effective area for focusing beam.	51
4.4	Effective area of an AUPA.	51
4.5	Geometric relationships among effective areas of neighboring AUPA devices.	52

4.6	Geometric relationship between AUPAs.	53
4.7	Azimuth on the linear boundary (the line EF) and the circular boundary (the arc FG) in Fig. 4.6	53
4.8	Installation of ceiling-sided AUPA devices.	55
4.9	Schematic illustration of AUPA devices suspending an object that naturally ascends.	55
4.10	Vertical and horizontal ARF applied by a single AUPA device at the target altitudes. Black lines indicate ARF at an altitude of 500 mm. Dotted lines indicate ARF at an altitude of 700 mm. . .	56
4.11	Dimensions of ceiling-sided AUPA devices in the experiment. . . .	56
4.12	Recorded trajectory of balloons manipulated by single-sided AUPA devices.	57
4.13	Manipulation of two balloons.	57
5.1	Balloon display system for body-scale augmented reality.	59
5.2	Schematic diagram of floating display system	62
5.3	Schematic illustration of adaptive circular window. (Left): Calculation of adaptive circular window in a scenario wherein a user touches a floating screen. (Right) Application of window to depth camera view.	62
5.4	Registration of AUPAs and Kinect V2. Arrows direct the color marker attached on an aluminum frame.	64
5.5	Adaptive circular window applied to depth map. (Left) A View from the color camera. (Center) Raw depth image from depth camera. (Right) depth image with an adaptive circular window applied.	65
5.6	Projection of a scene viewed by a camera object in virtual world.	67
5.7	Schematic illustration of perspective-correct projection	72
5.8	Projection to mesh-discretized sphere.	72
5.9	Stereoscopic image of a Utah teapot.	73
5.10	Schematic illustration of experiment configuration.	75

5.11	Threshold target sizes of front-view condition (Right) and oblique-view condition (Left).	76
5.12	Mean ratings and unbiased standard deviations for negative effects of floating screen.	77
5.13	Floating display system with ceiling-sided AUPA devices.	77
5.14	Demonstration at Siggraph Asia 2019.	78
5.15	Personal display for workers	80
5.16	Person guided by an arrow displayed on a balloon display	80
5.17	Person talks with floating avatars.	80
6.1	Concept illustration of encounter-type haptic feedback system.	82
6.2	System configuration of encounter-type haptic feedback system.	83

List of Tables

3.1	Coefficients of a cubic polynomial fitted to ARF measurement data.	31
3.2	PID control gains.	35

Chapter 1

Introduction

This thesis presents an acoustic manipulation method of macroscopic objects within a human-scale workspace. Here, the term *macroscopic* means that the object is much larger than the wavelength of the sound. In this chapter, the author first discusses the significance of this technology in terms of its applications. Then, the author surveys previous acoustic manipulation technologies and other non-contact manipulation technology. Finally, the contribution of this paper is summarized and the organization is described.

1.1 Background and Motivation

Scattering and reflecting of propagating ultrasound applies force to an object to which the ultrasound impinged. The force is called the acoustic radiation force (ARF). The force can be used to control the motion of an object. Acoustic manipulation is a technique to control the position of an object utilizing acoustic radiation force.

Traditionally, acoustic manipulation has been used for manipulation of *microscopic* objects, or sub-half-wavelength objects, within relatively small workspace up to tabletop scale [1, 2, 3, 4, 5, 6]. In this research, the author proposes an acoustic manipulation method that can move and stabilize *macroscopic* objects in the air within a human-scale workspace, which is larger than one meter. We envision that such large-scale manipulation, even of lightweight objects, will open

up new applications. the author provides some examples below.

- **Three-dimensionally controllable floating display for augmented reality (AR).** Projection-based augmented reality is a technology that superimposes virtual information on surfaces of real-world objects using projectors. Compared to AR using head-mounted displays or tablet devices, it has the advantages of seamless integration to the real world, tangible and intuitive input surfaces, and shareable contents.

Using floating objects with this technology, such interaction surfaces can be placed at arbitrary three-dimensional positions (Fig. 1.1). Similar goals have been pursued using aerial vehicles [7, 8, 9]. The proposed manipulation technology method, it is possible to display contents different from the conventional method by using the advantage that all the energy required for floating is supplied from the outside. The detail will be presented in Chapter 5 along with its implementation.

- **Unmanned aerial vehicles.** Acoustically manipulated objects equipment with task-performing payloads such as sensors, or displays can serve as battery-free aerial vehicles controlled by an external actuator for indoor use (Fig. 1.1). For example, if a camera or sensor is installed, it can be used as a robot to patrol the indoor environment. Although available force to support the weight of payload provided by the acoustic radiation force is limited, compensation of the weight by the buoyancy of helium-filled balloons will ease the problem.

We can find examples of externally actuated vehicles. Most familiar one may be sailing ships. Another example is solar sails [10]. They utilize external power to propel themselves without consuming onboard fuel. There are a few researches of manipulating particle-size robots by ultrasound. [11].

- **Manipulator in micro-gravity environments.** The technology can be used for a general-purpose manipulator in micro-gravity environments because the force required to counteract the gravity is small (Fig. 1.2). Such a noncontact manipulator for general purpose provides a way to handle

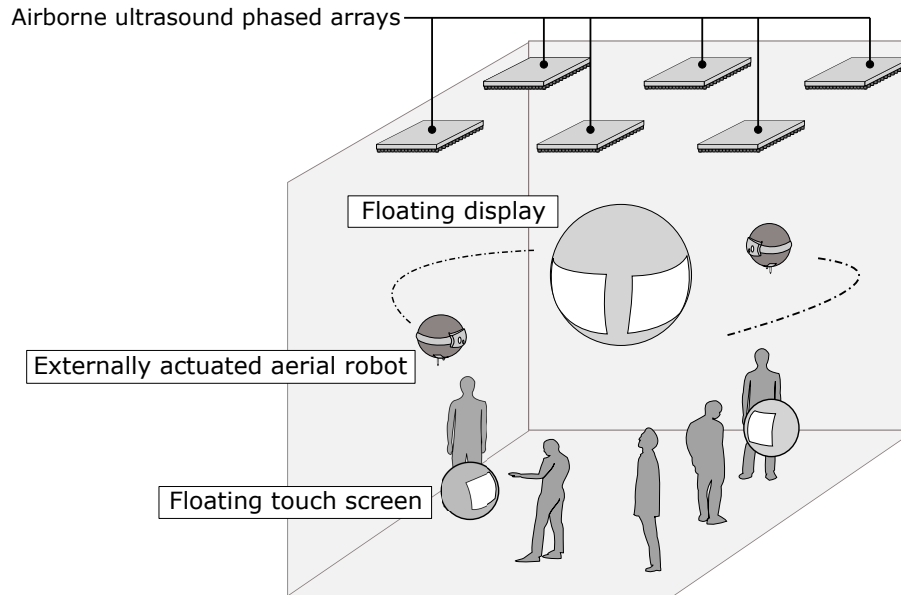


Fig. 1.1. Application scenarios.

fragile objects and heated objects. In addition, the absence of mechanical actuators may save the payloads of the carrier spacecrafts.

We propose a method using airborne ultrasound phased array (AUPA) [12, 13, 14, 15, 16]. Furthermore, the author also shows examples of application systems: a floating display system and a haptic feedback system.

This research is based on the recent development of transducer arrays. Multiple arrays can be synchronized by just plugging power source and Ethernet cable [17], thereby enabling human-scale applications [18, 19, 20]. Although the cost is still high and its installation is cumbersome, we expect these problems will be solved. They are commercialized (e.g. Stratos by UltraLeap [21]) and the development of thinner and more efficient devices are undergoing [22, 23].

1.2 Related Works

In this section, the author surveys noncontact manipulation technologies developed so far, and describes our contribution in the context of manipulation technologies.

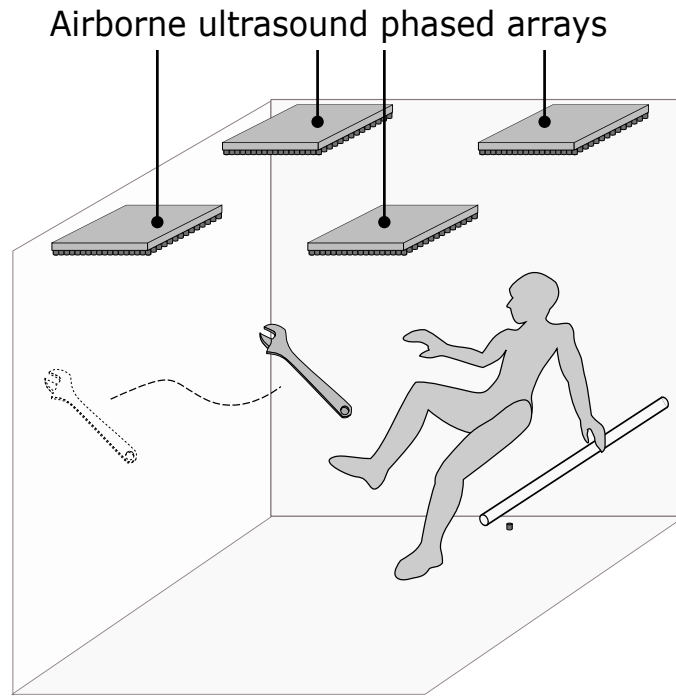


Fig. 1.2. Noncontact versatile manipulator for microgravity environment.

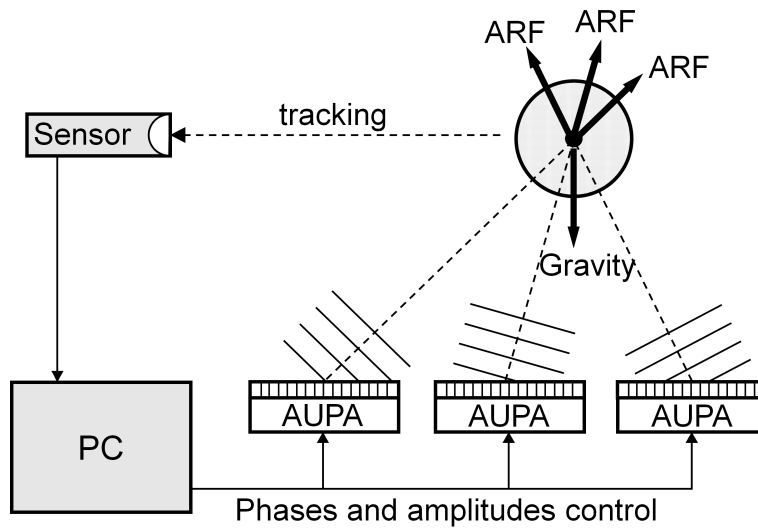


Fig. 1.3. Schematic illustration of dynamic acoustic manipulation.

Noncontact manipulation is a technology to control an object in the air using external actuators. Historically, it has been achieved by adding a move function to a *levitation* technology, which aims to stabilize an object in the air. Therefore, noncontact manipulation has a close relationship with levitation technologies. An excellent review of levitation can be found in [5]. Among a number of manipulation/levitation technologies, we introduce acoustic, aerodynamic, and magnetic ones because the other ones are microscopic and out of the interest of this research.

1.2.1 Acoustic Levitation/Manipulation

Acoustic waves can remotely exert a force in the form of ARF. Although ARF is relatively weak, it is beneficial in its spatio-temporal controllability and reproducibility compared with aerodynamic forces. Further, ARF can be generated on general objects, whereas magnetic methods are only applicable to magnetic objects. These ARF properties are exploited in applications such as mid-air haptic feedback, by remotely applying a force on a skin [12, 24, 15, 25]. ARF has also been used for mid-air manipulations. Most existing acoustic manipulation methods generate an acoustic trap (a point at which the ARF converge), to suspend an object in the air. Typically, such trap was achieved with nodes of standing waves generated by opposing transducers or a pair of transducer and reflector. Whymark demonstrated the suspension of particles in air using a pair of vertically opposing transducers [26]. Foresti et al. achieved horizontal manipulation of particles by temporally changing the driving voltages of the transducer array and moving the position of the standing wave [27]. Ochiai et al. demonstrated 3D particle manipulation by generating a standing wave using two pairs of opposing phased array devices [28]. A Bessel beam can also be used to trap a particle in the air. Courtney et al. and Seah et al. demonstrated 2D particle manipulation in a vertical plane surrounded by transducers using a Bessel beam [29, 30]. Marzo et al. proposed three types of traps: twin traps, bottle traps, and vortex traps. Further, they demonstrated 3D manipulation of particles using a single-sided phased array device [31]. Later, he developed a functional method to trap particles in

the air [32]. These traps have a well-known limitation regarding the size of the trapped objects; the object size must be smaller than half the wavelength of the sound. Trapping of a wavelength-scale particle by multiplexing acoustic vortices each of which has an opposite chirality was recently reported [33]. Boundary hologram method demonstrated levitation of a sphere of a 30mm radius at a 200mm altitude and an octahedron of a 50mm diagonal length at the same altitude [34]. Some mid-air acoustic suspension techniques for objects larger than the wavelength have also been proposed. Anderde et al. suspended an object larger than the wavelength by creating a standing wave between the transducers and the object [35, 36]. Ueha et al. used a near field to manipulate a planar object at a height in the order of tens of μ m [37, 38]. These methods require the distance between the object and actuator to be fixed or in close proximity. Therefore, this requirement constrains the translational DoF of the object. Whereas these existing acoustic 3D manipulation methods are focused on objects whose sizes are up to a few wavelengths, our method focuses on macroscopic objects that are 10 times larger than the sound wavelength, for example 200 mm diameter object for 40 kHz ultrasound with the wavelength of 8.5 mm. Our method contributes to the acoustic manipulation research increasing the size of the objects controlled. In addition, the workspace of the proposed method is larger than that of conventional methods. To achieve the manipulation of macroscopic objects in a large workspace, our method dynamically controls the acoustic field to stabilize the position of the object based on a PID sensor-feedback control scheme, in contrast to conventional methods that use a quasi-static acoustic field.

Sensor-feedback-based acoustic manipulation is only demonstrated on a two-dimensional plane that is enclosed by opposing transducers [39, 40].

In the context of acoustic manipulation, this research is an attempt to eliminate the difficulty of creating a trap in macroscopic scale by performing disturbance stabilization with sensor-feedback control. It also allows concentration of the acoustic energy in a single point.

1.2.2 Magnetic Levitation/Manipulation

Magnetic manipulation technologies is used for control of objects inside workspace of about 10 cm height. In most applications, it is for eliminating mechanical contact such as bearing or containerless handling in experiments, or two-dimensional actuation for transportation. Recently, it is used for three-dimensional actuation including vertical movement in the field of microrobotics [41] and interfaces [42, 43]. The largest workspace of 9cm has been achieved by Lee et al [43].

Aside from target object size and workspace, the technique is also characterized by its property to act only on magnetic objects. This allows occlusion with non-magnetic objects while it restricts its use only to magnetic objects.

1.2.3 Aerodynamic Manipulation

In aerodynamic levitation, a spherical object is levitated by air-jet blowing upward. The upward flow generates drag force to counteract gravity force. In transverse directions, Bernoulli and Magnus force produces centering force. The application includes containerless processing of specimens in physical experiments [44, 45], interfaces [46, 47], and robotics [48]. The centering force is strong enough to tilt the jet. Becker et al demonstrated that control of the flow rate and the direction of the jet can manipulate spheres with radii of several centimeters at the distance of several tens of centimeters within some jet angles [48].

1.3 Organization

The rest of the paper is organized as follows: Chapter 2 describes the physical phenomena behind dynamic acoustic manipulation and the airborne ultrasound phased array. Chapter 3 presents a force balancing control algorithm. Chapter 4 demonstrates acoustic manipulation of macroscopic objects by single-sided phased array transducers. Chapter 5 proposes an aerial display system that is intended for use in AR. The application scenarios benefited from the configuration is also

presented. Chapter 6 proposes another application system: encounter-type haptic feedback system. Chapter 7 gives the conclusion.

Chapter 2

Acoustic Radiation Force Model

In this chapter, the acoustic radiation force on a sphere applied by airborne ultrasound phased array is investigated. First, the physical principles of sound propagation and acoustic radiation force are introduced. Second, airborne ultrasound phased array is introduced. Finally, acoustic radiation force on a macroscopic sphere is discussed in a ray-acoustics approach.

2.1 Physics of Acoustic Radiation Force

This section describes the physics of acoustic radiation pressure. It is known that an object placed in a sound field receives force. This is called acoustic radiation pressure.*¹

Here, let's consider what force the acoustic radiation pressure gives from a hydrodynamic point of view.

The basic equations for inviscid fluids are the equation of continuity and Euler's equation described as follows:

$$\frac{\partial \rho}{\partial t} + \nabla(\rho \mathbf{u}) = 0 \quad (2.1)$$

$$\frac{\partial \mathbf{u}}{\partial t} + (\mathbf{u} \cdot \nabla) \mathbf{u} = -\nabla p. \quad (2.2)$$

*¹ This force may be excited by the sound waves that are observed even when there is no medium flow. This is another phenomenon called acoustic flow. I'll omit the explanation here.

Consider the case where the pressure changes slightly in the absence of sound (pressure $p = p_0$, density ρ_0 , $u = 0$). Let the change in pressure be Δp , the change in density be $\Delta\rho$, and the change in particle velocity be Δu . Then, the following relationships about the ratio between the original state and the amount of change holds: [49]

$$\frac{p}{p_0} \approx \frac{\rho}{\rho_0} \approx \frac{|\mathbf{u}|}{c_0} = \varepsilon \ll 1 \quad (2.3)$$

where ε is called acoustic Mach number. Now, let me consider the power-expanding of the pressure, density, and particle velocity around the soundless state. Equations (2.1), (2.2) are expanded to the power as follows.

$$\begin{aligned} \rho &= \rho_0 + \rho_1 + \rho_2 + \dots \\ p &= p_0 + p_1 + p_2 + \dots \\ \mathbf{u} &= \mathbf{u}_1 + \mathbf{u}_2 + \dots \end{aligned} \quad (2.4)$$

where the subscripts i means that its quantity is the order of $O(\varepsilon^i)$. First, the author considers the quantities of the first order. For the expression assigned to the expression (2.4) to the expression (2.2), (2.1), the first-order quantity is collected. Each formula becomes

$$\frac{\partial \rho_1}{\partial t} + \nabla(\rho_0 \mathbf{u}_1) = 0 \quad (2.5)$$

$$\frac{\partial \mathbf{u}}{\partial t} = -\frac{1}{\rho_0} \nabla p_1. \quad (2.6)$$

Taking the rotation of the Eq. (2.6) yields $\nabla \times \mathbf{u} = 0$ because $\nabla \times \nabla p_1 = 0$. This indicates that the particle velocity \mathbf{u} can be described by gradient of velocity potential ϕ_1 as follows:

$$\mathbf{u} = -\text{grad}\phi_1. \quad (2.7)$$

Substituting this into the expression (2.5) and (2.6) yields:

$$\frac{1}{c_0^2} \frac{\partial^2 \phi}{\partial t^2} + \Delta \phi_1 = 0 \quad (2.8)$$

As shown in these equations, c_0 is the speed of sound. Here, the author assumes harmonic oscillation. Then, Eq.(2.8) becomes:

$$(\Delta + k^2)\phi_1 = 0 \quad (2.9)$$

where $k = \frac{2\pi}{\lambda}$ is a wave number. Here, the sound pressure p_1 is represented as $p_1 = j\rho\omega\phi_1$.

Next, the author considers the quantities of the second order. Taking the second-order quantities from (2.1) and (2.2) yields:

$$\nabla p_2 + \rho_0 \frac{\partial \mathbf{u}_2}{\partial t} = \nabla(U - K) \quad (2.10)$$

where

$$U = \frac{p_1^2}{2\rho_0 c^2}, \quad K = \frac{1}{2}\rho_0 \mathbf{u} \cdot \mathbf{u}. \quad (2.11)$$

As you can see by taking the rotation of the expression (2.10), you can see that velocity potential can be defined for the second order of the particle velocity.

$$\mathbf{u}_2 = -\text{grad}\phi_2 \quad (2.12)$$

As [50] pointed out, the following equation holds from the law of conservation of momentum in the region V surrounding the object.

$$\mathbf{F} = \frac{d\mathbf{M}}{dt} + \frac{d}{dt} \iiint_V \rho \mathbf{u} dV = \iint_R (p\mathbf{n} - \rho \mathbf{u} u_n) dR \quad (2.13)$$

Here, when the momentum change of the fluid in the region is written up to the second order quantity using the velocity potential, the following equation holds:

$$\begin{aligned} \iiint_V \frac{\partial}{\partial t} (\rho \mathbf{u}) dV &= - \iiint_V \rho_0 \frac{\partial}{\partial t} \nabla(\phi_1 + \phi_2) dV + \iiint_V \rho_1 \mathbf{u}_1 \\ &= - \iint_R \rho_0 \frac{\partial}{\partial t} (\phi_1 + \phi_2) \mathbf{n} dR + \iiint_V \frac{\partial}{\partial t} (\rho_1 \mathbf{u}_1) dV. \end{aligned} \quad (2.14)$$

In the last transformation, the author used the relationship $\iiint_V \nabla \phi dV = \iint_S \phi \mathbf{n} dS$. The following equation also holds:

$$\iint_R p \mathbf{n} dR = \iint_R \rho_0 \frac{\partial}{\partial t} (\phi_1 + \phi_2) - L \quad (2.15)$$

Substituting this into Eq.(2.13) yields:

$$\mathbf{F} = - \iiint_V \frac{\partial}{\partial t} (\rho_1 \mathbf{u}_1) dV - \iint_R \rho_0 \mathbf{u}_1 u_{1n} dR + \iint_R L \mathbf{n} dR \quad (2.16)$$

In this thesis, let us consider the case of a rigid body, that is, the case where the object surface does not deform. This is a reasonable assumption, assuming that

many solids have a sufficiently high acoustic impedance compared to that of air. In that case, acoustic radiation pressure is given by the following equation: [51]

Time averaging yields:

$$\mathbf{F} = \int_S \langle L - \rho_0 \mathbf{u}_1 u_{1n} \rangle dS \quad (2.17)$$

where L is Lagrangian, which is given by the following:

$$L = U - K. \quad (2.18)$$

Equations (2.17) and (2.18) indicates that acoustic radiation pressure is proportional to the square of the sound pressure on the surface. Let us consider the case where the object is a rigid body. At that time, the normal component of the particle velocity on the surface of the rigid body, i.e. $u_{n1} = 0$. Therefore, Eq. (2.17) becomes:

$$\mathbf{F} = \int_S \langle L \rangle dS. \quad (2.19)$$

As this equation expresses, acoustic radiation pressure can be obtained from the first-order quantities, that is, the sound pressure obtained in linear acoustics.

2.2 Airborne Ultrasound Phased Array (AUPA)

In this chapter, we describe the specifications of an airborne ultrasound phased array (AUPA) device used throughout this research (Fig. 2.2).

Each device has 249 ultrasound transducers of 40 kHz resonant frequency (Nippon Ceramic Co., Ltd T4010A1). They are arranged in square lattice forming a rectangular aperture of 182.88 mm \times 142.24 mm.

The transducers are driven in the same manner as in [12, 15]. The input voltage to each transducer is a rectangular wave of 24 V_{pp} amplitude, 0 V average and 40 kHz frequency (Fig. 2.3). The driving amplitude p is controlled by adjusting the duty cycle of the input D . The transducers extract only the component of resonant frequency (40 kHz) from the input rectangular wave. The resonant component can be calculated by the Fourier series decomposition. As a result, the following

relationship between the duty cycle D and the driving amplitude p holds:

$$D = \frac{1}{\pi} \sin^{-1} \left(\frac{p}{p_M} \right) \quad (2.20)$$

where p_M is the maximum driving amplitude of the transducer. As shown in this figure, the maximum amplitude is obtained by a duty cycle of $1/2$.

The synchronization method of the driving phase among transducers are described in [17]. In this architecture, all AUPA devices are connected in a daisy chain with Ethernet RJ45 cables. The driving amplitude and phase of each transducer can be controlled according to the command from the PC. The phase and amplitudes are refreshed synchronously among all of the transducers on the multiple devices, which communicate with one another via EtherCAT protocol.

The sound pressure at a position \mathbf{r} generated by AUPA can be represented by the superposition generated by each transducer at \mathbf{r}_i :

$$p(\mathbf{r}) = \sum_i q_i \frac{D_i(\theta_i)}{|\mathbf{r} - \mathbf{r}_i|} \exp(ik|\mathbf{r} - \mathbf{r}_i|) \quad (2.21)$$

where the subscripts i is the id of the transducer, q_i is the complex gain, θ_i is an angle between the transducer and $\mathbf{r} - \mathbf{r}_i$, and $D(\theta)$ is the directivity of the transducer.

An AUPA can synthesize beams of various waveforms by controlling the driving phase their onboard transducers synchronously. In this research, plane wave beams and focusing beams are used (Fig. 2.1). Now, let ψ_i be the sound pressure (the sum of the incident wave and the reflected wave) generated on the object surface when a certain element is reflected by the reflector. At this time, since superposition is established from the expression (2.21), the sound field generated by the phased-array is

$$\psi = \sum_i q_i \psi_i. \quad (2.22)$$

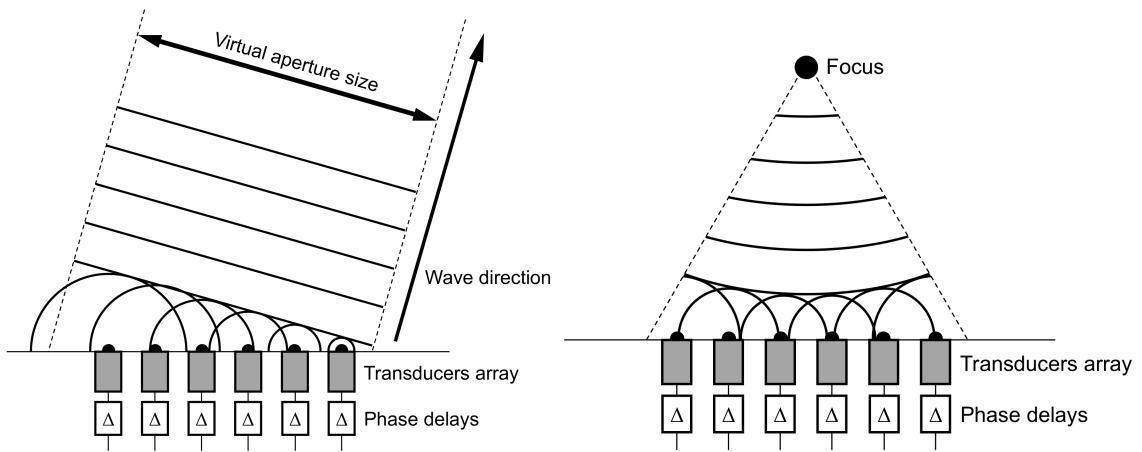


Fig. 2.1. Waveform synthesis by airborne ultrasound phased array

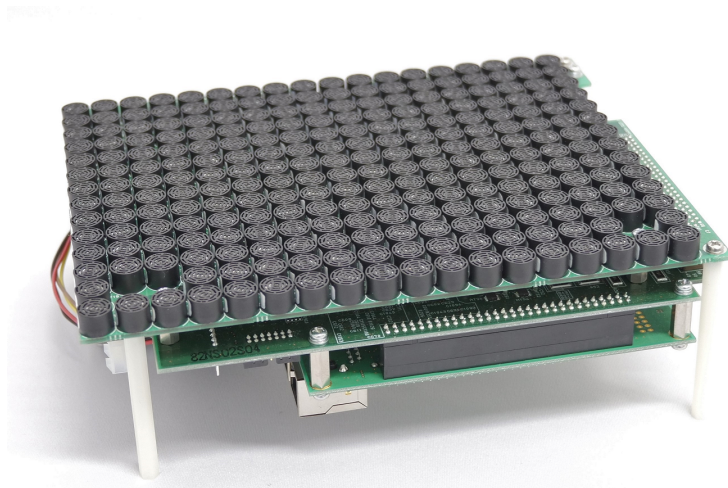


Fig. 2.2. Appearance of the aerial ultrasonic phased array.

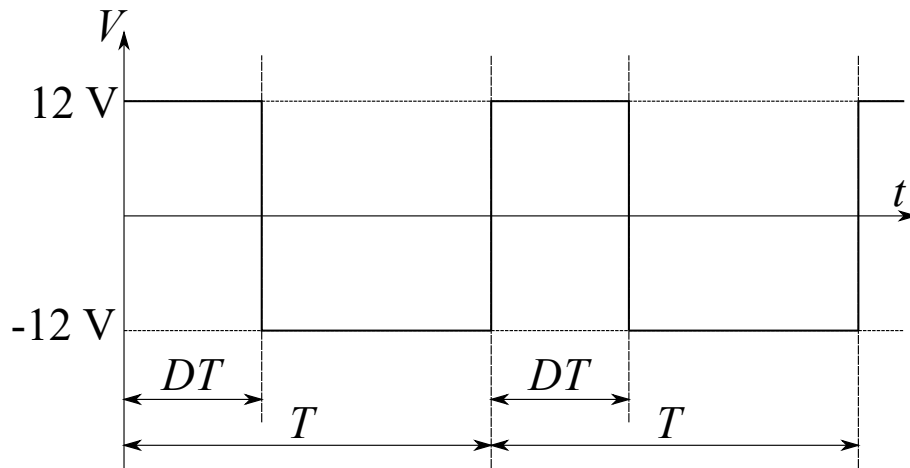


Fig. 2.3. Input voltage to transducers.

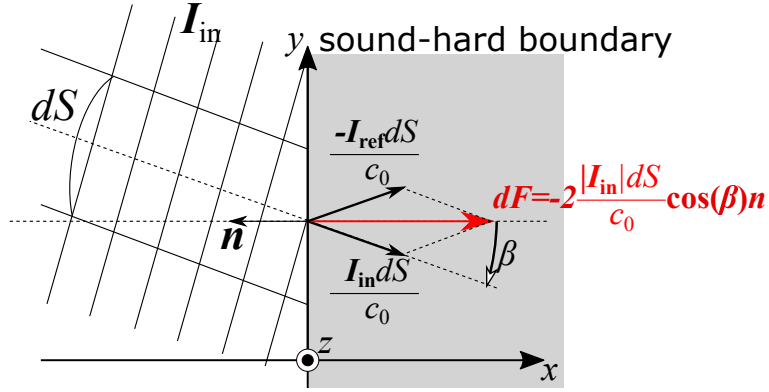


Fig. 2.4. Plane wave incident on a planar surface.

Substituting this into (2.17) and (2.18) yields

$$\mathbf{F} = \mathbf{q}^T \mathbf{A}(\mathbf{r}) \mathbf{q}^* \quad (2.23)$$

$$\mathbf{A} = \begin{bmatrix} \psi_1 \psi_1^* & \psi_1 \psi_2^* & \cdots & \psi_1 \psi_N^* \\ \psi_2 \psi_1^* & \psi_2 \psi_2^* & \cdots & \psi_2 \psi_N^* \\ \vdots & \vdots & \ddots & \vdots \\ \psi_N \psi_1^* & \psi_N \psi_2^* & \cdots & \psi_N \psi_N^* \end{bmatrix} \quad (2.24)$$

$$\mathbf{q} = [q_1 \quad q_2 \quad \cdots \quad q_N]^T. \quad (2.25)$$

where $*$ denotes a conjugate. Manipulation is nothing but the problem of designing a complex gain \mathbf{q} that generates a sound field that gives the desired force \mathbf{F} . The matrix \mathbf{A} is a function of the position of the object. In this study, the author proposes a method to determine \mathbf{A} by observing the position of an object and to specify \mathbf{q} based on \mathbf{A} .

From these equations, we can see that this problem consists of three problems.

- How to determine \mathbf{A} ?
- How to design the force \mathbf{F} that controls the object?
- How to find the gain \mathbf{q} ?

2.3 Acoustic Radiation Force Model for Macroscopic Sphere

2.3.1 Analysis of Focusing Beam: Ray-acoustics Approach

Good control requires a reasonably good model. To achieve control of a sphere of various radii within a large workspace, it is necessary to develop an ARF model that is applicable to various combinations of the radii and the distances. This section investigates ARF on a macroscopic sphere located far from the aperture, which is the interest of this research.

Sphere has been a common topic in previous researches on ARF [52, 53, 54, 55, 56]. In previous researches of levitation and manipulation, Gorkov potential [28], infinite expansions of spherical harmonics [33], finite element method [35], and boundary element method [34] were used and have been proven to be effective. Although the methods are useful to analyze a single case, it is challenging to predict the qualitative effect of changes in the object size and distance.

In this section, the author calculates ARF using a ray-acoustics approach. Ray-acoustics is valid if the scatterer is sufficiently larger than the wavelength so that the effect of diffraction around the scatterer is negligible. Ray-acoustics approach not only reduces the computational cost but also provides insight on the effect of changes in the object size and distance as described later in Section 2.3.2. A few Ray-acoustics-based analysis on ARF can be found [57, 58]. The models were developed as an analogy to optics. However, their applicable scale, their relationship to wave-acoustics were not discussed. They have not been verified by experiment.

First, the author develops a ray-acoustic-based ARF model for a macroscopic rigid sphere based on Fresnel diffraction mode. Second, the author compares the calculation results of the ray-acoustics approach and a wave-acoustics approach, which has been proven to be effective. Third, the author investigates the effect of changes in distance and radius by investigating the ray-acoustics-based model.

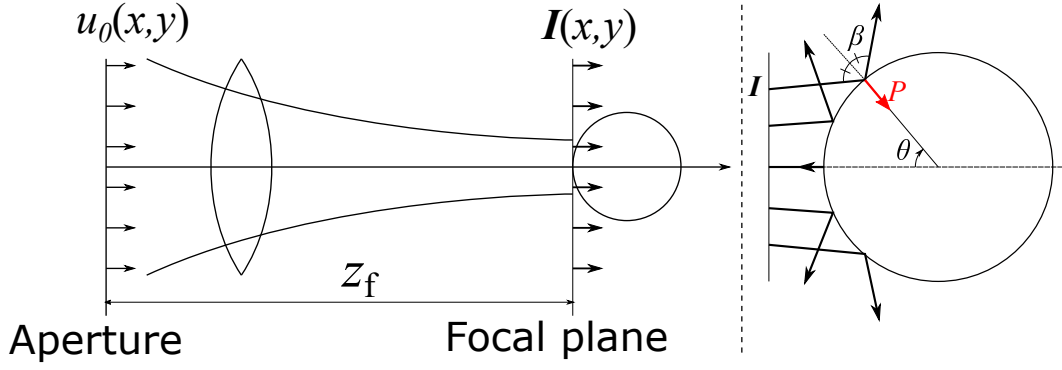


Fig. 2.5. Calculation of acoustic radiation pressure on a macroscopic sphere based on ray-acoustics. (Left) Step1: Wave propagation to focal plane. (Right) Step2: Calculation of acoustic radiation pressure based on geometric reflection of incident ray of intensity I .

Finally, the author reports the result of an ARF measurement experiment and compare the result with ray-acoustics-based ARF-model.

Acoustic radiation pressure (Fig. 2.4 of an impinging wave can be described using acoustic intensity I as follows:

$$P = 2 \frac{|I|}{c_0} \cos(\beta) \mathbf{n} \quad (2.26)$$

$$I = \text{Re}[p\mathbf{v}^*]. \quad (2.27)$$

where $\text{Re}[\cdot]$ indicates the real part of \cdot . Integration (2.26) for all rays that intersects the sphere results in acoustic radiation force \mathbf{F} :

$$\mathbf{F} = \int_S 2 \frac{|I|}{c_0} \cos \beta \mathbf{n} dS. \quad (2.28)$$

In ray-acoustics approach, the acoustic radiation force can be calculated in the following two steps (Fig. 2.5):

- (Step 1) Calculate the intensity field $I(x, y)$ in front of the sphere.
- (Step 2) Calculate the acoustic radiation force.

Figure 2.6 compares the calculation results based on the ray-acoustics approach and the wave-acoustics approach [56]. ARF applied by a focusing-on-the-surface beam from a single AUPA device is shown. The intensity field is numerically

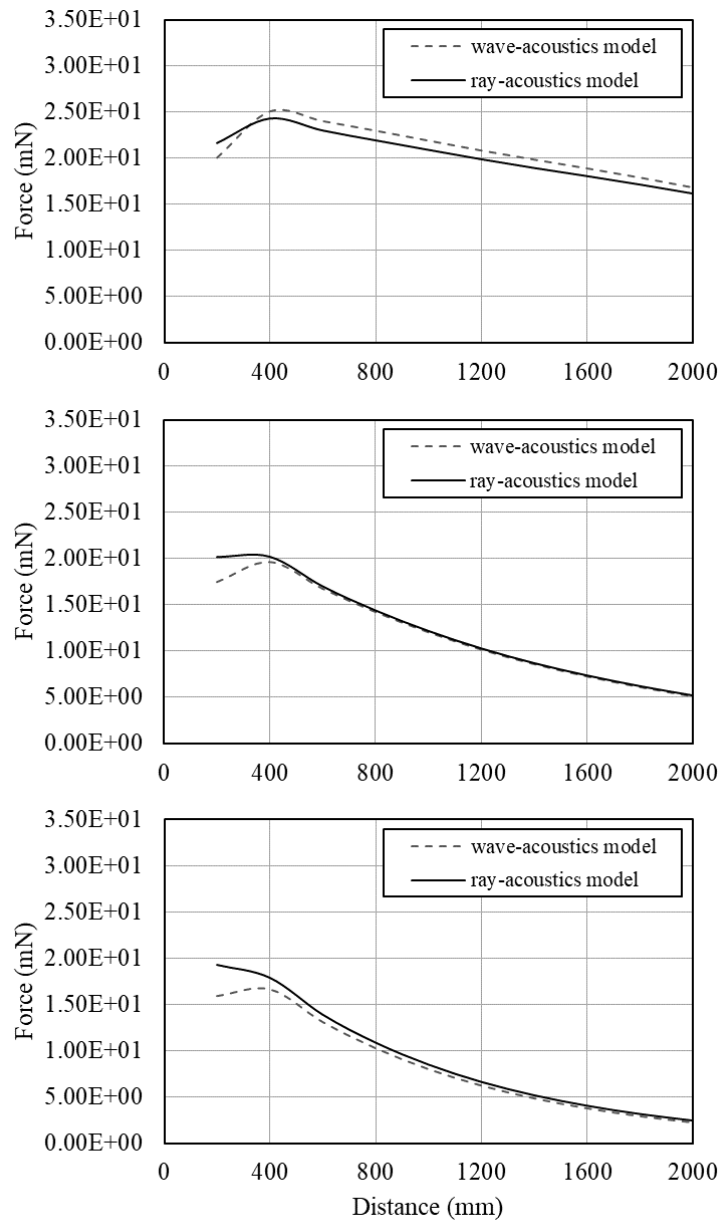


Fig. 2.6. Comparison of ARF calculation results based on ray-acoustics approach and wave-acoustics approach for absorption coefficient (Upper: 0 Neper/m. Middle: 0.3 Neper/m. Lower: 0.5 Neper/m).

calculated using Eq. (2.21). It is confirmed that they are in good correspondence far from the aperture.

2.3.2 Analytical Calculation

To get an insight on ARF dependency on distance and radius, the author calculates ARF analytically. When a focal point is generated on the sphere, the pressure on the focal plane $p(x, y)$ and $\mathbf{v}(x, y)$ is represented by Fourier transform of the pressure distribution on the aperture $p_0(x, y)$ and its derivative as following:

$$p(x, y) = \rho\omega U \frac{1}{4\pi z_f} \exp\left(jk \frac{x^2 + y^2}{2z_f}\right) \widehat{p}_0\left(k \frac{x}{z_f}, k \frac{y}{z_f}\right) \quad (2.29)$$

$$\mathbf{v}(x, y) = U \frac{1 + jkz_f}{4\pi z_f^3} \exp\left(jk \frac{x^2 + y^2}{2z_f}\right) \times \left\{ \widehat{p}_0\left(k \frac{x}{z_f}, k \frac{y}{z_f}\right) \begin{bmatrix} x \\ y \\ z_f \end{bmatrix} - j \begin{bmatrix} \frac{d\widehat{p}_0}{d\nu_x}\left(k \frac{x}{z_f}, k \frac{y}{z_f}\right) \\ \frac{d\widehat{p}_0}{d\nu_y}\left(k \frac{x}{z_f}, k \frac{y}{z_f}\right) \\ 0 \end{bmatrix} \right\} \quad (2.30)$$

where z_f is the focal length, $\widehat{f}(\nu_x, \nu_y) = \int_{-\infty}^{\infty} \int_{-\infty}^{\infty} f(x, y) e^{-j(\nu_x x + \nu_y y)} dx dy$. Assuming that $kz_f \gg 1$, we write the particle velocity distribution as follows:

$$\mathbf{v}(x, y) = \frac{jkU}{4\pi z_f^2} \exp\left(jk \frac{x^2 + y^2}{2z_f}\right) \left\{ \widehat{p}_0\left(k \frac{x}{z_f}, k \frac{y}{z_f}\right) \begin{bmatrix} x \\ y \\ z_f \end{bmatrix} - j \begin{bmatrix} \frac{d\widehat{p}_0}{d\nu_x}\left(k \frac{x}{z_f}, k \frac{y}{z_f}\right) \\ \frac{d\widehat{p}_0}{d\nu_y}\left(k \frac{x}{z_f}, k \frac{y}{z_f}\right) \\ 0 \end{bmatrix} \right\}. \quad (2.31)$$

Substituting (2.29) and (2.31) to (2.27) yields:

$$\mathbf{I}(x, y) = \rho\omega \left| \frac{U}{4\pi z_f} \widehat{p}_0\left(k \frac{x}{z_f}, k \frac{y}{z_f}\right) \right|^2 \begin{bmatrix} x/z_f \\ y/z_f \\ 1 \end{bmatrix}. \quad (2.32)$$

Next, the author calculates the reflection angle and impinging position of the acoustic ray that passed the position (x, y) using geometric relationships (Fig. 2.7) by using Eq. (2.43), To derive the reflection angles and the incident points, we only need the direction of intensity vector $\mathbf{e}_I(x, y)$

$$\mathbf{e}_I = [x/z_f \quad y/z_f \quad 1]^T \quad (2.33)$$

It is convenient to use the polar coordinate for its axisymmetry $r = \sqrt{x^2 + y^2}$. From the law of cosine, the following relationship holds:

$$R^2 = a^2 + (R + z_f)^2 - 2Ra \cos(\phi). \quad (2.34)$$

Solving the equation and taking smaller solution yields the length a

$$a = R \cos(\phi) - \sqrt{(R \cos \phi)^2 - (R + z_f)^2 - R^2}. \quad (2.35)$$

Again, the law of cosine yields the cosine of the reflection angle β as following:

$$\cos(\beta) = -\frac{R^2 + a^2 - (R + z_f)^2}{2Ra}$$

For rays tangent to the sphere, the following equation holds:

$$r_{\max}^2 = \frac{R^2}{1 + 2\frac{R}{z_f}}, \quad (2.36)$$

which determines the radius of integration domain S . Using the reflection angle β and the impinging polar angle θ ,

$$F_z = 2 \int_{x^2 + y^2 \leq r_{\max}^2} \frac{|\mathbf{I}|}{c_0} \cos \beta \cos \theta dx dy \quad (2.37)$$

Now we perform variable transformation $\bar{x} = \frac{x}{z_f}, \bar{y} = \frac{y}{z_f}$. Then, the above equations are shown to be functions only of the ratio of the radius and the distance of the sphere $\bar{R} = R/z_f$ as following:

$$\begin{aligned} F_z(\bar{R}) &= 2 \int_{\bar{x}^2 + \bar{y}^2 \leq \bar{r}_{\max}^2} \frac{\rho\omega}{c_0} \left| \frac{U}{4\pi} \hat{p}_0(k\bar{x}, k\bar{y}) \right|^2 \cos \beta \cos \theta d\bar{x} d\bar{y} \quad (2.38) \\ \bar{r} &= \sqrt{\bar{x}^2 + \bar{y}^2} \\ \bar{r}_{\max} &= \frac{\bar{R}^2}{\sqrt{1 + 2\bar{R}}} \\ \bar{a} &= \frac{a}{z} = \frac{(\bar{R} + 1)}{\sqrt{1 + \bar{r}^2}} - \sqrt{\frac{(\bar{R} + 1)^2}{\sqrt{1 + \bar{r}^2}} - [(\bar{R} + 1)^2 - \bar{R}^2]} \\ \cos \beta &= \frac{\bar{R}^2 + \bar{a}^2 - (\bar{R}^2 + 1)}{2\bar{R}\bar{a}} \\ \cos \theta &= \frac{1}{\sqrt{1 + \bar{r}^2}} (\cos \beta + \bar{r} \sin \beta). \end{aligned}$$

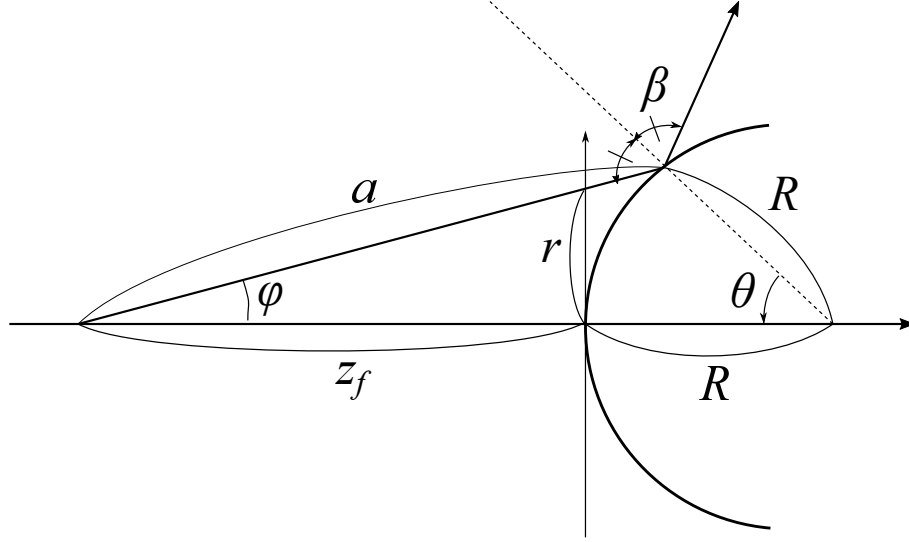


Fig. 2.7. Geometric Relationship among incident points and reflection angles of the incident acoustic rays.

For the case atmospheric absorption of coefficient α exists, the above equation can be modified as follows:

$$F_z(z_f, \bar{R}) = 2 \exp(-\alpha z_f) \int_{\bar{x}^2 + \bar{y}^2 \leq \bar{r}_{\max}^2} \frac{\rho\omega}{c_0} \left| \frac{U}{4\pi} \hat{p}_0(k\bar{x}, k\bar{y}) \right|^2 \cos \beta \cos \theta d\bar{x}d\bar{y} \quad (2.39)$$

under the assumption that the distance z_f is large enough to approximate

$$\exp(-\alpha \sqrt{x^2 + y^2 + z_f^2}) \approx \exp(-\alpha z_f). \quad (2.40)$$

2.3.3 Case of Focusing Beam of Rectangular Aperture

When a focal point is created by a rectangular aperture of length L_x and L_y , the sound pressure and velocity on the focal plane are described as follows:

$$p(x, y) = j\omega\rho \frac{U}{4\pi z_f} \exp\left(jk \frac{x^2 + y^2}{2z_f}\right) L_x L_y \text{sinc}\left(\frac{kL_x}{2\pi z_f} x\right) \text{sinc}\left(\frac{kL_y}{2\pi z_f} y\right) \quad (2.41)$$

$$\mathbf{v}(x, y) = \frac{1 + jkz_f}{4\pi z_f^3} U L_x L_y \quad (2.42)$$

$$\times \left\{ \text{sinc}\left(\frac{kL_x}{2\pi z_f} x\right) \text{sinc}\left(\frac{kL_y}{2\pi z_f} y\right) \begin{bmatrix} x \\ y \\ 1 \end{bmatrix} - j \begin{bmatrix} \text{dsinc}\left(\frac{kL_x}{2\pi z_f} x\right) \text{sinc}\left(\frac{kL_y}{2\pi z_f} y\right) \\ \text{sinc}\left(\frac{kL_x}{2\pi z_f} x\right) \text{dsinc}\left(\frac{kL_y}{2\pi z_f} y\right) \\ 0 \end{bmatrix} \right\}$$

where z_f is the focal length, U is the volume velocity, and $\text{dsinc}(x) = \frac{d}{dx}\text{sinc}(x)$. Assuming $kz_f \gg 1$ and taking real parts, the intensity field on the focal plane is described as follows:

$$\mathbf{I}(x, y) = \rho_0 c \left[\frac{U}{4\pi z_f} L_x L_y \text{sinc}\left(\frac{kL_x}{2\pi z_f} x\right) \text{sinc}\left(\frac{kL_y}{2\pi z_f} y\right) \right]^2 \begin{bmatrix} x/z_f \\ y/z_f \\ 1 \end{bmatrix}. \quad (2.43)$$

From geometric considerations and Eq. (2.26), acoustic radiation force acting on a sphere of R radius along beam direction can be described as follows:

$$\begin{aligned} F_z &= \int_0^{2\pi} \int_0^{r_{\max}} -2 \frac{|\mathbf{I}|}{c_0} \cos \alpha \frac{1}{\sqrt{1+r^2}} r dr d\phi \\ r &= \sqrt{X^2 + Y^2} \\ r_{\max} &= R_n / \sqrt{2R_n + 1} \\ X &= x/z_f, \quad Y = y/z_f, \quad R_n = R/z_f \\ a &= \frac{R_n + 1}{\sqrt{r^2 + 1}} - \sqrt{R_n^2 - (R_n + 1)^2 \left(\frac{r^2}{r^2 + 1} \right)} \\ \cos \alpha &= \frac{R_n^2 + a^2 - (R_n + 1)^2}{2R_n a}. \end{aligned} \quad (2.44)$$

Note that Eq. (2.44) is normalized by the distance from the aperture to the focal point (i.e. the closest point of the sphere). This means that scaling both in radius and distance of the sphere yields the same magnitude of acoustic radiation force.

Numerical Calculation of the force is shown below. In this simulation, atmospheric absorption coefficient [59] of 0.0005^{-1} is considered. Although the result fits well in distant places, the behavior in near fields is inconsistent with measured values. This error can be corrected by considering the directivity of the transducers.

2.3.4 Experiment

The author examined directional characteristics of acoustic radiation force on a sphere generated by focusing beam from an AUPA device of various angles and distances.

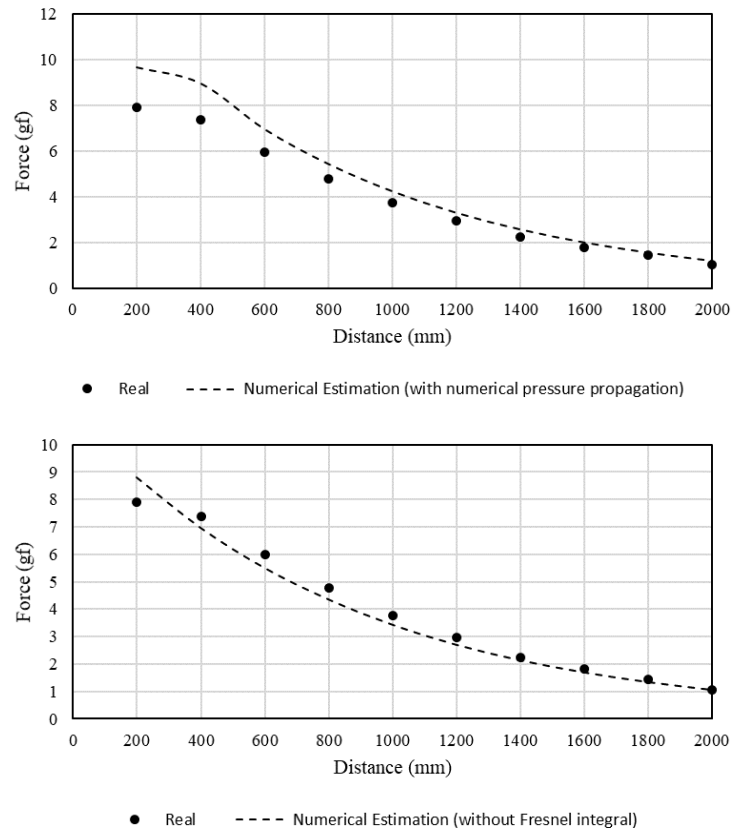


Fig. 2.8. Comparison of ray-acoustics-based model and measured value (Upper): Pressure field is numerically propagated considering the directivity of the transducers. (Lower): Pressure field is analytically propagated using a Fourier transform assuming a continuous rectangular aperture.

Figure 2.9 shows the experimental setup. An expanded polystyrene sphere is located is pinned on an electric balance. The author used a robotic arm to locate the AUPA device precisely. To align the force direction perpendicular to the surface of the electric balance, the beam axis is perpendicular to the surface of the electric balance. The green laser line is the reference to check that the alignment of the AUPA device and the sphere.

Figure 2.10 shows the measurement result depending on the angle and the distance from the AUPA. From the figures, it is shown that there is little difference between focusing-on-the-surface beam and focusing-on-the-center beam. The author stored the data as a table. By looking up the table, the system estimates acoustic radiation force on a balloon at a specific position and an angle.

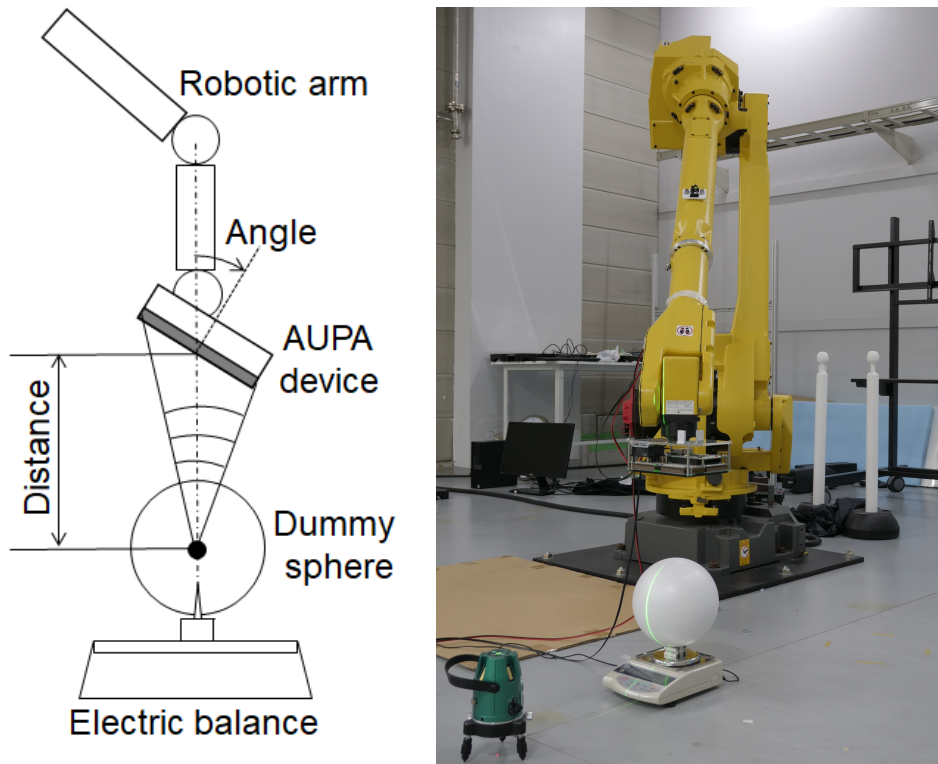


Fig. 2.9. Measurement of acoustic radiation force on a sphere. (Right) Schematic illustration. (Left) Actual setup.

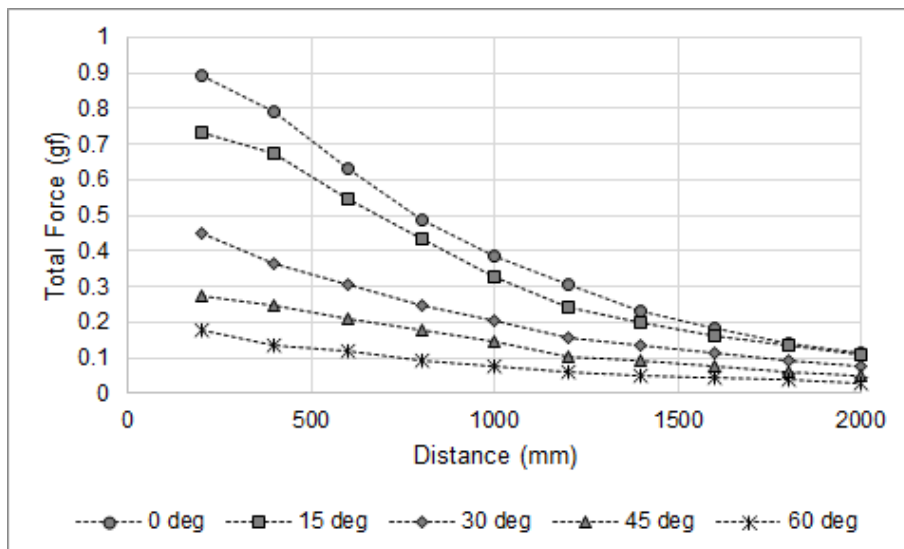


Fig. 2.10. Measured intensity of acoustic radiation force of focusing beam whose focus is at the center of the sphere.

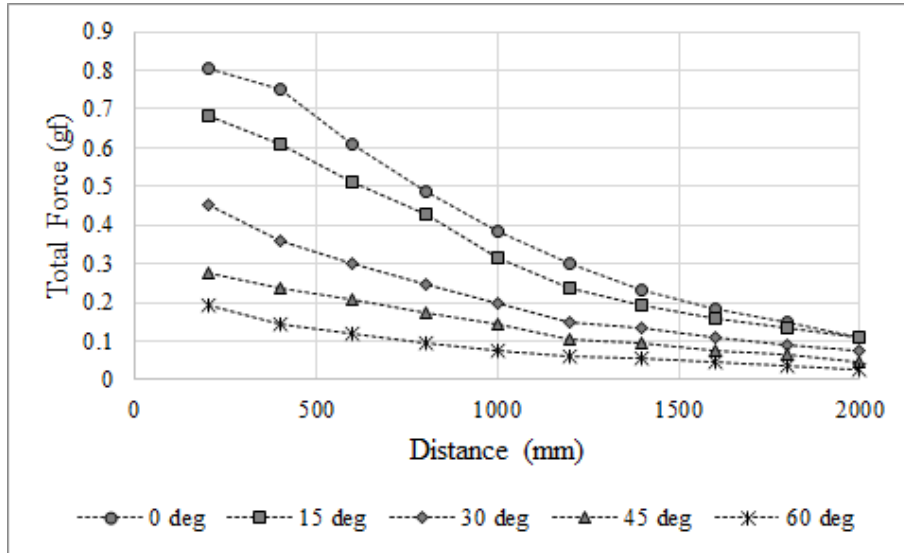


Fig. 2.11. Measured intensity of acoustic radiation force of focusing beam whose focus is on the surface of the sphere.

2.4 Analysis on Plane Wave Beam: Experimental Approach

The author developed an experimental ARF model for a plane wave beam by fitting a cubic polynomial to ARF measurement data.

The author constructed an experimental setup shown in Fig. 2.12 (right). An expanded polystyrene sphere of 200 mm diameter and 68.5 g weight was used as the dummy sphere. The sphere was suspended on an aluminum frame with a string of length 1,400 mm. An AUPA device was fixed at the same height as the sphere with its aperture directed toward it. The author drove all transducers at the maximum pressure amplitude p_M with the driving phase fixed to an identical value to emit a plane wave. The sphere oscillated about the equilibrium position, where tension, gravity force, and ARF were balanced. The author measured displacement of the equilibrium position caused by the ARF. Vertical displacement of the sphere was negligible, being a maximum of 0.043 mm. Kinect v2 was placed above the sphere for the measurement of the displacement, which detected

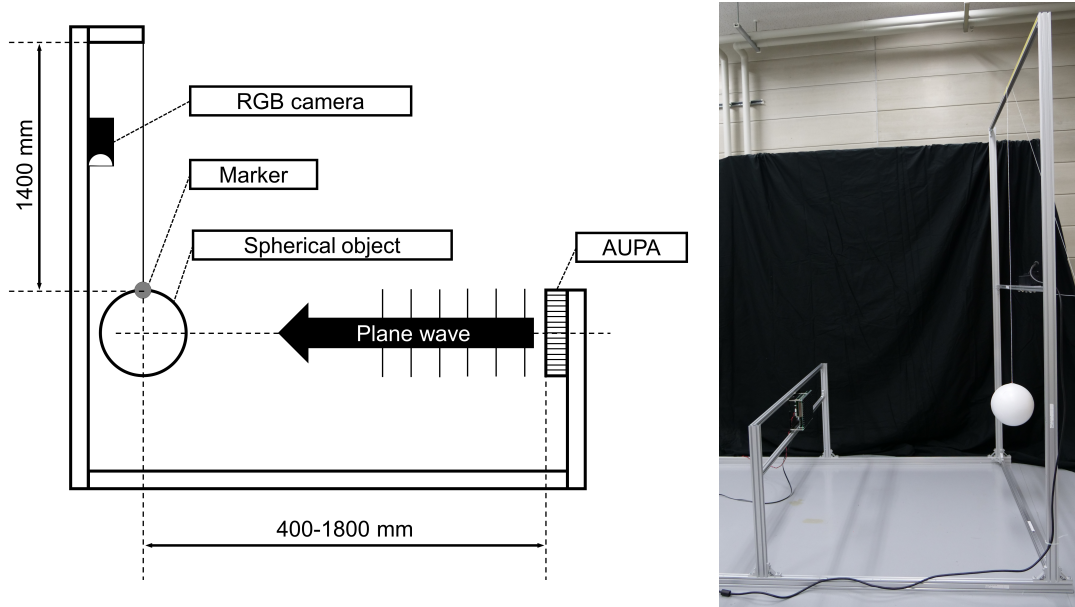


Fig. 2.12. (Left) Schematic diagram of the setup for measuring ARF on a rigid sphere. (Right) Actual settings for the experiment.

a visual marker attached to the top of the sphere. To measure the displacement accurately, we used its RGB camera in this experiment. The author obtained the equilibrium position by measuring the average position for 60 seconds. Fig. 2.13 shows the observed magnitude of ARF F_M with the maximum driving amplitude for a varying distance r between the aperture and the center of the sphere. As previously mentioned a cubic function was fitted to the measured data and obtained an ARF model described as follows:

$$F_M(r) = 2.71r^3 - 9.24r^2 + 6.77r + 3.60 \quad (2.45)$$

$$(0.4 \leq r \leq 1.8)$$

where the unit of $F_M(r)$ is mN and that of r is meter.

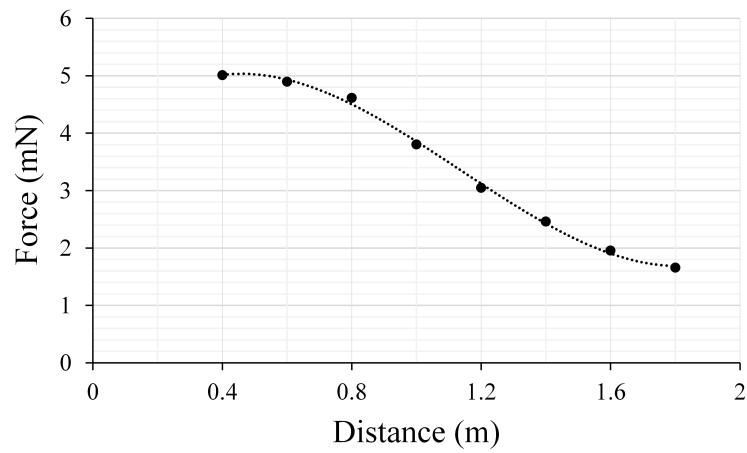


Fig. 2.13. Measured magnitude of acoustic radiation force on a rigid sphere of 200 mm in diameter for various distances from the aperture of the AUPA device. The black dots indicate the measured values. The dotted line indicates the polynomial approximate curve fitting the data points.

Chapter 3

Balancing Control by Multiple Phased Array Units

In this chapter, Force Balancing Control algorithm is presented. In Force balancing control algorithm, distributed AUPA devices emit axisymmetric ultrasound beams of appropriate power toward the target object such that the net force of ARF and gravity force controls it in proportional-integral-differential (PID) manner. This algorithm can be applied to cases where the beam diameter is smaller than the size of the object and if the AUPA devices are sparsely distributed such that the interferences between the AUPAs are negligible. The experiments demonstrate the manipulation of a sphere of 20 cm diameter more than one meter away from the transducers.

3.1 Dynamics

In this section we formulate a dynamics model based on the ARF model described in the previous section to express the behavior of the objects. Consider that AUPAs at positions $\mathbf{r}_1, \mathbf{r}_2, \dots, \mathbf{r}_N$ emits axisymmetric ultrasound beams toward a sphere at a position \mathbf{r} (Fig. 3.1). First, Let me consider ARF exerted by a single AUPA device at \mathbf{r}_i . Typical examples of axisymmetric beam include focusing beam and plane wave. The direction of the ARF is repulsive due to the

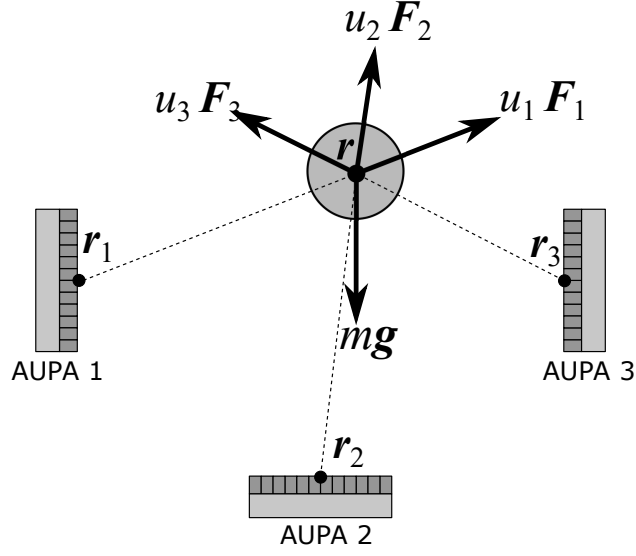


Fig. 3.1. Linear dynamics model of a sphere in balancing control algorithm.

symmetry. The magnitude is a function of the relative position between the sphere and the AUPA $\Delta \mathbf{r}_i = \mathbf{r} - \mathbf{r}_i$ as described in Chapter 2. The shape of the function depends on the kind of ultrasound beam and the AUPA specifications. When the AUPA is driven at the maximum amplitude p_M , the ARF \mathbf{F}_i is described as the follows:

$$\mathbf{F}_i = F(\Delta \mathbf{r}_i) \frac{\Delta \mathbf{r}_i}{|\Delta \mathbf{r}_i|} \quad (3.1)$$

where $F(\Delta \mathbf{r})$ is a function that the kind of the beam and the specifications of the AUPA determine. The shape of $F(\Delta \mathbf{r})$ is investigated in detail in Chapter 2. Because magnitude of ARF is proportional to the square of the driving amplitude p_i , or the power $u_i = (p_i/p_M)^2$ as indicated by Eq. (2.17), ARF \mathbf{f}_i at a driving amplitude p_i is described as follows:

$$\mathbf{f}_i = u_i \mathbf{F}_i. \quad (3.2)$$

Next, let me consider ARF exerted by multiple AUPA devices. Here, I assume that the interferences of ultrasound beams emitted from the AUPA devices are negligible. This approximation is valid if the diameter of the sphere is larger than the beam widths and the AUPA devices are sparsely distributed. Then, the resultant ARF is approximated by the sum of ARF that a single AUPA device exerts. The net force $\mathbf{f}_{\text{total}}$ applied to the sphere is described as the sum of ARF

and the gravity force as follows:

$$\mathbf{f}_{\text{total}} = \mathbf{F}(\mathbf{r})\mathbf{u} - m\mathbf{g} \quad (3.3)$$

$$0 \leq \mathbf{u} \leq 1 \quad (3.4)$$

$$\mathbf{F}(\mathbf{r}) = [\mathbf{F}_1, \mathbf{F}_2, \dots, \mathbf{F}_N] \quad (3.5)$$

$$\mathbf{u} = [u_1, u_2, \dots, u_N]^T. \quad (3.6)$$

where m is the mass of the object, and \mathbf{g} is gravitational acceleration. In the description of (3.4), $l_b \leq \mathbf{x} \leq u_b$ denotes that every element of vector \mathbf{x} is constrained by the following inequality condition: $l_b \leq x_i \leq u_b$. The solution of (3.3) provides the driving amplitudes allowing the net force $\mathbf{f}_{\text{total}}$ to be applied on the object at position \mathbf{r} .

3.2 Control

3.2.1 Algorithm

Here we consider how to determine the driving powers \mathbf{u} of the AUPA devices such that the net force a desired force \mathbf{f}_{tgt} is applied to the target object.

one thing to note is that the matrix \mathbf{F} in Eq. (3.3) depends on the position of the object. Now we assume the position \mathbf{r} is observed without delay. In that case, $\mathbf{F}(\mathbf{r})$ can be determined in real time by referring to the ARF model, which is represented by (3.7). To dynamically stabilize the position, $\mathbf{F}(\mathbf{r})$ should be estimated in a short time. To quickly estimate the ARF, ARF of various combinations of distances and beam angles in advance. We used two methods to estimate ARF from the data. One is to use a fitting curve, e.g. a cubic polynomial, of a relative distance as follows:

$$F_M(r) = a_3 r^3 + a_2 r^2 + a_1 r + a_0. \quad (3.7)$$

Table. 3.1 shows the coefficients for a plane wave beam and a focusing beam obtained from the measurement data in Chapter 2. Estimating using only a relative distance means that the transducer directivity and the change of the

virtual aperture size are negligible. This assumption is reasonable for cases where the beam angle is small considering that the transducers mounted on the AUPAs have 100° of half-amplitude full angle and that the virtual aperture size (see Fig. 2.1 left) is proportional to $\cos(\theta)$. Another method is to store the ARF data in a table and interpolate the data samples. In this approach, we used both a distance and a beam angle to estimate ARF. We used the former approach in the experiments in Chapter 6 and the latter approach in the experiments in Chapter 4. As shown later, it is confirmed that both approaches work. Predicting ARF by (2.19) requires complete information about the wave field and the object shape. Because the incident wave is diffracted and not perfectly planar due to the finite aperture of the AUPA, exact calculation of such incident and reflected wave field requires complex numerical analysis such as finite element method and boundary element method, which hinders real-time ARF prediction.

As previously mentioned a cubic function was fitted to the measured data (Fig. 2.12 and Fig. 3.2) and obtained an ARF model described as follows:

Beam type	$a_0(\text{mN})$	$a_1(\text{mN/m})$	$a_2(\text{mN/m}^2)$	$a_3(\text{mN/m}^3)$
Plane wave	3.60	6.77	-9.24	2.71
Focusing beam (focus on the surface)	9.17	-5.12	-0.858	0.712
Focusing beam (focus on the center)	10.5	-8.22	1.40	0.184

Table 3.1. Coefficients of a cubic polynomial fitted to ARF measurement data.

Then, (3.3) can be regarded as linear equations about \mathbf{u} of constant coefficient $\mathbf{F}(\mathbf{r})$ and $\mathbf{f}_{\text{tgt}} - m\mathbf{g}$. The solution to the equation yields duties that applies desired force.

The other thing to note is that AUPA devices can exert only repulsive force and cannot exert pulling force^{*1}. This is represented by the inequality condition

^{*1} For small spheres, there may be a case that AUPA can generate only pulling force. But, we focus on the case of a macroscopic sphere.

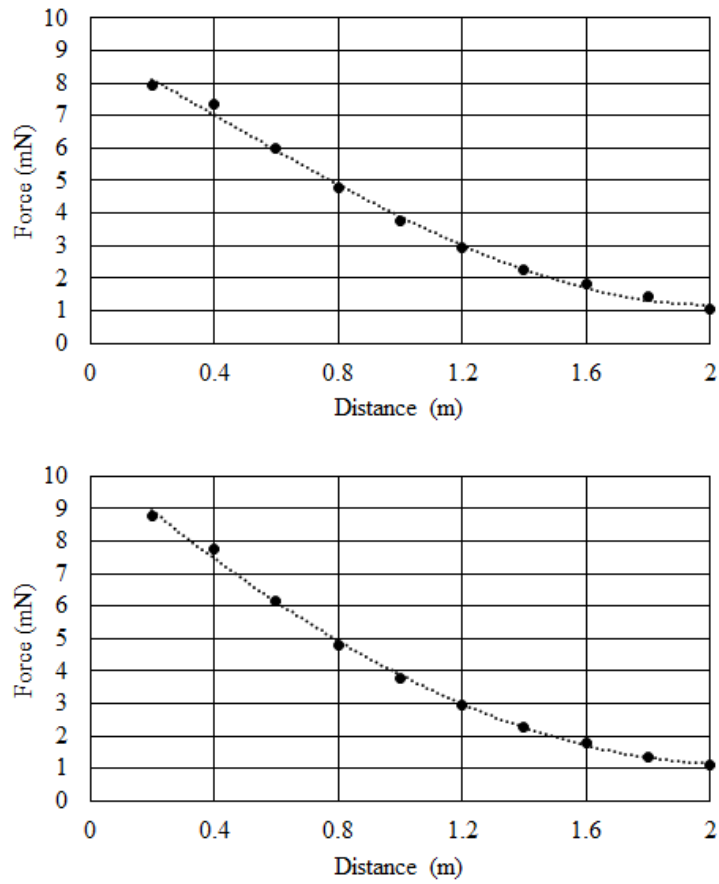


Fig. 3.2. Cubic polynomials fitted to ARF measurement data of focus on the surface (upper) and focus on the center (lower).

of Eq. (3.4). This limitation prevents us from using direct algebraic least squares methods such as a pseudo-inverse matrix method. Although the direct algebraic least squares solution promptly provides an exact solution, such solutions are likely to violate the feasibility constraint designated by (3.4). When we solve the problem, we should consider the constraint explicitly. Let me give an example to show the reason. For the sake of simplicity, we provide a two-dimensional example here. See Fig. 3.3, in which we want to apply upward force using three AUPAs arranged in triangular manner (fig. 3.3 left). In this case, the pseudo-inverse matrix method gives a solution of pulling force because the method yields the solution of the minimal square norm. Clearly, the solution is invalid. The correct solution is pushing the sphere with upper AUPAs with equal forces.

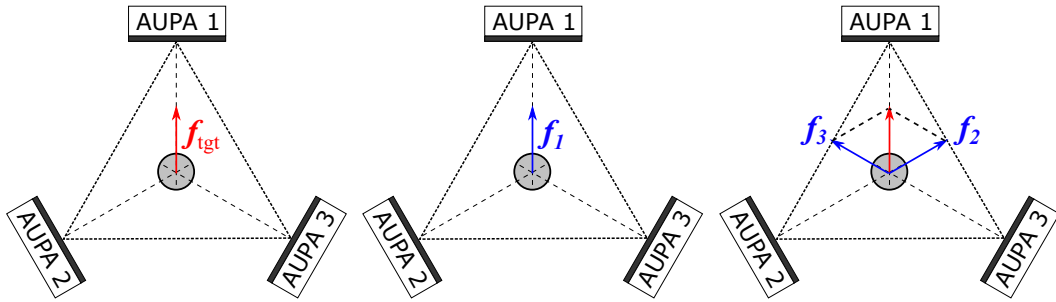


Fig. 3.3. Two-dimensional Example problem of finding duties that apply desired force on a sphere. (Left) Desired force. (Middle) Invalid solution yielded without consideration of constraints on duties. That contains pulling force by AUPA 1. (Right) Valid solution yielded with consideration on constraints on duties which consists of repulsive forces only.

One may say that offsets in powers may work. In other words, what about defining control variables as $u'_i = (p_i/p_M)^2 + 1/2$ ($-1/2 \leq u'_i \leq 1/2$). This strategy can avoid the problem stated just above. However, this strategy fails when the gravity force exists. Let me show another example shown in Fig. 3.4, in which we want to apply a downward force using three single-sided AUPAs. (This example is important for manipulation by single-sided transducers array, which is investigated in Chapter 4 in detail.) Again, L_2 norm minimization without inequality conditions yields an invalid solution that requires an AUPA to apply pulling force to overcome the offset force by the other two AUPA devices. Such situations easily occur.

To determine duties that apply the desired force while satisfying the inequality constraints, we formulate the following optimization problem that minimizes the square norm of the difference between the left- and right-hand sides of (3.3):

$$\text{minimize } \left| \mathbf{F}(\mathbf{r})\mathbf{u} - m\mathbf{g} - \mathbf{f}_{\text{tgt}} \right|^2 \quad (3.8)$$

$$\text{subject to } 0 \leq \mathbf{u} \leq 1. \quad (3.9)$$

This formulation is known as a semi-definite quadratic programming problem. This problem can be solved by iterative methods in a sufficiently short time for dynamic stabilization.

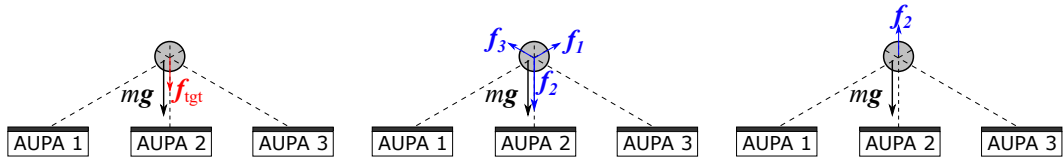


Fig. 3.4. Two-dimensional Example problem of finding duties that apply desired force on a sphere. (Left) Desired force. (Middle) Invalid solution yielded without consideration of constraints on duties. That contains pulling force by AUPA 2. (Right) Valid solution yielded with consideration on constraints on duties which consists of repulsive forces only. Note that this is not the only solution.

Our prototype system tries to find the \mathbf{u} by an iterative method. Instead, we chose to use an iterative method to guarantee that the solution meets the constraint. Such a solution provides not the smallest but still small squared errors. There are many quadratic programming solver available [60, 61]. We confirmed that a quadratic programming solver provided in the Dlib Machine Learning Library and CGAL works.

Strictly speaking, the time for the acoustic waves to arrive at the object surface from the AUPA is finite. Therefore, it causes a delay in the applied ARF. However, for the size of our workspace, this delay is in the order of milliseconds, hence it is negligible compared to the moving speed of most objects, including the ones in our experiments. For this reason, we regard the generation of ARF as instantaneous one and we exclude any dynamic term in the force generation model described by (3.3).

3.2.2 Stabilization

Stabilization of the object requires a restoring force to suppress the disturbance. We used a Proportional-integral-differential (PID) controller to calculate such a restoring force. With the position of the object observed by the tracking sensor,

the force is calculated as follows:

$$\mathbf{f}_{\text{total}} = -k_p \Delta \mathbf{r} - k_d \dot{\Delta} \mathbf{r} - k_i \int_0^t \Delta \mathbf{r} dt' \quad (3.10)$$

where $\Delta \mathbf{r}$ is the error in the position, $\dot{\Delta} \mathbf{r}$ is the error in the velocity, k_p , k_d , and k_i are user-defined parameters, and t denotes time. The parameter value determined in the following experiments is shown in Table 3.2.

Parameter	Notation	Value	Unit
Proportional gain	k_p	6.0×10^{-3}	N/m
Differential gain	k_d	2.2×10^{-2}	$N \cdot s/m$
Integral gain	k_i	2.0×10^{-4}	$N/(m \cdot s)$

Table 3.2. PID control gains.

3.2.3 Maximum Controllable Weight and Workspace

Because the applicable ARF depends on the object position, so does the maximum weight the system can manipulate. The maximum weight at position \mathbf{r} can be obtained by optimizing \mathbf{u} such that it maximizes the vertical force under the condition that lateral force is zero. Optimizing both control variables \mathbf{u} and position \mathbf{r} determines the maximum weight it can support. The prototype can manipulate an object of up to 8.54 mN weight.

In addition to counteracting gravity, stabilization requires the application of an additional restoring force when the position of the object slightly deviates from the target position. Therefore, the maximum weight it can practically manipulate in a robust manner is smaller than the value mentioned above.

Here, we introduce the control variables $\bar{u}_i = (p_i/p_M)^2 - \frac{1}{2}$. By substituting \bar{u}_i into (3.3), the force exerted on the object can be represented as follows:

$$\mathbf{f}_{\text{total}} = \mathbf{F}(\mathbf{r})\bar{\mathbf{u}} + \mathbf{g}' \quad (3.11)$$

$$-\frac{1}{2} \leq \bar{\mathbf{u}} \leq \frac{1}{2}. \quad (3.12)$$

\mathbf{g}' is given as $\mathbf{g}' = m\mathbf{g} + \frac{1}{2} \sum_{i=0}^{N-1} \mathbf{F}_i$. Here, we define the workspace as a region where the object has three translational DoF. This depends on the weight of the

object. We propose checking the translational DoF at position \mathbf{r} by finding a solution to (5) that minimizes $|\bar{\mathbf{u}}|_\infty$, where $|\bar{\mathbf{u}}|_\infty = \max\{\bar{u}_0, \bar{u}_1, \dots, \bar{u}_{N-1}\}$. Such a solution can be obtained using a linear programming technique. If and only if $|\bar{\mathbf{u}}|_\infty$ is smaller than $1/2$ and the rank of the matrix \mathbf{F} is 3, the object has three translational DoF at position \mathbf{r} . A set of such points where a 3-DoF force can be generated was considered as the workspace. Examples of the workspace of the prototype system are shown in Fig. 8. Inside the workspace, the object can move anywhere at a moderate speed.

3.3 Manipulation Experiment

3.3.1 Implementation of Manipulation System

We constructed a prototype system to conduct manipulation experiments. We used the same AUPA device as that applied in [17]. The specifications of the AUPA devices are described in Section 2.2.

Figure 3.6 shows the definition of the coordinate system and the arrangement of the AUPA devices in our prototype system. Five AUPA devices were installed in the system. One AUPA had its aperture oriented in the vertical direction, and two pairs of opposing AUPA devices were arranged orthogonally in a horizontal plane at a height of 1,085 mm.

We used Microsoft Kinect V2 for object tracking. Although Kinect V2 has an RGB and a depth camera, the prototype system uses only the depth one. The prototype system captures the object position and refreshes the driving amplitudes and phases of all the transducers every 50 ms.

The balloon is assumed to have a rigid-body and sound-hard boundary because solids in the air because the characteristic acoustic impedance of the air is much smaller than that of solids [12].

3.3.2 Performance of Suspension at a Fixed Position

Proportional Control

To gain an insight into the dynamics, we present a result of the case only proportional (P) gain is applied. Figure 3.7 shows the recorded position for about 60 seconds.

As shown in the figure, the position oscillates about the target position. The reason should be that the damping force generated by the drag force is too small to suspend such a macroscopic object. This indicates that differential control is required for stabilization. It is also shown that the average altitude is below the target value. This is due to the gravity force is larger than expected. To compensate for the mismatch in weight expectations, integral control should be applied.

Proportional-integral-differential (PID) Control

We conducted an experiment to suspend an object at a fixed 3D position.

We used a spherical balloon of 200 mm in diameter as the object to be manipulated, which was filled with helium gas. Pieces of adhesive tape were stuck onto the balloon surface to adjust the weight of the object, to be as close as possible to air buoyancy. The resultant force of gravity and buoyancy in the air during the experiment was 1.3 mN downward. The target position was set to $r = [0 \ 0 \ 1300]^T$. We initially placed the object near the target position inside the workspace by hand.

The recorded trajectory is shown in Fig. 3.8. As can be seen, the object position successfully converged to the target position.

Note that the object is not perfectly spherical, as shown in Fig. 3.9. This implies that the proposed method is robust against the unevenness of the object shape.

3.3.3 Performance of Translation Maneuver

Next, we conducted an experiment to move the object along a specified route.

The route is shown in Fig. 3.10. We specified six target positions in the first quadrant of the xy plane, considering the symmetric arrangement of AUPA devices. The target position was sequentially updated every 10 s. As with the stationary suspension described in the previous section, we used a spherical helium-filled balloon with a diameter of 200 mm and adhesive tape applied as described in the previous experiment. The resultant force in the air during the experiment was 3.13 mN downward. The recorded trajectory and control variables are shown in Fig. 3.11. As shown in Fig. 3.11, the object followed the sequentially changing target positions. As shown in Fig. 3.12, we succeeded in stabilizing the object even at a point not right in front of the AUPA apertures. Because the same manipulation is considered possible in the other quadrants, this result indicates that a 1 meter diagonal manipulation is possible with the proposed method.

The tracking accuracy varied according to the target position. At positions A, B, D, and F, the actual positions converged to the target positions within a deviation of 20 mm within 10 seconds. Meanwhile, deviations of 40 to 60 mm were observed at positions C and E. Such deviations may be due to the upper limit of the actuation force that the vertical AUPA device could exert. At these positions, the control variables reached their maximum at these positions as shown in Fig. 3.11.

3.3.4 Evaluation of the Workspace

We verified the actual workspace size of the prototype. For each of the altitudes 1300mm, 1500mm, and 1700mm, the target position is moved by 50mm in the direction of the x axis and the xy direction every 20 seconds from the center of the workspace shown in the figure 3.13. The error from the target position was recorded. Figure 3.14 shows a plot of the deviation from the target position with respect to the distance from the center.

3.4 Discussion

In this paper, we demonstrated a new robotic framework where a lightweight object with no actuators or batteries is manipulated in the air by acoustic driving forces remotely provided from the workspace. Technically, it is a sensor-feedback-based meter-scale 3D acoustic manipulation of a sphere 10 times larger than the sound wavelength. This was achieved by dynamically controlling the directions and amplitudes of the plane waves emitted from distributed airborne ultrasound phased array devices. Based on the experimentally obtained radiation force model, we formulated a 3D motion control algorithm based on PID control. Experiments on object manipulation were conducted, the results of which demonstrated that dynamic meter-scale position control is possible within the workspace. The position error increased at a specific position where the available maximum control force was insufficient for the feedback control criteria of the object movement.

The primary limitation of the system is that manipulated objects must be extremely light, ensuring their buoyancy is almost in balance with the gravity force. This is because a force that an AUPA provides is less than 100 mN typically. In addition, the lateral movement of the objects in our current prototype system is much slower than that of quadrotors. Another major limitation is that the movement of the robot is confined within the workspace and vulnerable to ambient wind, which renders it unsuitable for outside applications.

Despite such restrictions, the proposed system possesses its intrinsic advantage that stable long-time 3D operation of robots with multi-DoF is possible without the need for onboard batteries. For instance, the proposed framework can be applied to a 24-hour indoor surveillance system with no blind spots when a miniature camera is mounted on the flying object. Another application could be an airborne transportation robot that can carry lightweight items to a specific user in a room where many obstacles such as tables, chairs, or wiring exist on the floor. It should be noted that our method does not require numerous ultrasound sources installed across the workspace. A sparse arrangement of AUPAs is sufficient for the correct

operation of our system, which is important for practical use.

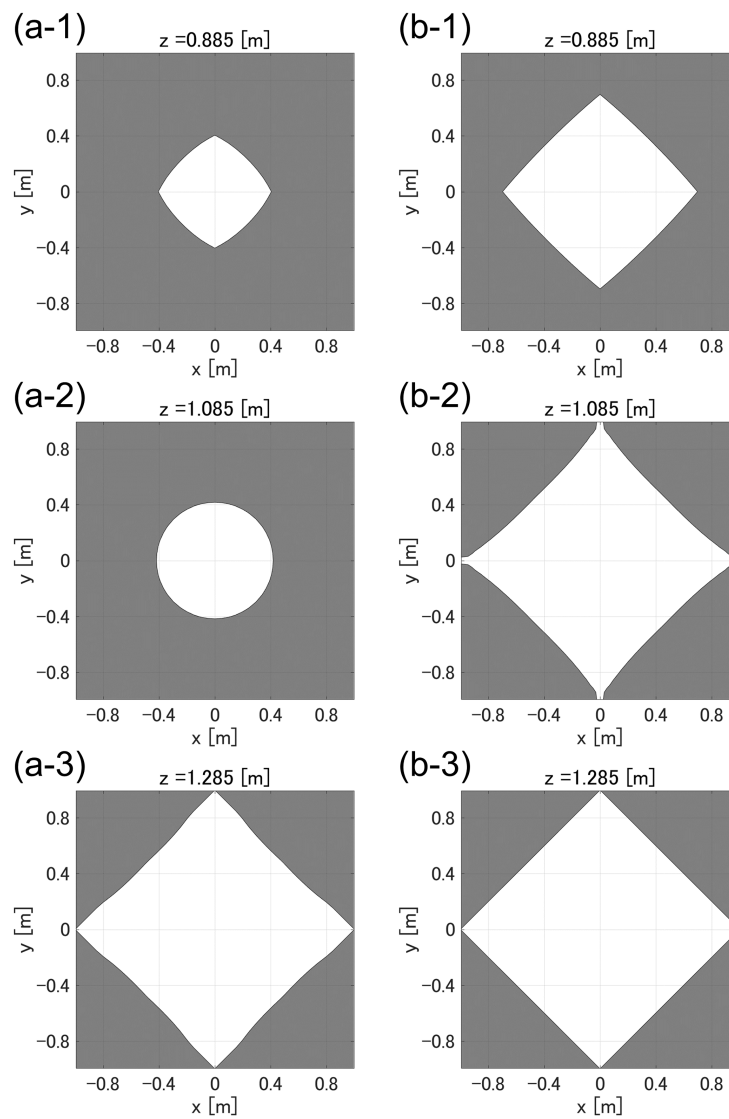


Fig. 3.5. Workspace of the prototype system. The object has three translational DoF inside the white area. The work volume for an object of 1.3 mN in weight is shown in the left-side column, namely, (a-1), (a-2), and (a-3), and that for an object of 3.1 mN in effective weight is shown in the right-side column, (b-1), (b-2), and (b-3). The top, middle, and bottom images show the workspaces at an altitude of 885, 1085, and 1285 mm, respectively

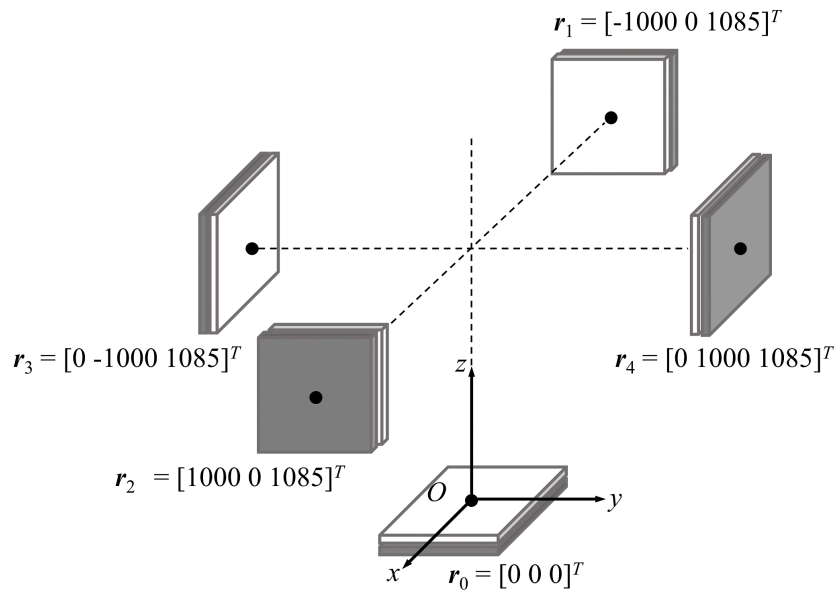


Fig. 3.6. Definition of coordinate system and arrangement of AUPA devices in the prototype system

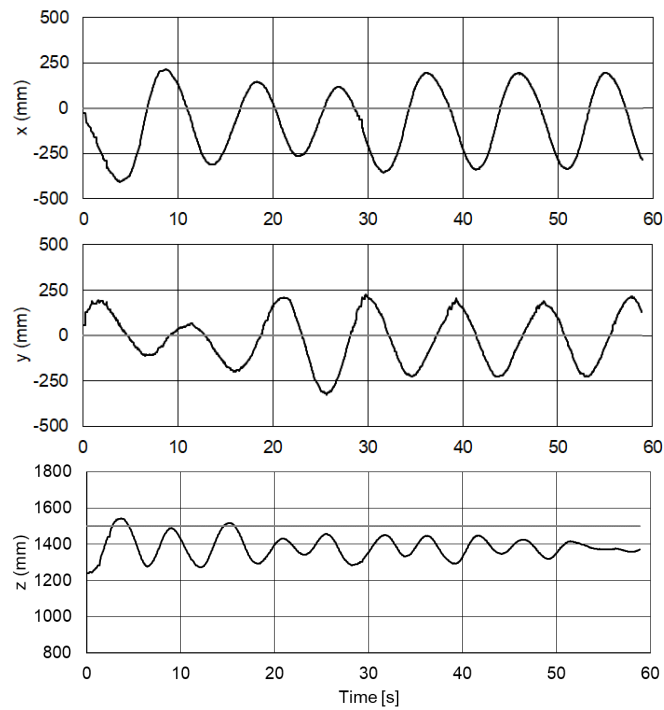


Fig. 3.7. Recorded trajectory in the case only proportional gain was applied. Black and gray lines indicate recorded and target values respectively.

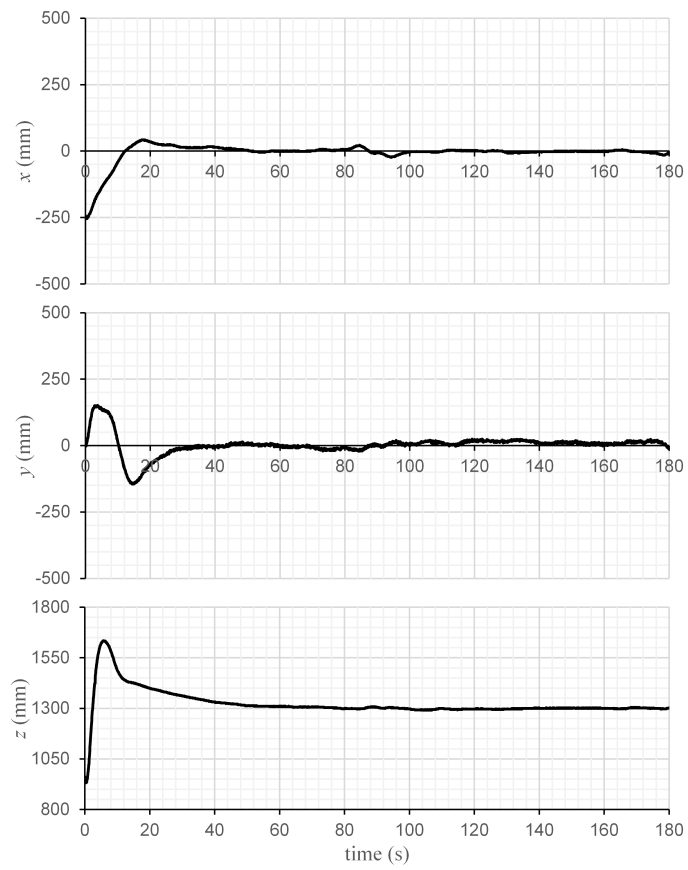


Fig. 3.8. Recorded trajectory during the stationary suspension task

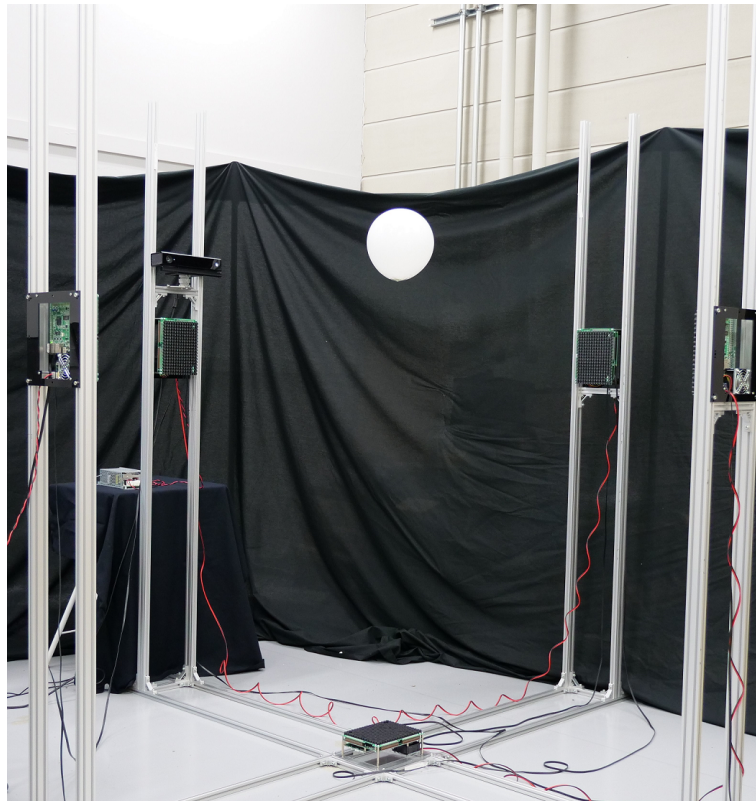


Fig. 3.9. A spherical object suspended at a fixed position.

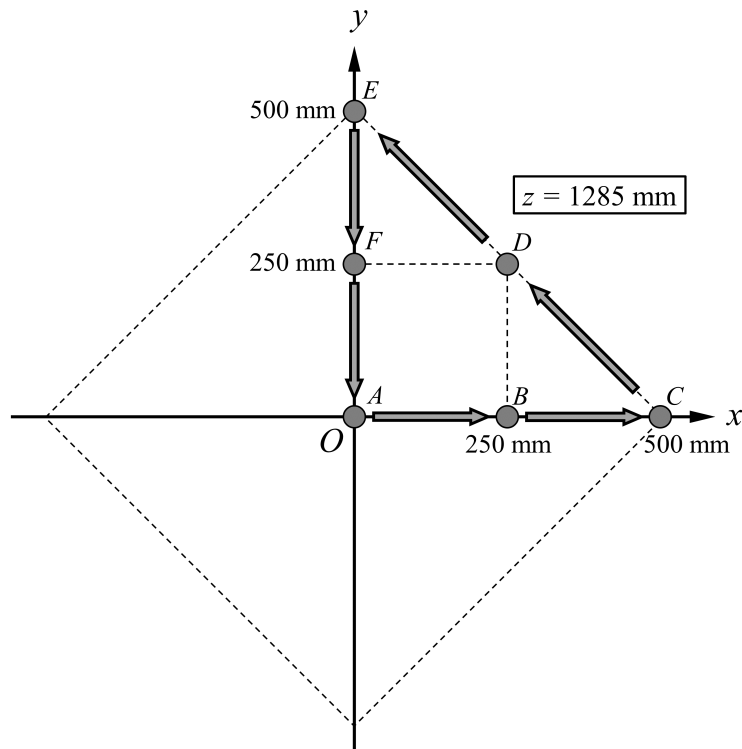


Fig. 3.10. Route in the translation task

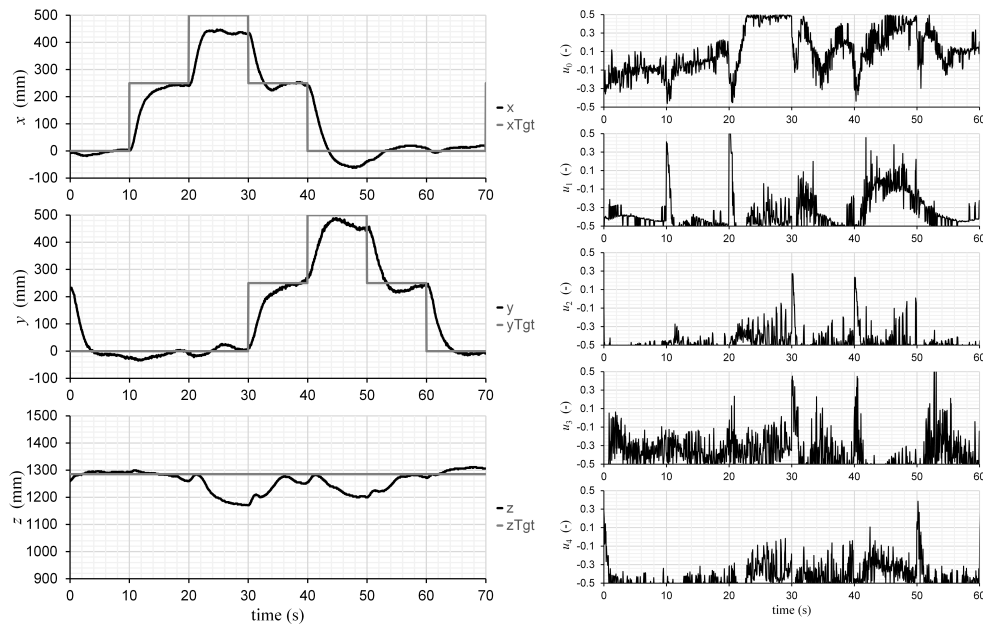


Fig. 3.11. Record of positions (left) and control variables (right) during the translation task. The black lines indicate the recorded position of the object. The gray lines in the left figure indicate the target position.

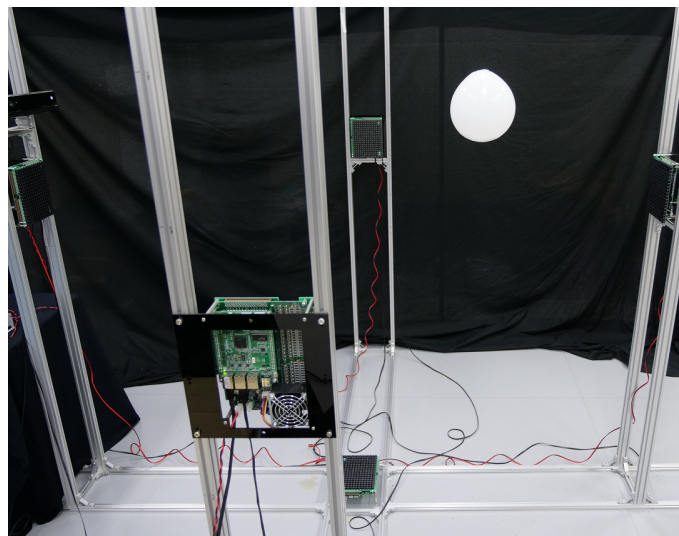


Fig. 3.12. A sphere suspended at a position $r = [0 \ 250 \ 1285]^T$ mm

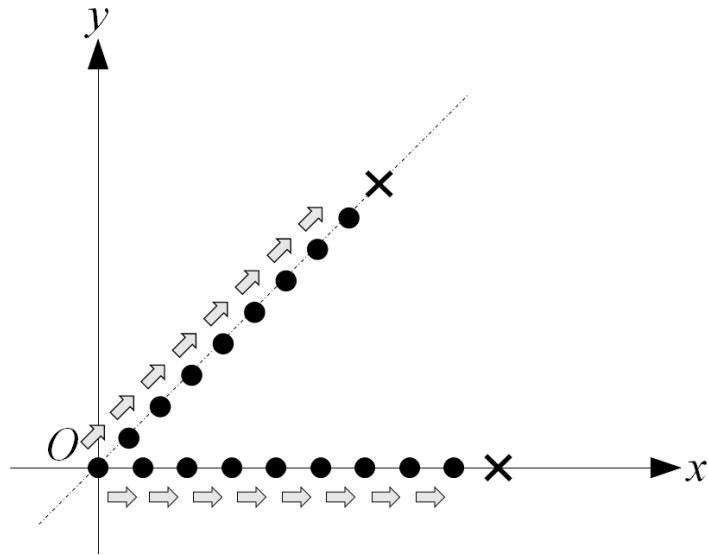


Fig. 3.13. Translation sequence for workspace analysis.

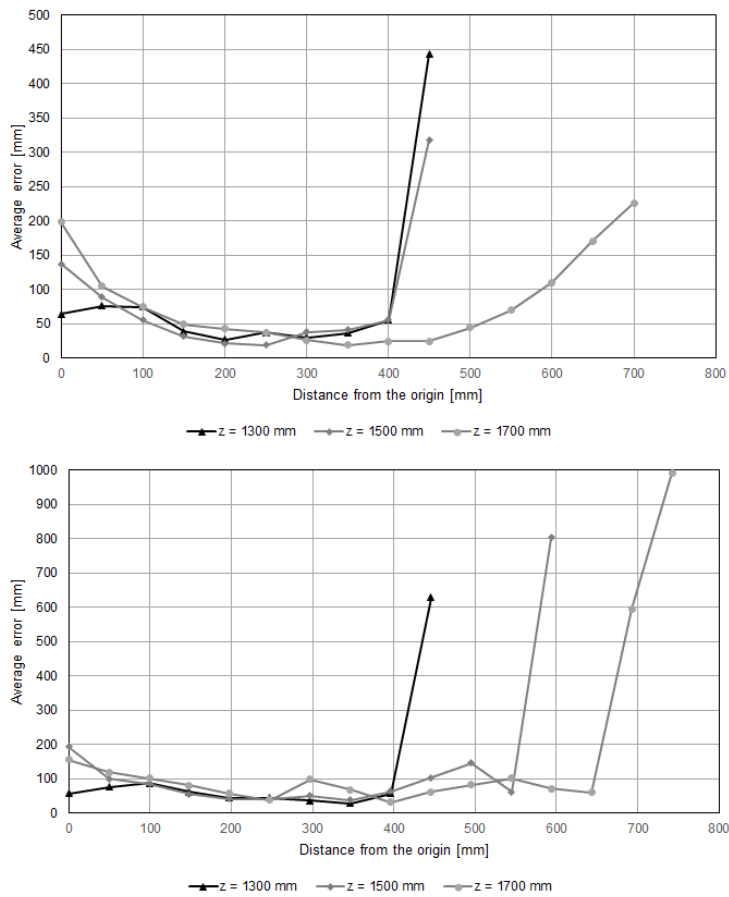


Fig. 3.14. Average position error at distances from the origin at various altitudes.

Chapter 4

Manipulation by Single-sided Array for Scalable Workspace

In Chapter 3, I discussed a control algorithm and analyzed the workspace for a given arrangement of AUPAs. In this chapter, I discuss the inverse problem: how to arrange AUPA to achieve the desired workspace. This problem always occurs when we apply the manipulation system to a real application. Of course, enclosing the whole workspace with AUPA devices satisfies the workspace requirement. However, it is unpractical because it suffers from low visibility, poor access to the floating object, and complex installation process. For practical installation, a sparse arrangement is desirable. The trade-off makes this problem untrivial. To meet such needs, the author proposes to design workspace by arranging AUPA devices in a single-sided lattice manner (Fig. 4.1). Especially, if the balloon is filled with helium gas and the buoyancy is greater than gravity, the balloon position can be controlled only by the AUPA placed on the ceiling.

4.1 Design of Lattice

4.1.1 Design Criteria of AUPA Arrangement

To make sure that the object can stably float at specified position, what condition on AUPA arrangement should be satisfied? In the case of triangular lattice,

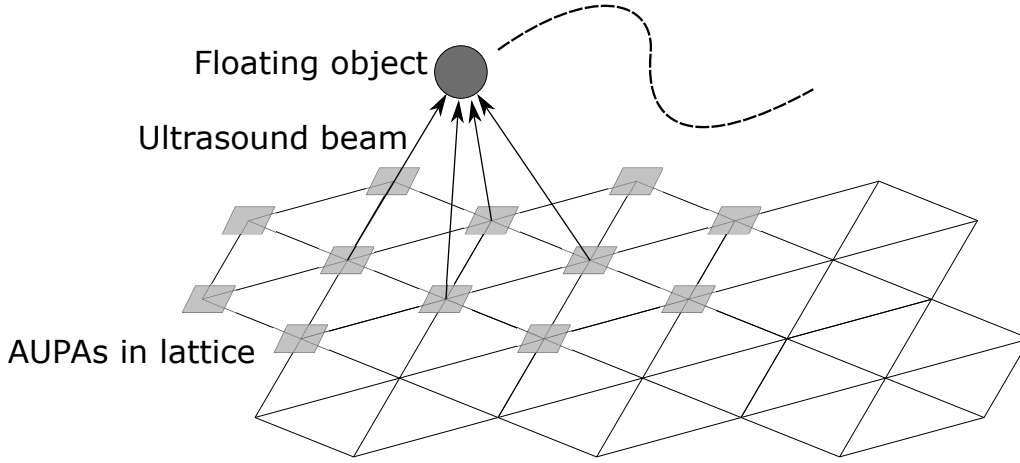


Fig. 4.1. Acoustic manipulation by single-sided AUPA devices arranged in lattice.

how to determine the interval of AUPA devices L ? As stated in chapter 3, the requirement for stable position keeping is that AUPA devices can apply force to counteract the gravity force and the disturbances. The maximum applicable force around the equilibrium, where the gravity force and ARF are balanced, changes according to the direction. I define *force margin* M along a direction \mathbf{e} as the minimum available force as following:

$$M = \min|\mathbf{e} \cdot (\mathbf{F}\mathbf{u} + m\mathbf{g})| \quad (4.1)$$

$$0 \leq \mathbf{u} \leq 1$$

We adopt force margin as the criteria to evaluate the goodness of an AUPA arrangement for keeping an object at the specified position. The goodness of AUPA arrangement for keeping.

$$\mathbf{F} = [\mathbf{F}_1 \mathbf{F}_2 \cdots \mathbf{F}_N] \begin{bmatrix} u_1 \\ u_2 \\ \vdots \\ u_N \end{bmatrix} \quad (0 \leq u_i \leq 1) \quad (4.2)$$

where \mathbf{e} is a unit vector of an arbitrary direction. The condition is graphically described in Fig.4.2. The available force set is the polyhedron that consists of all weighted sum of ARF vectors for AUPA devices. To counteract the gravity,

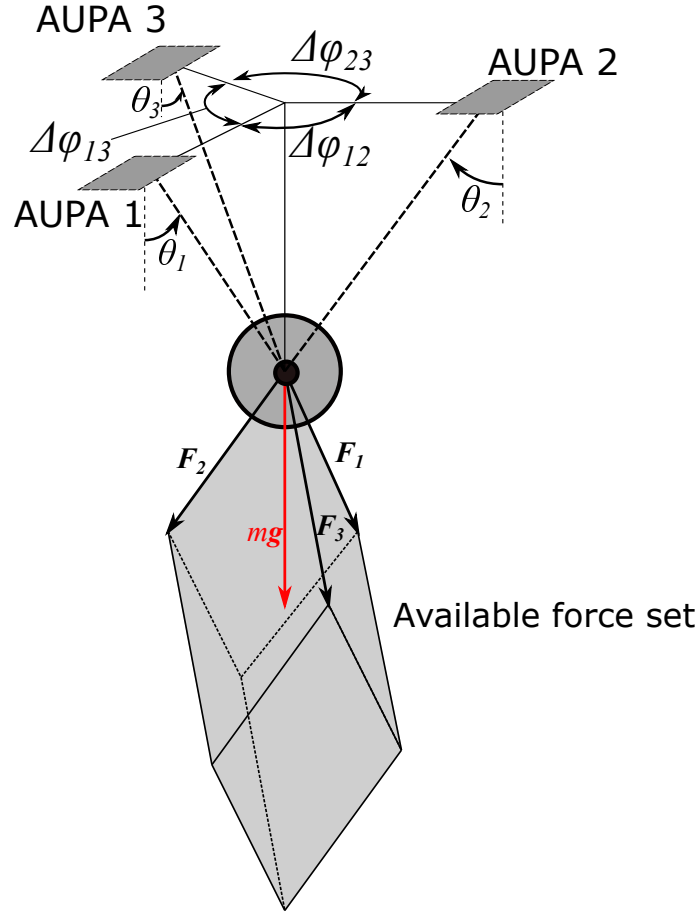


Fig. 4.2. Available force set.

it should be inside the polyhedron. The margin is the minimum distance from equilibrium force point $\mathbf{F}_{\text{eq}} = -m\mathbf{g}$ to the convex hull of points $\mathbf{F}_1, \mathbf{F}_2, \dots, \mathbf{F}_N$.

4.1.2 Design of AUPA Lattice

Here, we aim to make the margin larger than the specified value ε at all positions in the workspace at target altitude h . One way to satisfy the requirement at a position \mathbf{r} is to have at least three maximum radiation force vectors that satisfy the following three conditions:

- (A) The vertical component must be greater than or equal to the threshold $F_{z(\text{min})}$.
- (B) The horizontal component must be greater than or equal to the thresh-

old value $F_{r(\min)}$.

- (C) The maximum value of the azimuth angle of each maximum radiation vector is less than $\varphi_{(\max)}$ degrees

Conditions (A) and (B) are about one AUPA. If conditions (A) and (B) are satisfied at position \mathbf{r} for the AUPA, we say that the AUPA is *effective* at position \mathbf{r} . We define *effective area* of an AUPA as positions set at the target altitude where the AUPA is effective. Assuming that the AUPA device has axisymmetric force directivity, The effective area can be described by two radii (Fig. 4.4). These radii are determined from an ARF-directivity plot. Let me show an example of determining the radii from the threshold values $F_{z(\min)}$ and $F_{r(\min)}$ using the case of manipulation by focusing beams. Figure 4.3 plots vertical and radial component of ARF of focusing beam at the altitude of 1000 mm. Suppose that the threshold values of a vertical and horizontal components of ARF are set to 1.0 mN and 0.5 mN respectively. In this case, to meet the requirement on a vertical component, the distance between a target point and the AUPA should be smaller than threshold value r_{\max} (Fig. 4.3 upper). On the other hand, to meet the requirement on a horizontal component of ARF, the distance should be larger than another threshold value r_{\min} . After all, effective area is the area that is enclosed by the circle of radius r_{\max} and that of r_{\min} . (Of course, r_{\max} may be determined by the requirement on a horizontal component according to the threshold value.)

To satisfy condition (A) and (B), all the area of workspace should be have at least three effective AUPA devices. If the inner boundary circle of each AUPA device is inscribed in the outer boundary circles of neighboring AUPA devices, the condition is clearly satisfied. This requirement yields the first condition on the AUPA interval L .

$$L \leq r_{\max} - r_{\min}. \quad (4.3)$$

Next, let me consider condition (C), a requirement on the azimuthal angles. Figure 4.6 shows four AUPA devices in the lattice. For the symmetry of hexagonal lattice, I only need to consider in triangle $\triangle BEH$. Note that the number of

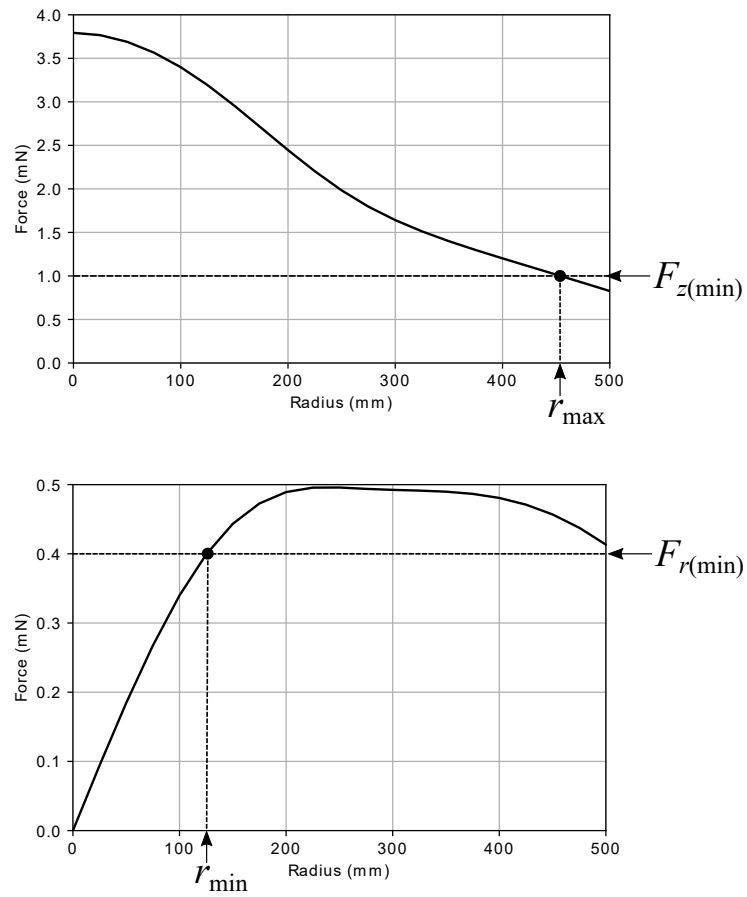


Fig. 4.3. Inner and outer radii of effective area for focusing beam.

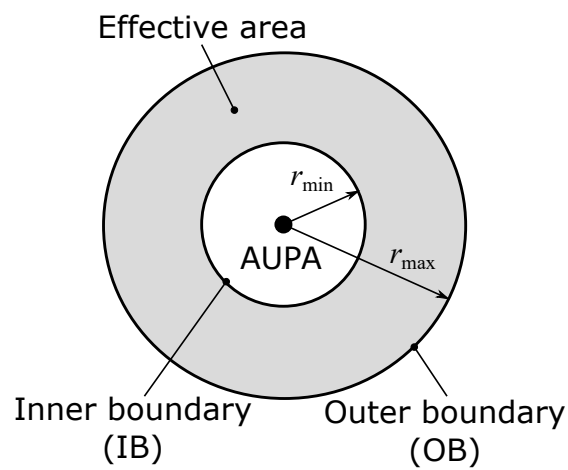


Fig. 4.4. Effective area of an AUPA.

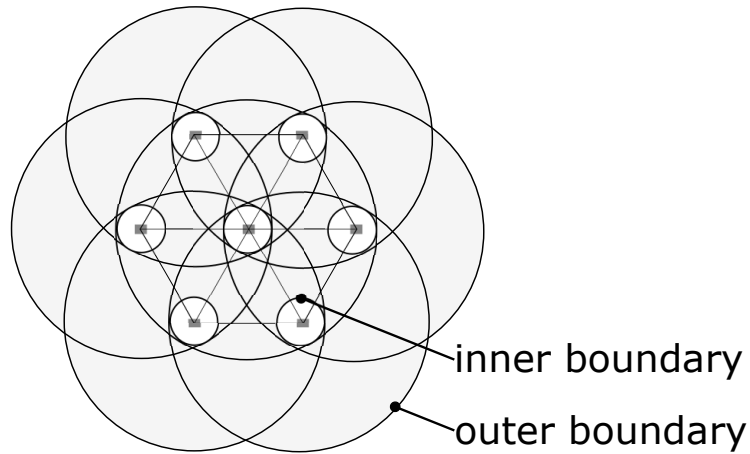


Fig. 4.5. Geometric relationships among effective areas of neighboring AUPA devices.

effective AUPA devices depends on the position. If the following condition

$$L \leq \frac{\sqrt{3}}{2} r_{\max} \quad (4.4)$$

is satisfied, all the points in $\triangle BEH$ have more than three effective AUPAs. This may be automatically satisfied by condition of Eq. (4.3). If it is not satisfied, the gray area in the figure has three effective AUPAs. In this region, azimuthal angles are likely to be small. Therefore, I analyze maximum azimuth angles in this area. The maximum azimuthal angles become largest on point F and point G. Figure 4.7 shows the maximum azimuth angle of each point. As shown in this figure, condition (C) also impose a limit on AUPA interval length in terms of r_{\max} . In this figure, the limit for the case of a maximum azimuthal angle 140 deg is shown. As a result, the second requirement on AUPA interval is described as following:

$$L \leq \alpha r_{\max} \quad (4.5)$$

where $\alpha = (L/r_{\max})_{\max}$, which can be determined from figure 4.7.

After all, condition (A), (B), and (C) at target altitude h are equivalent to the two requirements on AUPA interval represented by (4.3) and (4.5).

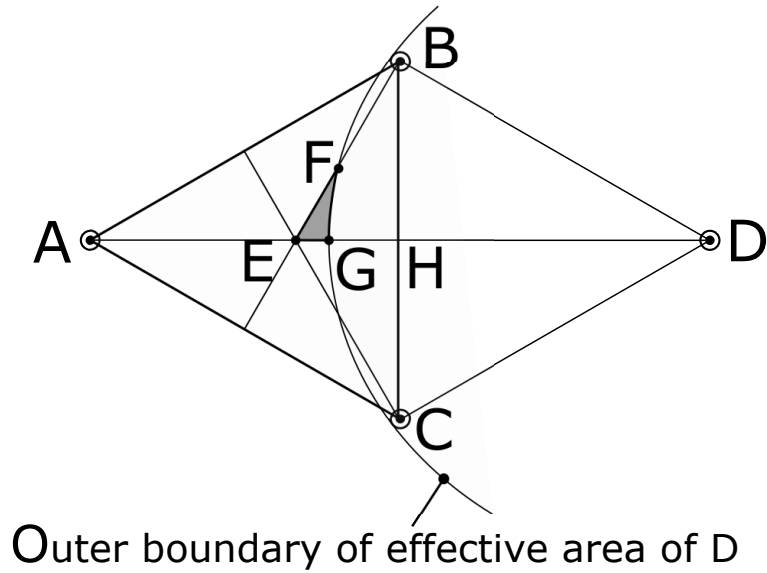


Fig. 4.6. Geometric relationship between AUPAs.

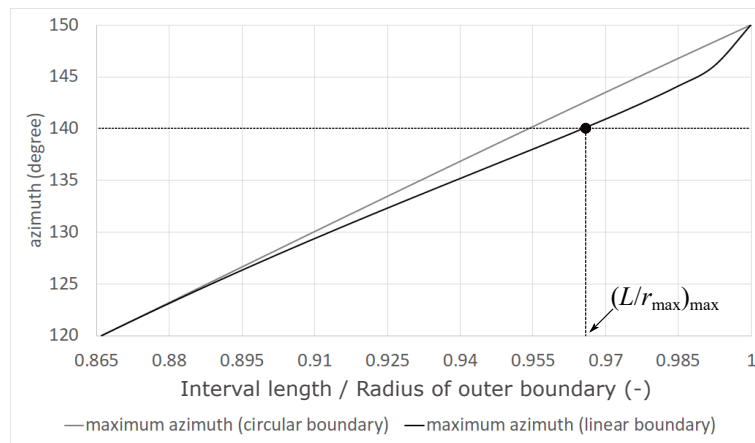


Fig. 4.7. Azimuth on the linear boundary (the line EF) and the circular boundary (the arc FG) in Fig. 4.6

4.2 Manipulation of Multiple Objects

Objects in close proximity share the AUPA devices. To accommodate the situation, time-division multiplexing of beam direction is implemented. To keep the average of the ARF the same, the beam power of the beam is multiplied by the number of objects that shares the AUPA device.

4.3 Translation Maneuver Experiment

An experiment of lateral translation maneuver was conducted to demonstrate the scalability of the workspace and multiplexing control. The target altitudes from the transducers were set to 500 mm and 700 mm.

4.3.1 Experimental Setup

Figure 4.8 shows the experimental setup. The AUPA devices were installed on the ceiling so that the heights of the apertures are 1931 mm from the floor. The arrangement is intended to suspend objects that ascends naturally by their buoyancy (Fig. 4.9). In this experiment, helium-filled spherical balloons of approximately 20 cm diameter were used as target objects. The threshold value of horizontal ARF, vertical ARF, and azimuth angles were set to 0.43 mN, 0.6mN and 130 degrees respectively (Fig. 4.10). Note that the requirement on the azimuth angles is automatically satisfied by the other requirements. Following the guideline described in Section 4.1, the interval of the AUPA devices was set to 520 mm (Fig. 4.11). AUPA is arranged to draw a hexagonal lattice, and in the prototype, two hexagons are arranged. If the balloon can be moved from one hexagonal region to the adjacent hexagonal region, it is considered that the moving range can be expanded as much as desired by expanding this hexagonal lattice arrangement.

4.3.2 Result

Figure 4.13 shows the balloons moving to the adjacent blocks. Figure 4.12 shows the recorded trajectory of the two objects. The figures shows that the objects succeeded in translation to adjacent along the target trajectory. The result demonstrates the lateral scalability of the workspace, that is, Floating objects can move further by moving by cell.

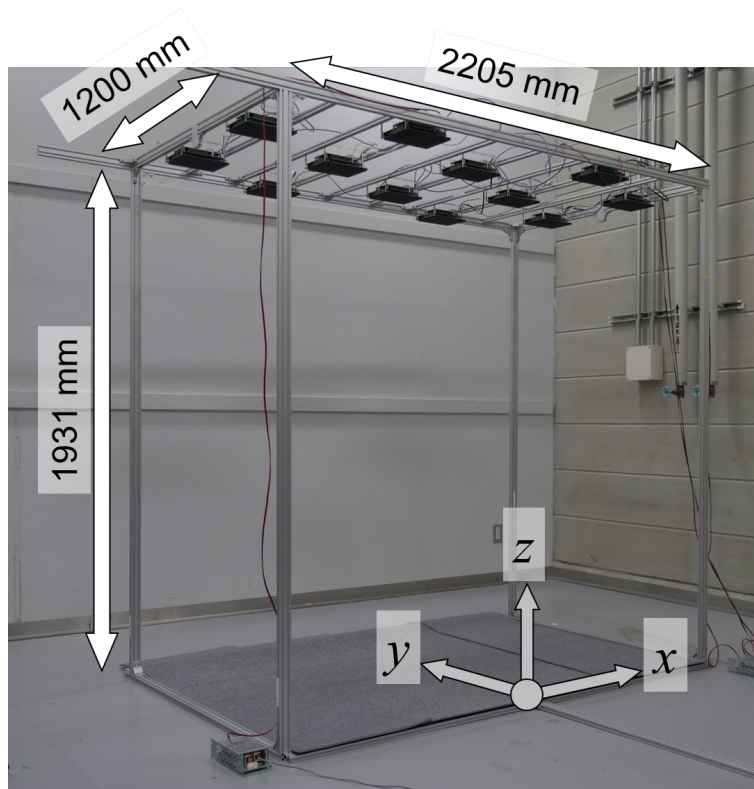


Fig. 4.8. Installation of ceiling-sided AUPA devices.

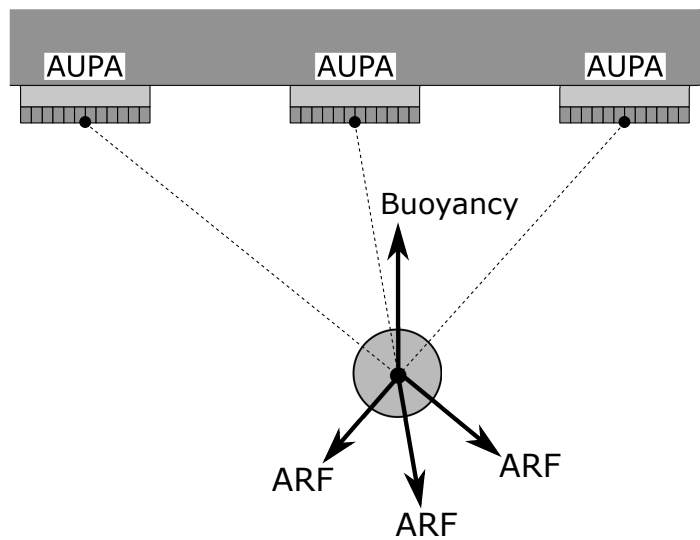


Fig. 4.9. Schematic illustration of AUPA devices suspending an object that naturally ascends.

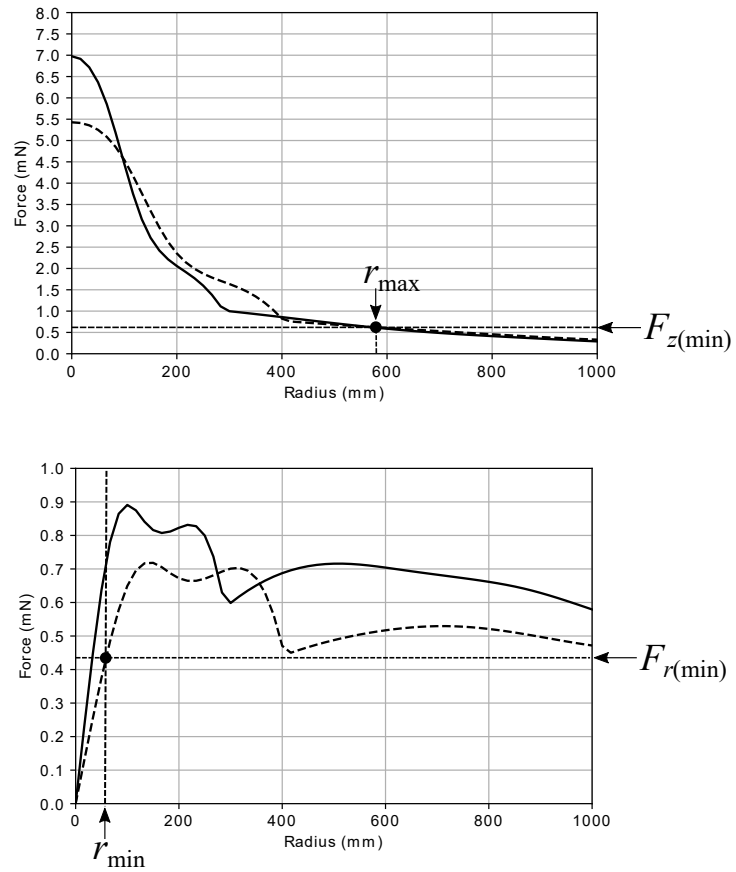


Fig. 4.10. Vertical and horizontal ARF applied by a single AUPA device at the target altitudes. Black lines indicate ARF at an altitude of 500 mm. Dotted lines indicate ARF at an altitude of 700 mm.

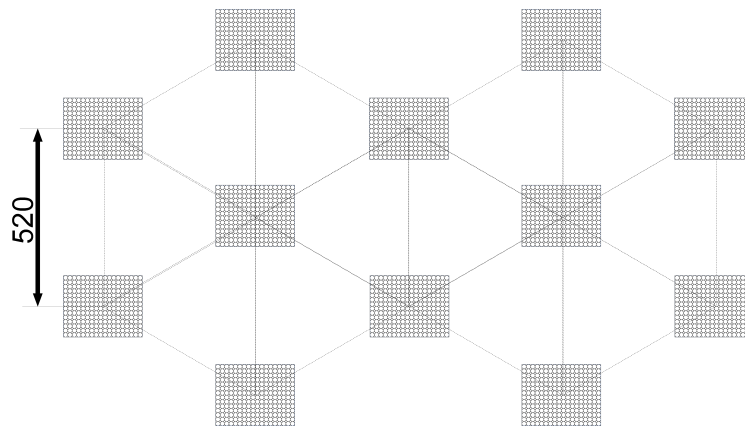


Fig. 4.11. Dimensions of ceiling-sided AUPA devices in the experiment.

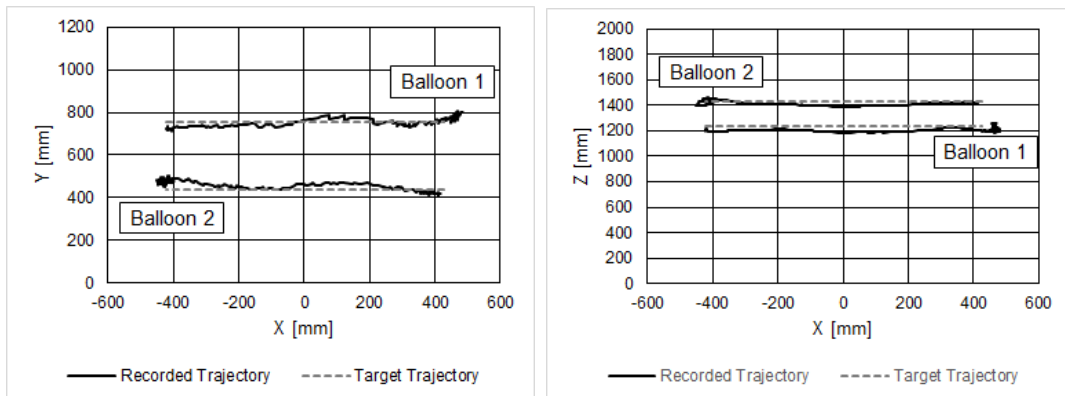


Fig. 4.12. Recorded trajectory of balloons manipulated by single-sided AUPA devices.

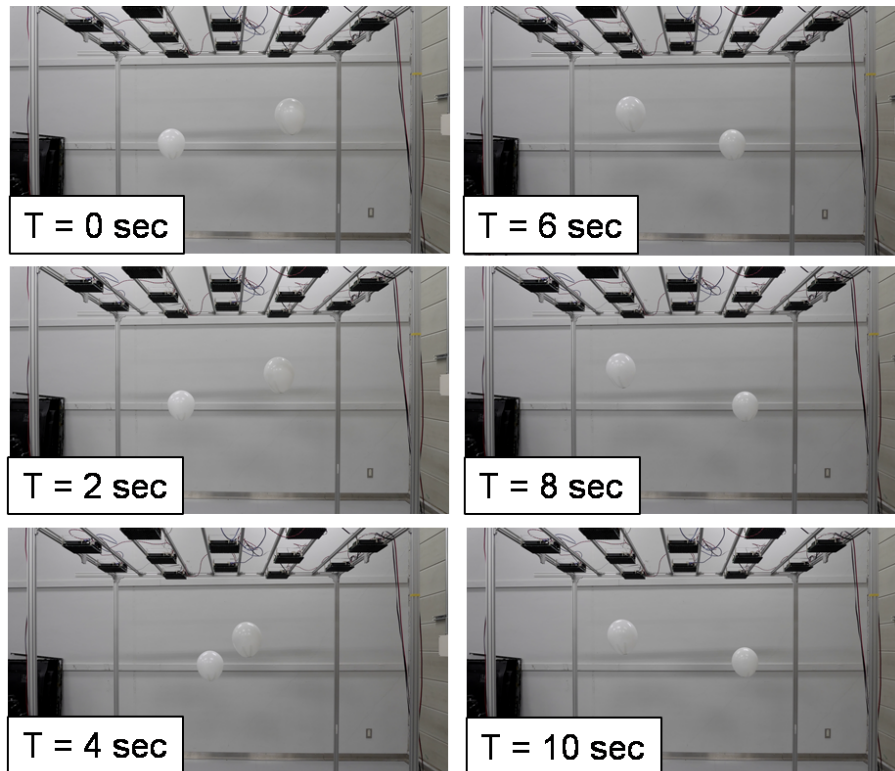


Fig. 4.13. Manipulation of two balloons.

Chapter 5

Floating Balloon Display for Body-scale Augmented Reality

In this chapter, the author presents a floating display system for device-free augmented reality (AR) of full-body scale (Fig. 5.1). The system projects an image to helium-filled balloon screens that is controlled by the dynamic manipulation system. The power supply for actuation and display from the environment provides long operational time, which is limited only by the helium loss. For this feature, it is effective for presenting static objects that should float continuously in the air such as menus, icons, and public art. This chapter describes the implementation and evaluation of the floating display system.

5.1 Background and Motivation

Augmented reality (AR), which superimposes digital information on the real world [62] has been acknowledged as a promising technology. The expected applications include manufacturing [63], medical care [64], education [65], and entertainment [66].

The display methods can be classified into two types: non-device-free AR and device-free AR. Displays of the former type include see-through head-mounted-display and tablet devices. Recently, the author sees prevailing of non-device-

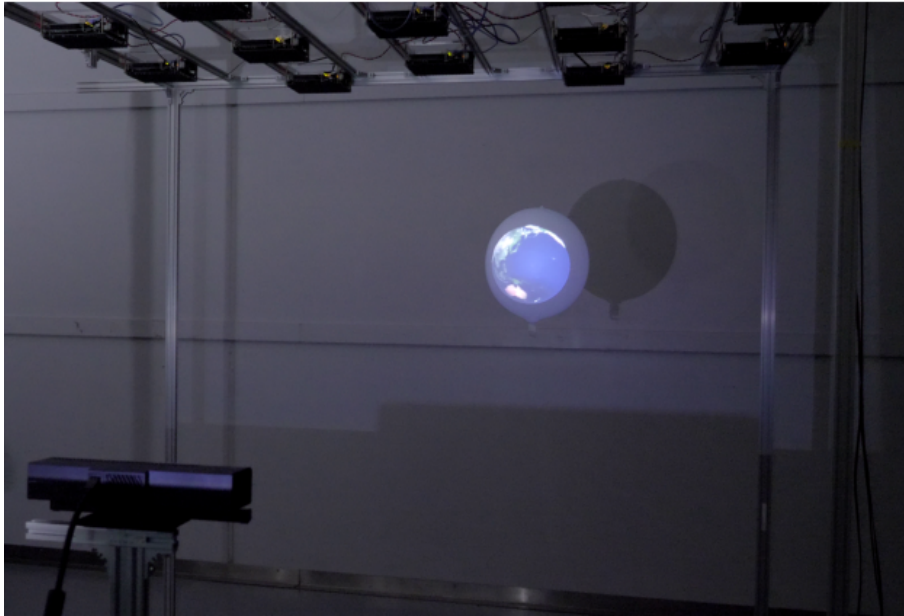


Fig. 5.1. Balloon display system for body-scale augmented reality.

free AR in our daily life. AR Application softwares such as games for tablet devices has become widespread. HMD such as Microsoft HoloLens [67] have been commercialized. One of the technical challenges of AR is to make wearable visual displays such as AR glasses and head-mounted displays more light-weight and power-saving to reduce the stress of wearing and the operational time.

Device-free AR displays digital contents to the users who have no display devices. The advantages of device-free AR includes no stress of wearing devices, the sharability of contents. The typical example is spatial AR (SAR), or projection-mapping-based AR. Its applications include theme park attractions [66], workbench [68], and collaborative digital workspace [69].

First series of SAR was exclusively designed to project a planar image onto an existing plane. Following them, several researches proposed display and interaction system for digital objects at an arbitrary position in 3D space. For example, a 3D workbench has made it possible to collaborate up to two people using 3D shutter glasses [70]. Another examples include methods to project an image onto floating objects in the air such as fog [71, 72], water drops [73, 74], and bubbles [75]. ZeroN created a 3D interaction in a range of several centimeters in height

by projecting an image onto a magnetically suspended magnet [43]. Pixie dust [76], LeviPath [77] realized a voxel display using acoustically suspended particles. Freeman used levitated particles to enhance physical objects [78]. Acoustically levitated particles can be combined for displaying chart [79], or pointers [80, 81]. Leviprop levitated a sheet for projection in the air [82]. Hirayama et al developed a volumetric image by a scanning illuminated particle [83]. In recent years, many AR applications using quadcopter have been proposed [8, 7, 9, 84]. The merit will still be able to achieve human-scale interactions. For example, LightBee has increased the presence of avatar using the ability to move at the height of a person [85]. Another platform to display an image in the air is a blimp [86, 87].

Although dynamic contents can be presented by active-type displays, it remains to be difficult to present passive contents in the air, which steadily floats, within a full-body immersive AR environment because it requires a long flight time. The examples of passive contents include menus, icons, public art. Such objects should stay calm in the air until the user intentionally interferes to avoid distracting the user and to be noticed instantly when needed. Displays that have such properties are called ambient displays or calm technologies. The previous research suggests that such calmness is important to reduce mental workload [88]. It should be noted that being calm does not necessarily mean that the movement has to be stopped. For example, the bar indicating the communication strength must always change the mark according to the communication strength.

We propose a floating display to express such ambient contents. The video is presented in the air by projecting the video onto a floating balloon using the proposed method. Because all the power is supplied from the environment, the proposed system achieves long operational time of one day or more, which depends only on helium loss from the balloon screens.

Note the difference from the conventional acoustic based display [76, 77]. Both are the same in that an image is projected onto an object suspended by acoustic radiation force, Its purpose and implementation method are different. The traditional acoustic based display was a voxel display, which levitated particles as voxels. On the other hand, what we are trying to realize is a spherical display

that aims to project a high-resolution image onto a surface with an area, and as a representation method, [89, 90, 91]. The method proposed in this paper was used to levitate an object with sufficient area to project an image. It may be used as a tangible interface. Mid-air tangible objects with one-dimensional movements were formerly developed using aerodynamic levitation. [47, 46]. We believe that the proposed system provides a platform to explore tangible interaction in 3D space.

5.2 System Overview

The block diagram of this system is shown in Fig. 5.2. This system consists of a projector-camera system and the dynamic manipulation system that is described in chapter 3 and chapter 4. In this system, The system projects images onto helium-filled balloons that are controlled by AUPA devices. The system also tracks the user to detect his/her interaction with the balloon screen. Images are rendered based on the geometric relationship among the projectors, screens, and the user.

The prototype uses a Microsoft Kinect V2 sensor to track the screen in real time. Although the Kinect V2 has both a color and a depth camera, we used only the depth camera because it is not affected by the change in the illumination by the projector. The author uses a commodity projector BenQ TK 800.

5.3 Tracking System

5.3.1 Estimating Screen Position

The prototype determines the screen position using the following procedure. First, it subtracts the background from the depth image. Next, it performs binarization based on whether each pixel is inside the workspace. Then, it captures the depth of the center of the binarized image in order to estimate the 3D position of the frontmost point of the screen. Finally, it estimates the center of the screen by extrapolating the frontmost depth by its radius. This simple binarization-based

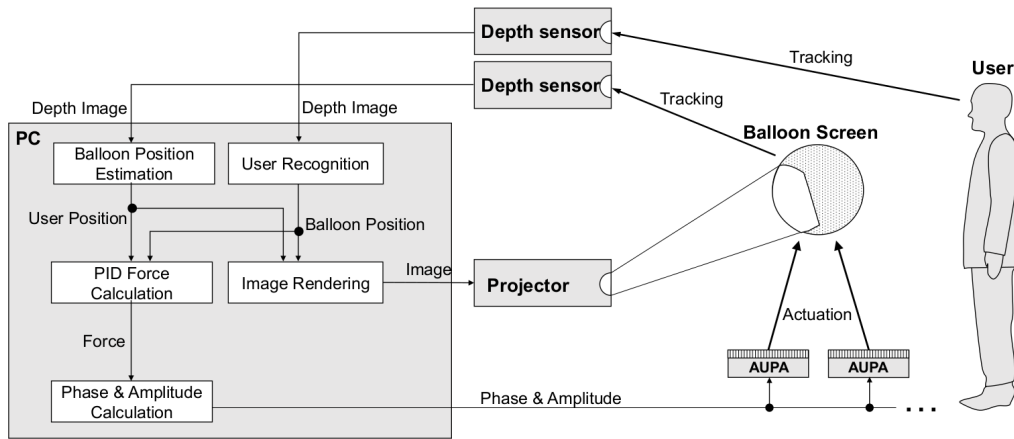


Fig. 5.2. Schematic diagram of floating display system

tracking technique works only if nothing is in contact with the screen. However, the user touches the screen, the mass center shifts. To reduce the shift, it applies an adaptive circular window (Fig. 5.3). As the window, we use the projection of the virtual circle of a predefined radius at the screen position to the depth image plane (Fig. 5.3). The radius of the circular window is adaptively changed in proportion to the distance between the screen and the depth camera. This prevents tracking failure caused by the user’s touch to the screen (Fig. 5.5)

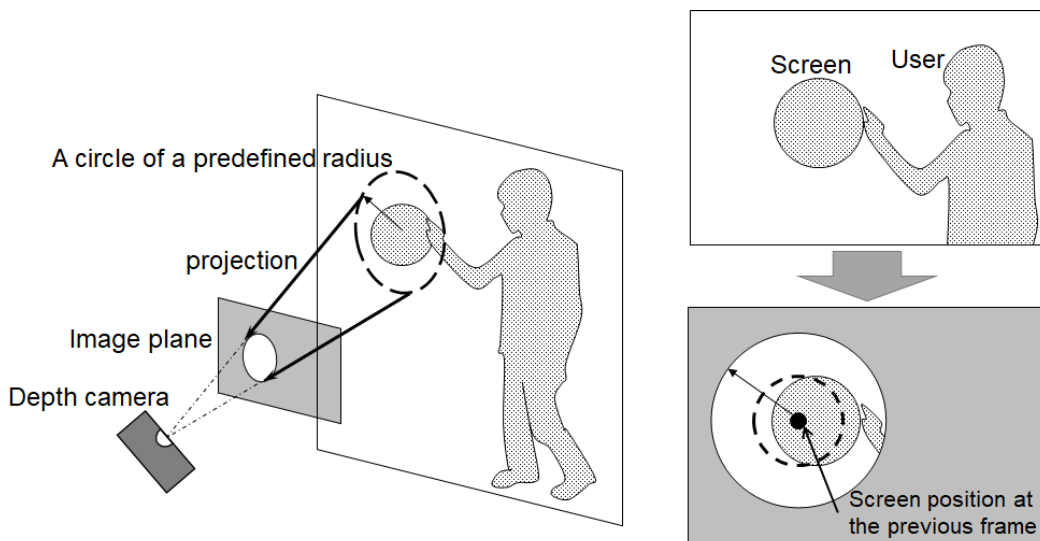


Fig. 5.3. Schematic illustration of adaptive circular window. (Left): Calculation of adaptive circular window in a scenario wherein a user touches a floating screen. (Right) Application of window to depth camera view.

5.3.2 Registration between AUPA Devices and Depth Camera

Registration between the AUPAs and the Kinect depth camera is required to place the display at the specified position in the space. Especially in large spaces, an accurate and flexible method is required. This chapter describes the registration method of AUPA and Kinect V2.

We used color markers, a color camera, and a depth camera on Kinect V2 placed at known positions in space. Here, it is assumed that the arrangement of AUPA and the positional relationship between the color camera and the depth camera are already known. First, color markers are placed at known locations. Acquire a color image with a color camera and a point cloud with a depth camera. From the geometric relationship between the color camera and depth camera, calculate the position of the point cloud captured by the depth camera on the color camera image, and obtain the correspondence between each pixel of the color camera and the point cloud. Kinect V2 has a function that maps each pixel of the depth camera to a pixel on the color map (note that the reverse is not possible). Next, extract the marker from the Color image. The position of the marker in the depth camera coordinate system is obtained from the correspondence between each pixel of the color image obtained earlier and the point cloud. Note that the point cloud is not necessarily associated with all color pixels. For example, if you can see from the color camera by occlusion but not from the depth camera, you cannot get the 3D position corresponding to the color pixel. If the marker position cannot be obtained correctly, the point is discarded.

Once the position of the color markers in the Kinect depth camera coordinate system is obtained in this way, the position and orientation of the depth camera relative to the AUPA can be determined by associating the positions of the color markers in the AUPA coordinate system with the positions in the depth camera coordinate system. This time, we use the singular value decomposition to find the least-squares solution of the position and orientation that correspond to the points obtained in the two coordinate systems [92].

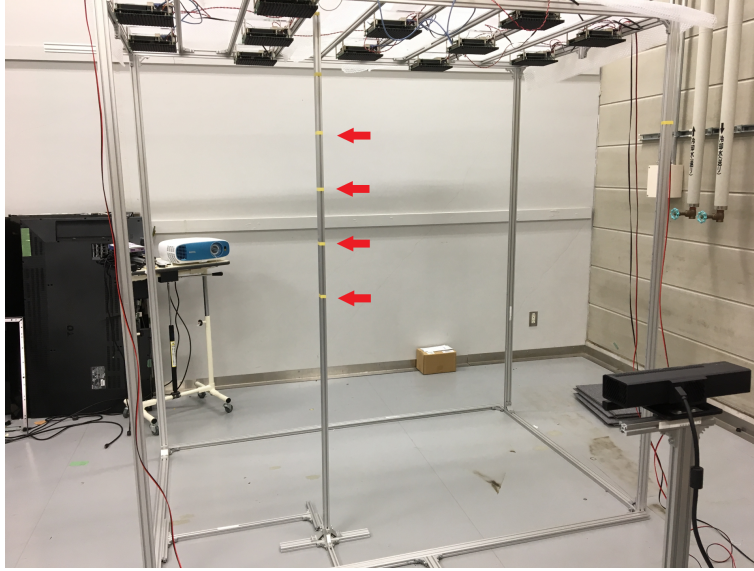


Fig. 5.4. Registration of AUPAs and Kinect V2. Arrows direct the color marker attached on an aluminum frame.

Let the positions of the markers in the AUPA coordinate system be $\mathbf{x}_1, \mathbf{x}_2, \dots, \mathbf{x}_N$, their positions in the depth camera coordinate system be $\mathbf{x}'_1, \mathbf{x}'_2, \dots, \mathbf{x}'_N$, the position and the attitude of the depth camera relative to the AUPA coordinate system be \mathbf{t}, \mathbf{R} , and the noise be $\mathbf{n}_1, \mathbf{n}_2, \dots, \mathbf{n}_N$. Then, the following equation holds:

$$\mathbf{x}_i = \mathbf{R}\mathbf{x}'_i + \mathbf{t} + \mathbf{n}_i. \quad (5.1)$$

Now, we want the position and the posture of the depth camera that minimizes the following quantity

$$\Sigma^2 = \left| \sum_{i=1}^N \mathbf{x}_i - (\mathbf{R}\mathbf{x}'_i + \mathbf{t}) \right|^2. \quad (5.2)$$

Let the least square solution of the position and the attitude be $\hat{\mathbf{t}}, \hat{\mathbf{R}}$. These solutions map the centroid of the positions in the depth-camera coordinate system \mathbf{c}' to the centroid of the positions in the AUPA coordinate system \mathbf{c} [93].

$$\mathbf{c} = \frac{1}{N} \sum_{i=1}^N \mathbf{x}_i, \quad \mathbf{c}' = \frac{1}{N} \sum_{i=1}^N \mathbf{x}'_i \quad (5.3)$$

$$\mathbf{c} = \hat{\mathbf{R}}\mathbf{c}' + \hat{\mathbf{t}}. \quad (5.4)$$

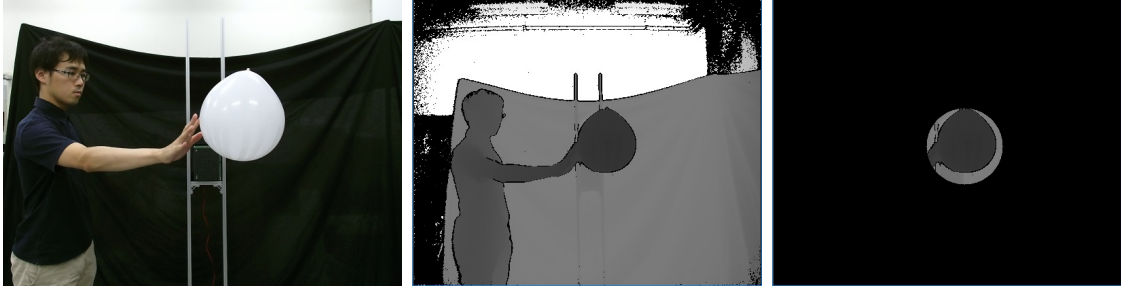


Fig. 5.5. Adaptive circular window applied to depth map. (Left) A View from the color camera. (Center) Raw depth image from depth camera. (Right) depth image with an adaptive circular window applied.

Let:

$$\Delta \mathbf{x}_i = \mathbf{x}_i - \mathbf{c} \quad \Delta \mathbf{x}'_i = \mathbf{x}'_i - \mathbf{c}'. \quad (5.5)$$

Then, the function to minimize is written as follows:

$$\Sigma^2 = \sum_{i=1}^N |\Delta \mathbf{x}_i - \mathbf{R} \Delta \mathbf{x}'_i|^2. \quad (5.6)$$

Now, I define 3x3 matrix \mathbf{H} as following:

$$\mathbf{H} = \sum_{i=1}^N (\Delta \mathbf{x}_i)(\Delta \mathbf{x}'_i)^T. \quad (5.7)$$

Perform singular value decomposition on this matrix.

$$\mathbf{H} = \mathbf{U} \mathbf{\Lambda} \mathbf{V}^T \quad (5.8)$$

if $\det(\mathbf{V} \mathbf{U}^T) = +1$, then

$$\hat{\mathbf{R}} = \mathbf{V} \mathbf{U}^T. \quad (5.9)$$

Now, the attitude of the depth camera is obtained. Finally, the position can be obtained from Eq. (5.4) as follows:

$$\hat{\mathbf{t}} = \mathbf{c} - \hat{\mathbf{R}} \mathbf{c}'. \quad (5.10)$$

5.4 Natural User Input System

A natural user input system is implemented to allow the users to manipulate the screen position intuitively by dragging and dropping the screen directly with their hands. The prototype determines whether the screen has been “grabbed” based on the distance between the screen and a user’s hand. To determine the position of the user’s hand, we used a body tracking function provided in Kinect V2 Software Development Kit. If the distance is below a predefined threshold for a predefined duration, the prototype regards the screen as having been grabbed. In this state, the target position of the screen is updated using the current position at every frame. Updating the target position makes the projected image move along with the screen at this state because of the projection strategy described in Section 3.2. When the distance again becomes greater than the threshold distance, the prototype regards the screen as having been released and stops updating the target position. Consequently, the target position is set to the position at which the screen is released.

5.5 Projection System

5.5.1 Registration between Projectors and Depth Cameras

We estimated the internal and external parameters of the projector by the following procedure. First, the projector projects a 9×9 circle grid pattern on a whiteboard. Next, the Kinect v2 detects the pattern using its color camera and captures their 3D position using its depth camera. Third, the inclination of the whiteboard is estimated and their 2D positions on the white board were determined. We repeated this procedure for whiteboards of various directions and positions. Finally, it retrieves the extrinsic parameters and the intrinsic parameters using CalibrateCamera function of OpenCV [94] library, which is based on [95, 96] using the collected pairs of positions on the whiteboard and that on the original image of the projected points.

5.5.2 Projecting Virtual Contents to Real World

To project the virtual world to the real world via a projector, Copy the view of the created virtual world from the camera object using the projector. For this purpose, the position, orientation, and internal parameters of the actual projector must be correctly reflected in the camera object placed in the virtual world. This section describes the method.

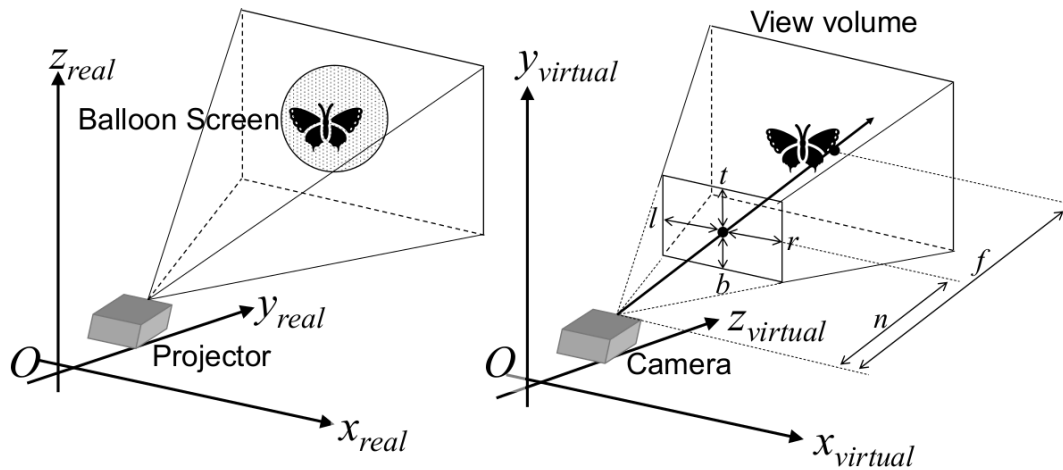


Fig. 5.6. Projection of a scene viewed by a camera object in virtual world.

Matching Views of Real Projector and Virtual Camera

Now, the internal parameters of the projector are calculated in the form of camera matrix $C_{\text{projector}}$ by the method described in Section 5.5.1.

$$C_{\text{projector}} = \begin{bmatrix} f_x & 0 & c_x \\ 0 & f_y & c_y \\ 0 & 0 & 1 \end{bmatrix} \quad (5.11)$$

where:

- f_x, f_y : focal lengths of the projector.
- (c_x, c_y) : principal point. Note that the principal point of a typical projector is off the center of the image.

We consider projecting an image captured by a camera in the virtual world (virtual camera object). The view of the virtual camera object is given by projection matrix $\mathbf{M}_{\text{projection}}$ in a general graphic pipeline in order to accelerate rendering processes. The projection matrix is expressed in terms of the coordinates of each vertex in the camera coordinate system of the view volume (frustum) as follows:

$$\mathbf{M}_{\text{projection}} = \begin{bmatrix} \frac{2*n}{r-l} & 0 & \frac{r+l}{r-l} & 0 \\ 0 & \frac{2n}{t-b} & \frac{t+b}{t-b} & 0 \\ 0 & 0 & -\frac{f+n}{f-n} & -\frac{2fn}{f-n} \\ 0 & 0 & -1 & 0 \end{bmatrix} \quad (5.12)$$

where:

- r, l, t, b : right, left, top, and bottom boundary values of the front clipping plane
- n : the distance between the camera and the front clipping plane
- f : the distance between the camera and the back clipping plane.

The following geometric relationship holds between the camera matrix parameters and the dimensions of the frustum of the virtual camera object:

$$r = (w - c_x) \frac{n}{f_x} \quad (5.13)$$

$$l = (-c_x) \frac{n}{f_x} \quad (5.14)$$

$$t = c_y \frac{n}{f_y} \quad (5.15)$$

$$b = (c_y - h) \frac{n}{f_y} \quad (5.16)$$

where:

- w, h : the resolutions of the projector image in width and height.

Substituting these to (5.12) yields the following representation of the projection matrix of the virtual camera in terms of parameters of the projector in the real

world

$$\mathbf{M}_{\text{projection}} = \begin{bmatrix} \frac{f_x}{w} & 0 & \frac{w-2c_x}{w} & 0 \\ 0 & \frac{f_y}{h} & \frac{2c_y-h}{h} & 0 \\ 0 & 0 & -\frac{f+n}{f-n} & -\frac{2fn}{f-n} \\ 0 & 0 & -1 & 0. \end{bmatrix} \quad (5.17)$$

Here, the internal parameters of the projector is configured in accordance with the virtual camera object.

Position and Attitude of Virtual Camera Object

Next, we describe how to make the camera object in the virtual world correspond to the position and orientation of the projector in the real world.

In this section, the position and orientation are represented by a homogeneous transformation matrix. If the rotation matrix representing the posture is set as \mathbf{R} and the vector representing the position as \mathbf{t} , the homogeneous transformation matrix \mathbf{T} is expressed as follows

$$\mathbf{T} = \begin{bmatrix} \mathbf{R} & \mathbf{t} \\ \mathbf{O} & 1 \end{bmatrix}. \quad (5.18)$$

The homogeneous coordinates \mathbf{x} corresponding to the position \mathbf{r} are expressed as follows:.

$$\mathbf{x} = \begin{bmatrix} \mathbf{r} \\ 1 \end{bmatrix}. \quad (5.19)$$

Let a homogeneous transformation matrix that maps a homogeneous coordinate \mathbf{x}_A expressed in a coordinate system A to a coordinate system B representation be $\mathbf{T}_{A \rightarrow B}$. Then,

$$\mathbf{x}_B = \mathbf{T}_{A \rightarrow B} \mathbf{x}_A. \quad (5.20)$$

The list of homogeneous transformation matrices that have been found in previous sections.

- $\mathbf{x}_{\text{aupA}}^{(\text{real})}$: AUPA coordinate system in the real world.
- $\mathbf{x}_{\text{kinect}}^{(\text{real})}$: Depth camera coordinate system in the real world.
- $\mathbf{x}_{\text{projector}}^{(\text{real})}$: Projector coordinate system in the real world.

- $\mathbf{x}_{\text{base}}^{(\text{virtual})}$: Base coordinate system of the virtual world.
- $\mathbf{x}_{\text{camera}}^{(\text{virtual})}$: Camera coordinate system in the virtual world.

In general, coordinate systems in the real space are defined in the right-handed coordinate system following the conventions of the mechanical system, while the coordinate systems in the virtual space are defined in the left-handed coordinate system following the conventions of graphics. The author indicates which is used by (real), (virtual) superscripts.

The current interest is to determine the position and orientation of the camera object in the virtual world, that is $\mathbf{T}_{\text{camera} \rightarrow \text{base}} = [\mathbf{R}_{\text{camera}} | \mathbf{t}_{\text{camera}}]$. The homogeneous transformation matrices that have been found up to the previous chapter are the following two.

- $\mathbf{T}_{\text{kinect} \rightarrow \text{aupa}}$: the transform relating the pose and position of Kinect depth camera (Section 5.3.2)
- $\mathbf{T}_{\text{projector} \rightarrow \text{kinect}}$: the transform relating the pose and position of projector (Section 5.5.1)

In addition to the above, the following information is required to determine the position of the camera.

- $\mathbf{T}_{\text{aupa} \rightarrow \text{base}}$: The transform relating to the conventions of the AUPA coordinate and the base coordinate of the virtual world, which is usually defined by the user. This transform may include reflection.
- $\mathbf{T}_{\text{camera} \rightarrow \text{projector}}$: the transform relating the conventions of the camera coordinate and the projector coordinate. This transform may include reflection.

Using these homogeneous transformation matrices, the position and orientation of the camera object are expressed as follows.

$$\mathbf{T}_{\text{camera} \rightarrow \text{base}} = \mathbf{T}_{\text{aupa} \rightarrow \text{base}} \mathbf{T}_{\text{kinect} \rightarrow \text{aupa}} \mathbf{T}_{\text{projector} \rightarrow \text{kinect}} \mathbf{T}_{\text{camera} \rightarrow \text{projector}}. \quad (5.21)$$

Note that the rotation matrix contained in $\mathbf{T}_{\text{camera} \rightarrow \text{base}}$ is a virtual coordinate system (which is typically left-handed). To express the same rotation in the right-

handed coordinate system, when the mirror image transformation about the yz plane is set to \mathbf{T} ,

$$\mathbf{R}^{\text{a(right)}} = \mathbf{T}\mathbf{R}^{\text{(left)}}\mathbf{T} \quad (5.22)$$

Process. In particular, if you want to obtain the quaternion notation in the left-handed coordinate system, find the $\mathbf{R}^{\text{(real)}}$ once using the above equation, then find $\mathbf{q}^{\text{(real)}}$, Sometimes it is convenient to obtain $\mathbf{q}^{\text{(virtual)}}$ by multiplying the x and w components of $\mathbf{q}^{\text{(real)}}$ by -1 .

5.6 Stereoscopic Image Rendering

This section presents a method of presenting a stereoscopic image.

5.6.1 Perspective-correct Image Rendering

In order to achieve stereoscopic viewing, it is necessary to present a perspective-correct image to the viewer (Fig. 5.7).

Here we assume that the shape of the screen is perfect sphere. The system creates a mesh-discretized sphere object in the virtual space and places it in the virtual space at a position corresponding to the balloon display in the real space. In addition, a camera object to capture a scene to be shown to the user is placed in the virtual space. Then, Project each mesh of the sphere object onto the user's view and calculate which coordinate of the user's view corresponds to (Fig.5.8). The user's view pattern corresponding to mesh is mapped to the mesh by an affine transformation. The affine transform is an approximate transform, but if the mesh is fine enough, you can draw an image without any sense of incongruity. Performing this operation for all meshes yields a semi-perspective-correct image.

5.6.2 Stereoscopic Image

In this system, stereoscopic images are presented using active shutter glasses. Images for the right and left eye are displayed at 120 Hz. 3D shutter glass synchronizes with it to close the right and left eye shutters so that separate images

are input to the right and left eyes which yields a stereoscopic image (Fig. 5.9).

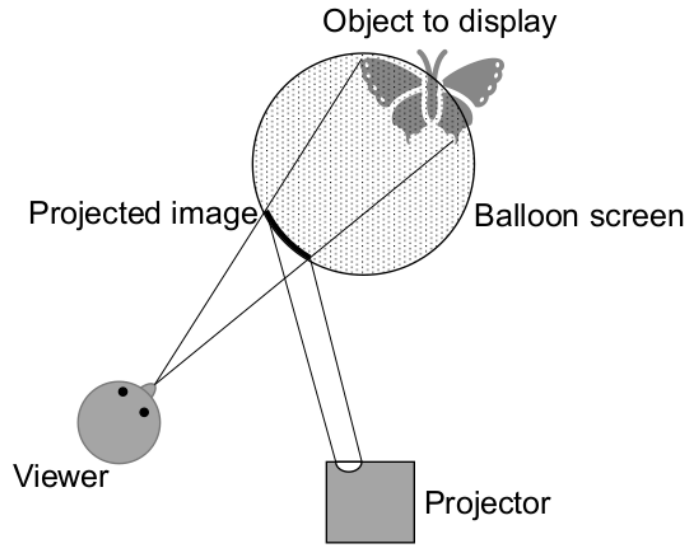


Fig. 5.7. Schematic illustration of perspective-correct projection

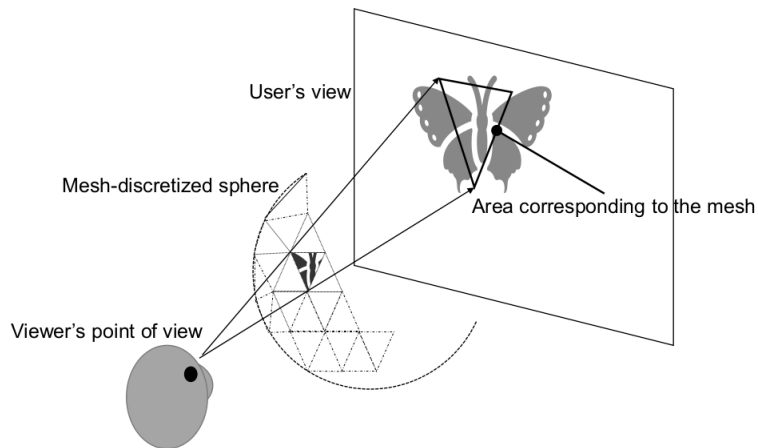


Fig. 5.8. Projection to mesh-discretized sphere.

5.6.3 Projection Point

We have two options for image projection approaches. One is a projection onto the current position of the screen. The other is a projection onto the target position of the screen. In the case of the former approach, a position instability



Fig. 5.9. Stereoscopic image of a Utah teapot.

results in a fluctuation in the image position. In the case of the latter approach, the screen position fluctuation with respect to the projected image distorts the image. In this paper, the latter approach when the screen is not moving because we empirically found that the latter effect is less significant. A detailed evaluation of this effect is presented in Section 5.7.

5.7 Preliminary Experiment on Visibility

Although the closed loop controller described in Chapter 3 stabilizes the screen position, its fluctuation cannot be eliminated in reality. This causes distortions and movement of the projected image, which may degrade its visibility. This effect seems to be greater when the image is viewed from an oblique direction than when the image is viewed from the front because the movement of the screen leads to not only distortions and scaling but also a translation of the image in the view from an oblique direction.

We conducted a user study to evaluate the effect of the instability in screen position on the accuracy of the user's image recognition of the image. In this study, we measured the minimum size of the recognizable pattern. We used a Landolt ring as a target. We projected the target onto the screen and measured an identifiable target threshold size. We then compared the threshold sizes of the

floating and fixed images.

5.7.1 Procedure

The configuration used in this study is shown in Fig. 5.10. In the fixed-screen condition, the screen is fixed on a tripod. In the floating-screen condition, the target position of the screen is set to the position at which it is fixed in the fixed-screen condition. In both conditions, the same balloon screen was used. To obtain the required resolution for displaying Landolt rings, the projector was placed sufficiently closer to the screen. The distance between the screen and the subject was two meters. When viewing the image from the front, the subject stood behind the projector, and when viewing the image from an oblique direction, the subject stood at an angle of 20 degrees. The gap of the Landolt rings ranged from 0.5 to 2.0 arcmin. The target gaps were oriented in horizontal or vertical directions. Subjects were instructed to make a guess in case they were not sure about the answer. Landolt rings were presented in descending order until the subject answered incorrectly. For each trial, we recorded the minimum size of the Landolt ring that the subject answered correctly. We repeated the procedure three times per subject. We used the average of the three measurements as the subject's threshold target size. The image presentation time was limited to two seconds in order to prevent a subject from waiting for a Landolt ring to appear larger as the screen approached them. Prior to the experiment, subjects practiced the task expected of them until they understood the task. Subjects observed the target with binocular vision.

After the experiment, the subjects were asked to answer the following questions in four grades (0 - 3).

Q 1) Did the fluctuation and distortion of the image interfere with your image recognition?

Q 2) Did the fluctuation of the screen position interfere with your image recognition?

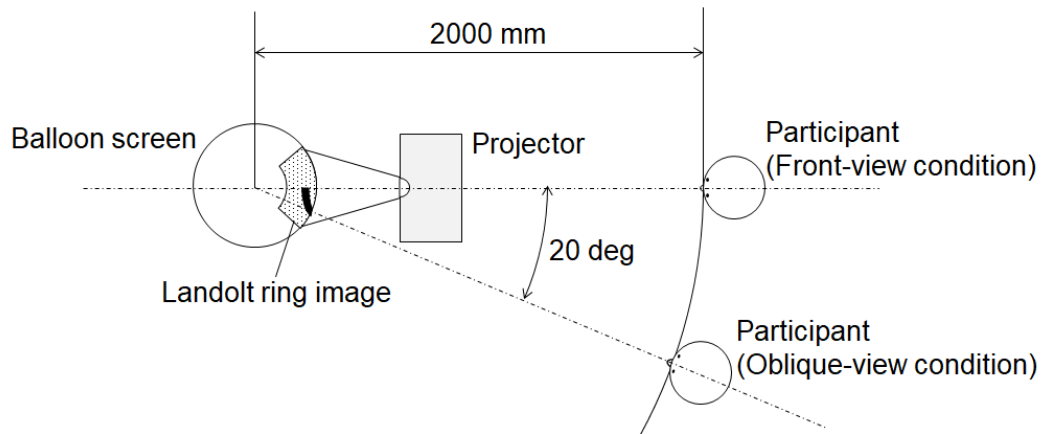


Fig. 5.10. Schematic illustration of experiment configuration.

Q 3) Did you feel frequently dazzled?

Q 4) Did you feel more stress when you saw the screen floating?

Five male university students participated as subjects. Their ages ranged from 22 to 25 years.

In this experiment, AUPA devices are arranged in the same manner as in the experiment described in Section 3.3.1.

5.7.2 Result

The threshold target sizes of each participant in the case of the front-view and oblique-view conditions are shown in Fig. 5.11. Figure 5.12 shows their answers to the questionnaire. Regardless of the view point, no decrease in target threshold size was observed. (The difference of threshold target size ranged from -0.05 to 0.366 in the case of the front-view condition, and from -0.0667 to 0.233 in the case of the oblique-view condition.) This result is consistent with the subjective evaluation that the negative effect of the screen motion was small (Q1: Negative Effect of image distortion, average score:1, standard deviation: 0.8, Q2: Negative effect of screen movement, average score: 0.8, standard deviation:0.837). Many subjects expressed the impression that the image sometimes dazzled them and became invisible. This suggests that the distance of the projector from the balloon and the amount of light should be carefully adjusted for stress-free image

presentation.

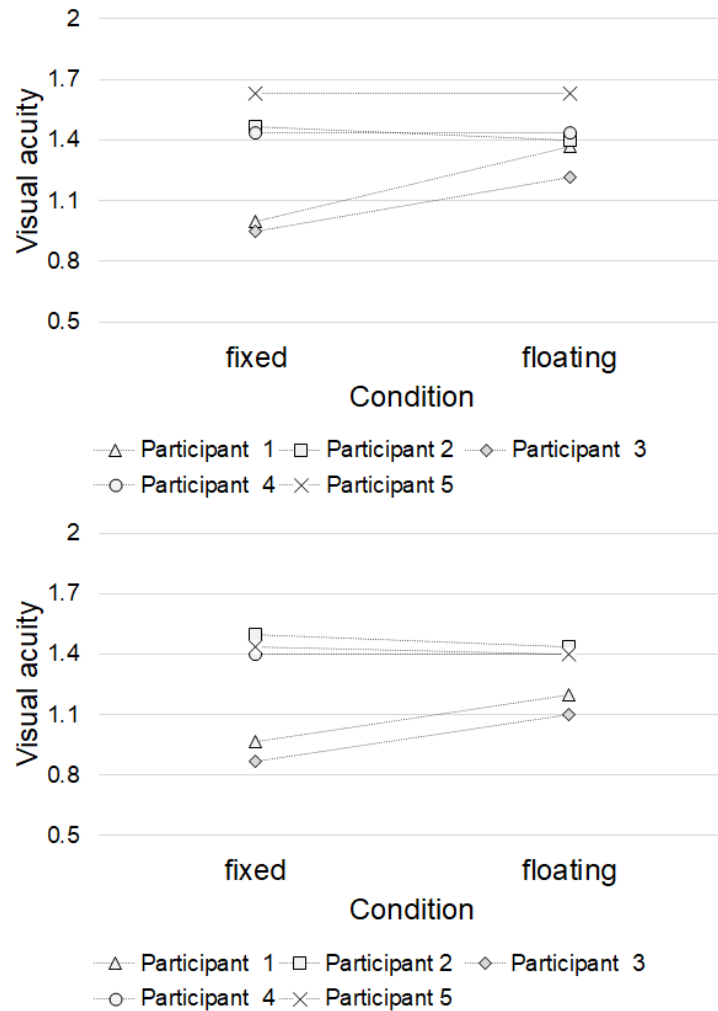


Fig. 5.11. Threshold target sizes of front-view condition (Right) and oblique-view condition (Left).

5.8 Demo at Siggraph Asia 2019

The demonstration of the floating display system was performed in Siggraph Asia 2019 held in Australia. Figure 5.13 shows the demo system. The AUPA devices are arranged on the ceiling in the same manner as in Section 4.3. This configuration allows participants to see and touch the display from any directions. The balloons of 25.4 cm (10inch) radius were used as screens. The demonstration continued for three days (Fig. 5.14). [htbp]

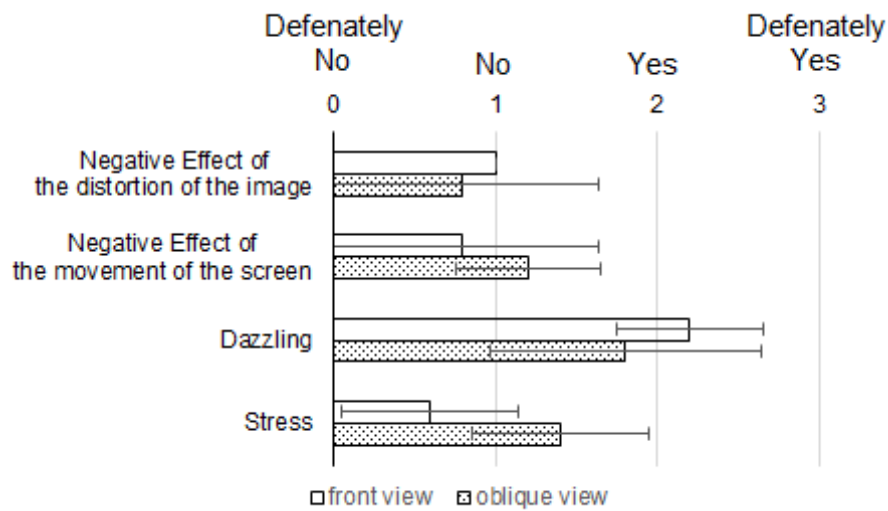


Fig. 5.12. Mean ratings and unbiased standard deviations for negative effects of floating screen.

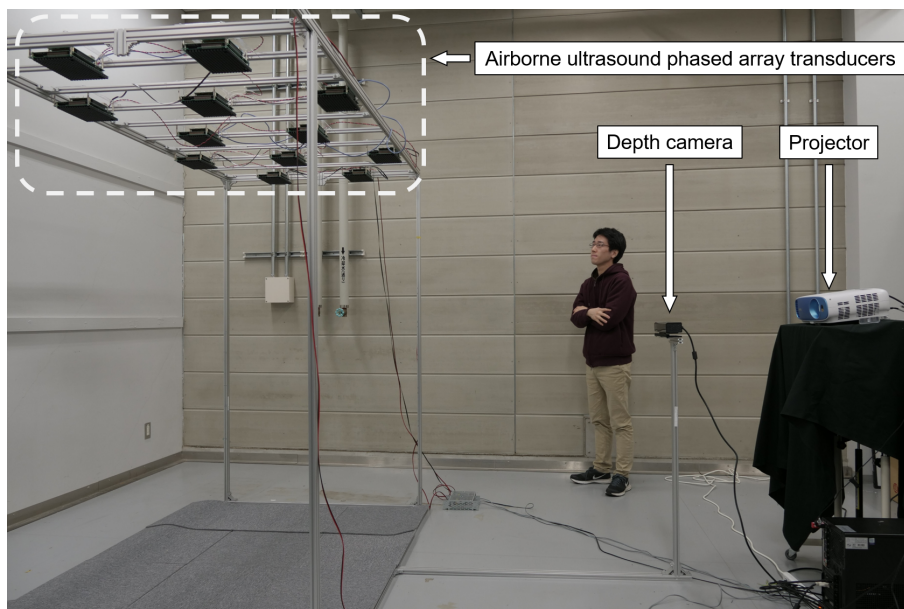


Fig. 5.13. Floating display system with ceiling-sided AUPA devices.

5.9 Application Scenarios

5.9.1 Personal Display for Workers

As is shown in Fig. 5.15, multiple balloons can be used for multiple people. Users can use it as if they were wearing an eyeglass-type display individually, although

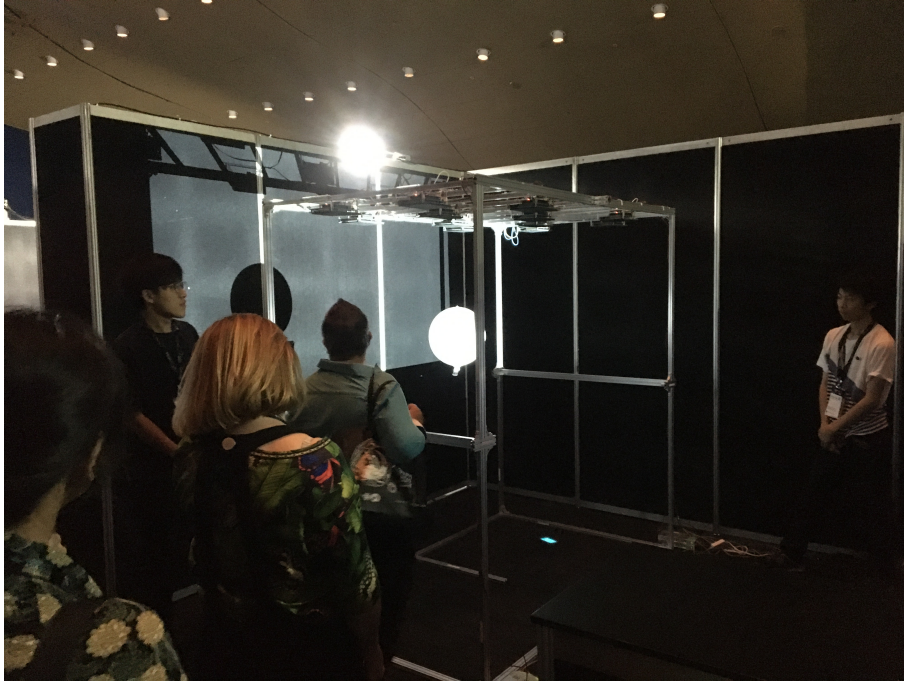


Fig. 5.14. Demonstration at Siggraph Asia 2019.

it does not superimpose the image over real objects. It does not narrow the workspace as the display is floating in the air.

5.9.2 Guidance

The proposed system can be used for guiding people (Fig. 5.16). Users only need to follow the balloon moving toward the destination. Since the balloon is floating, the condition on the ground does not affect the motion of the balloon. Even if the user loses sight of the balloon, the system can make the user aware by moving in front of them or by actively tapping them. Projected images can be used for showing the supportive information such as the distance to the destination.

5.9.3 Avatar for Telecommunication

Figure 5.17 shows the telecommunication system using the prototype. The floating display can be used as an avatar for the remote people. Since the size of the balloon is comparable to that of a human head, and the height can be controlled so that it comes to the eye-contactable height, this screen is suitable for use as an avatar.

It can move freely in the room.

5.10 Discussion

We developed a passive-type midair display that is capable of presenting a floating image in a one-meter-cubic workspace. We have also shown that users can recognize an image on the floating screen as accurately as that on a fixed screen. However, the current system has some limitations.

The first limitation is that the workspace is still confined to a space that is defined by an arrangement of AUPA devices, although that is larger than that of previously proposed passive-type midair displays. We should note that occlusion of the screen from an AUPA device disables the AUPA and shrinks the workspace. Close interaction between users and the screen may cause such occlusion. A properly planned arrangement or redundant installation of AUPA devices may prevent this problem.

The second limitation is the small magnitude of the force that an AUPA device can apply. This leads to a vulnerability to ambient winds, which limits the applications of this system to indoor ones. In addition, the translation speed is much slower than drone-based midair displays for the same reason. The installation of a greater number of AUPA devices or the use of stronger transducers will solve this problem.

One concern of the system is the safety of the ultrasound. Though the ultrasound intensity into the body is much less than the safety standard determined for the medical imaging [97], the effect on the human auditory system is still under examination. The safety standard must be confirmed before the practical use, which is still under examination.

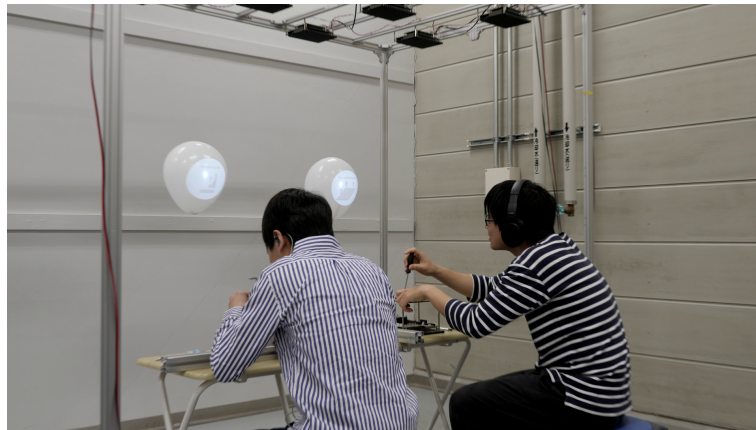


Fig. 5.15. Personal display for workers



Fig. 5.16. Person guided by an arrow displayed on a balloon display

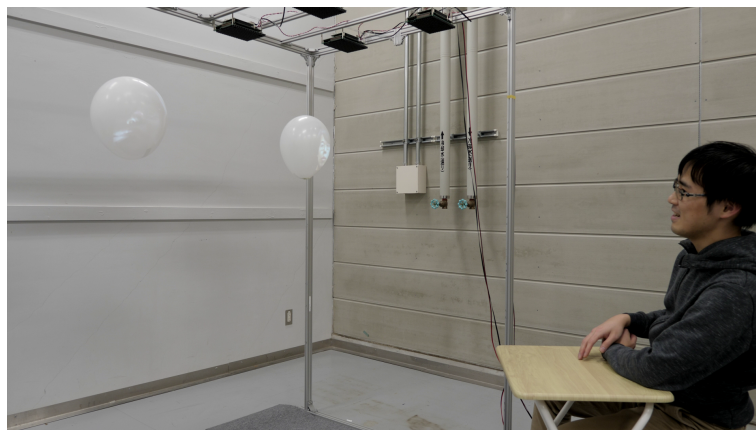


Fig. 5.17. Person talks with floating avatars.

Chapter 6

Encounter-type Haptic Feedback System Using an Acoustically Manipulated Floating Object

This Chapter presents another application system: an encounter-type haptic feedback system for virtual reality (VR). It utilizes a balloon that can move around in three dimensional space to provide haptic sensation at arbitrary three-dimensional positions. By locating a balloon at a position corresponding to that of a virtual object, the user equipped with a head-mounted display feels a contact sensation when his or her hand touches a virtual object. The balloon is remotely actuated by the dynamic acoustic manipulation system. We constructed a prototype system and performed a demonstration.

6.1 Background

A contact sensation is indispensable for virtual reality (VR) for its users to naturally interact with its contents. Many approaches have been proposed to achieve a natural contact sensation. Encounter-type haptic feedback [98, 99, 100] is one approach to present a natural contact sensation of an object in a virtual world or in a remote place. Encounter-type haptic devices present a contact sensation

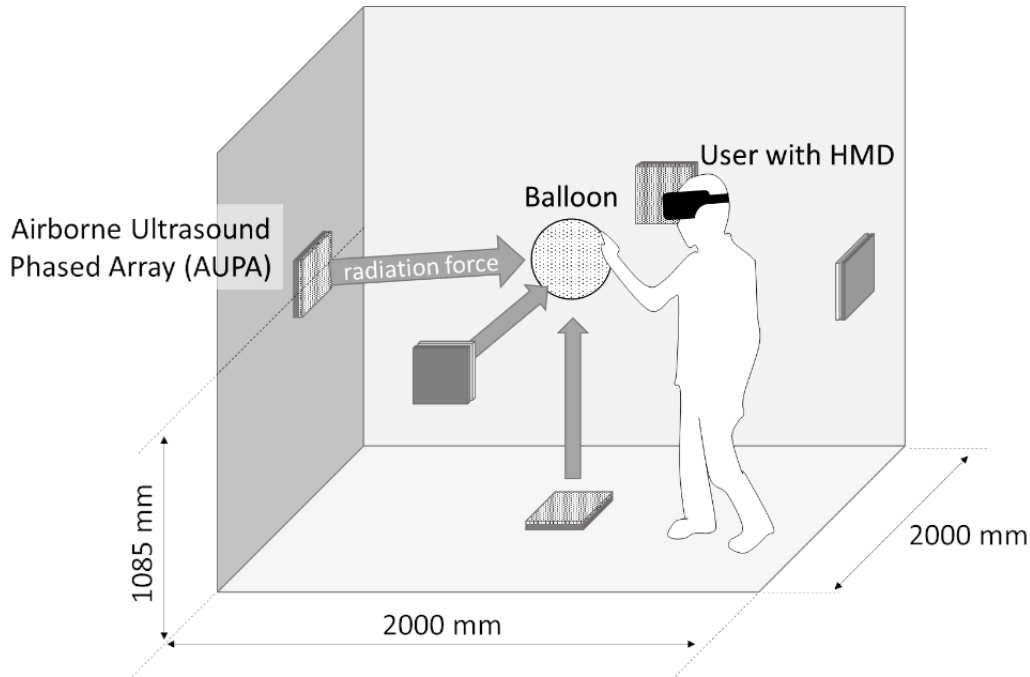


Fig. 6.1. Concept illustration of encounter-type haptic feedback system.

by controlling a real proxy object so that it touches the user only when he or she touches a virtual object. Conventionally, a proxy object is controlled by a robot arm [98, 99] or is implemented in an exoskeleton [100].

In this chapter, we propose a novel encounter-type haptic feedback system utilizing a balloon whose position is synchronized with the position of a virtual object (Fig. 6.2). The balloon is manipulated in three-dimensional space using airborne ultrasound. The system features no necessity to equip special haptic devices. This allows the user to move their hands freely. In comparison with midair haptic displays using ultrasound [13, 12, 15, 24] or air flow [101, 102], the proposed system requires smaller number of devices to be install to cover the full body.

6.2 System Configuration

The proposed system presents a contact sensation consistent when a user touches a virtual object. Figure 6.2) shows the system configuration. The proposed system consists of a VR system and the dynamic acoustic manipulation system described in Chapter 3. The virtual contents are generated by Unity game engine.

The virtual contents are displayed to the user through a head-mounted display (HMD). The target position of the proxy object is send from VR software running on Unity to the dynamic manipulation system after correct transformation from virtual space coordinates to real space coordinates. The mathematical detail of the transoformation can be found in Chapter 5. The positions of the hand and the head is tracked by a Leap Motion sensor and a HMD tracker. Using the tracking information, the relative positions of the virtual object and the avator's body is consistent with that of the proxy object and the user. Therefore, the avator's touch to the virtual object coincides the user's touch to the proxy object, whichi provides haptic sensation.

The demonstration was performed in Asia Haptics 2018. A balloon was used as a proxy object. In the demo, attentants punched a virtual monster floating in the air. Attendants expressed many kinds of impressions such as "interesting", "creepy", and "too light".

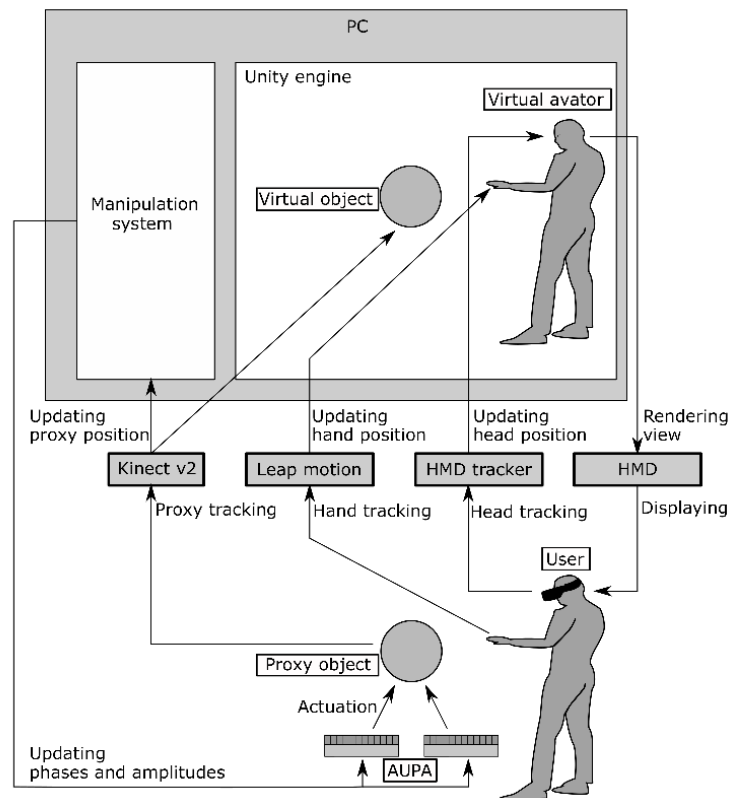


Fig. 6.2. System configuration of encounter-type haptic feedback system.

Chapter 7

Conclusion

7.1 Summary of Contributions

This thesis presents a dynamic acoustic manipulation method of macroscopic spheres within human-body scale workspace. The method stabilizes the objects using sensor-feedback control of an acoustic field. This thesis also presents two application systems: a floating display system and an encounter-type haptic-feedback system.

Chapter 2 presents models of acoustic radiation force on a macroscopic sphere located at various distances from the aperture of an AUPA. Especially, the effect of changes in the distance and the radius of the sphere in focusing beam is investigated via ray-acoustics. The comparison with the traditional wave-acoustics approach shows the validity of the application of a ray-acoustics approach to focusing beams of 40 kHz ultrasound to a sphere of 20 cm. Practical ARF models for focusing beams and plane-wave beams were also presented.

Chapter 3 presents algorithms to manipulate a macroscopic sphere using sparsely distributed AUPA devices. The AUPA devices emit axisymmetric ultrasound beams of appropriate powers such that the position of the sphere is stabilized in a PID manner. Such powers are derived by numerically solving a quadratic programming problem. The algorithm successfully manipulated a macroscopic object of 20 cm diameter at a height of more than one meter.

Chapter 4 discusses manipulation by single-sided AUPA devices to achieve lat-

eral scalability of the workspace. While naturally-descending objects can be suspended in a floor-sided configuration, naturally-descending objects can be suspended by a ceiling-sided configuration, which is useful for interface and surveillance applications. The triangular lattice arrangement allows users to enlarge the workspace by repeating the same pattern. This chapter also presents time-division multiplexing control of the beam directions for the manipulation of multiple objects. Simultaneous translation of two spheres to the adjacent cells by ceiling-sided devices was succeeded in an experiment. The result demonstrates the lateral scalability of the workspace.

Chapter 5 presents a floating display system as an application system. The system displays a planar or stereoscopic image at an arbitrary 3D position by image projection to a helium-filled balloon screen controlled by the dynamic acoustic manipulation system. The supply of the actuation power from the environment provides long operational time limited only by the helium loss. The system is effective for presenting static objects in the air in spatial augmented reality applications. The preliminary experiment suggested that the instability should not degrade the user's discrimination of projected patterns.

Chapter 6 presents an encounter-type haptic feedback system as another application system for virtual reality as another application system. The system synchronizes a floating object position with a corresponding virtual object which is rendered to the user through a head-mounted display. The coincidence of the touches to the floating object and the corresponding provides the user a touch sensation.

7.2 Future Works

This paper demonstrated the concept of dynamic acoustic manipulation of macroscopic objects and presented its application examples. The author sees room for further development. The author lists future works below:

7.2.1 Higher Speed Control

The fast movement is valuable in many application scenarios. In the avatar scenario, it allows the avatar to move as fast as humans. In the surveillance scenario, it allows the robot to go to the destination in a short time. In the guidance scenario, it enables the guidance of fast-walkers.

Fast movement may require evaluations on the effect of the delay. In this thesis, the dynamics is treated as a time-invariant linear system by assuming that the position and the ARF are determined without delay. However, if the movement becomes fast, the assumption fails. This requires modification to system modelling and the corresponding control algorithm.

Using high speed optical system will be effective. Hopping-pong system succeeded in changing the trajectory of ping-pong ball using high-speed stereo cameras and airborne ultrasound phased arrays [103]. For a faster balloon display, a system configuration similar to [104] may be effective.

Fast movement also requires the modification to the evaluation method of workspace. The evaluation method provided in this thesis assumes the quasi-static movements of objects. Therefore, there is no need to suppress momentum. On the other hand, the evaluation of the workspace of fast-moving objects requires not only the balance of forces but also the suppression of the momentum.

7.2.2 Six-degree-of-freedom Manipulation of Objects of Various Shapes

Rotational control in addition to translational control of objects of various shapes will enable a wide variety of applications. The technology is essential for versatile manipulation in microgravity environments. When it is used for control camera-equipped robot, it enables rotate itself and direct onboard camera toward its target. As a first step, Kasai et al and the author demonstrated rotational manipulation of a planar object in the air using single-sided AUPA devices [105].

7.2.3 Development and Evaluation of Application Systems

In this paper, a balloon display system is implemented and demonstrated as an example of the application. To use it in real application systems, an interaction design, or how and for what users use the balloon display, should also be explored more.

In chapter 1, other application scenarios such as externally-actuated robots and manipulators in microgravity environments are proposed. Implementation and demonstration of such systems would be interesting.

Bibliography

- [1] Xiaoyun Ding, Sz-Chin Steven Lin, Brian Kiraly, Hongjun Yue, Sixing Li, I-Kao Chiang, Jinjie Shi, Stephen J. Benkovic, and Tony Jun Huang. On-chip manipulation of single microparticles, cells, and organisms using surface acoustic waves. *Proceedings of the National Academy of Sciences*, 109(28):11105–11109, 2012.
- [2] Ljiljana Puskar, Rudolf Tuckermann, Torsten Frosch, Jürgen Popp, Vanalysa Ly, Don McNaughton, and Bayden R. Wood. Raman acoustic levitation spectroscopy of red blood cells and plasmodium falciparum trophozoites. *Lab Chip*, 7:1125–1131, 2007.
- [3] J. K. Richard Weber, D. Scott Hampton, Dennis R. Merkley, Charles A. Rey, Mark M. Zatarski, and Paul C. Nordine. Aero-acoustic levitation: A method for containerless liquid-phase processing at high temperatures. *Review of Scientific Instruments*, 65(2):456–465, 1994.
- [4] W. J. Xie, C. D. Cao, Y. J. Lü, Z. Y. Hong, and B. Wei. Acoustic method for levitation of small living animals. *Applied Physics Letters*, 89(21):1–3, 2006.
- [5] E. H. Brandt. Levitation in Physics. *Science*, 243(4889):349–355, 1989.
- [6] Yoichi Ochiai, Kota Kumagai, Takayuki Hoshi, Jun Rekimoto, Satoshi Hasegawa, and Yoshio Hayasaki. Fairy Lights in Femtoseconds: Aerial and Volumetric Graphics Rendered by Focused Femtosecond Laser Combined with Computational Holographic Fields. *ACM Trans. Graph.*, 35(2):17:1–17:14, 2016.
- [7] Antonio Gomes, Calvin Rubens, Sean Braley, and Roel Vertegaal. Bit Drones: Towards Using 3D Nanocopter Displays as Interactive Self-

- Levitating Programmable Matter. *Proceedings of the 2016 CHI Conference on Human Factors in Computing Systems - CHI '16*, pages 770–780, 2016.
- [8] Wataru Yamada, Kazuhiro Yamada, Hiroyuki Manabe, and Daizo Ikeda. iSphere: Self-Luminous Spherical Drone Display. *Proceedings of the 30th Annual ACM Symposium on User Interface Software and Technology - UIST '17*, 2017.
- [9] Sean Braley, Calvin Rubens, Timothy Merritt, and Roel Vertegaal. Grid-drones: A self-levitating physical voxel lattice for interactive 3d surface deformations. In *Proceedings of the 31st Annual ACM Symposium on User Interface Software and Technology, UIST '18*, page 87–98, New York, NY, USA, 2018. Association for Computing Machinery.
- [10] Yuichi Tsuda, Osamu Mori, Ryu Funase, Hirotaka Sawada, Takayuki Yamamoto, Takanao Saiki, Tatsuya Endo, Katsuhide Yonekura, Hirokazu Hoshino, and Jun'ichiro Kawaguchi. Achievement of ikaros — japanese deep space solar sail demonstration mission. *Acta Astronautica*, 82(2):183 – 188, 2013. 7th IAA Symposium on Realistic Advanced Scientific Space Missions, Aosta, Italy, July 2011.
- [11] Yuki Uno, Hao Qiu, Toru Sai, Shunta Iguchi, Yota Mizutani, Takayuki Hoshi, Yoshihiro Kawahara, Yasuaki Kakehi, and Makoto Takamiya. Luciola: A millimeter-scale light-emitting particle moving in mid-air based on acoustic levitation and wireless powering. *Proc. ACM Interact. Mob. Wearable Ubiquitous Technol.*, 1(4), January 2018.
- [12] T Hoshi, M Takahashi, T Iwamoto, and H Shinoda. Noncontact Tactile Display Based on Radiation Pressure of Airborne Ultrasound. *IEEE Transactions on Haptics*, 3(3):155–165, 2010.
- [13] Tom Carter, Sue Ann Seah, Benjamin Long, Bruce Drinkwater, and Sriram Subramanian. UltraHaptics : Multi-Point Mid-Air Haptic Feedback for Touch Surfaces. *Proc. UIST 2013*, pages 505–514, 2013.
- [14] Mitsuru Ito, Daisuke Wakuda, Seki Inoue, Yasutoshi Makino, and Hiroyuki Shinoda. High spatial resolution midair tactile display using 70 khz ultrasound. In Fernando Bello, Hiroyuki Kajimoto, and Yon Visell, editors, *Hap-*

- tics: Perception, Devices, Control, and Applications*, pages 57–67, Cham, 2016. Springer International Publishing.
- [15] K Hasegawa and H Shinoda. Aerial Vibrotactile Display Based on MultiUnit Ultrasound Phased Array. *IEEE Transactions on Haptics*, page 1, 2018.
- [16] Takayuki Hoshi. Compact ultrasound device for noncontact interaction. In Anton Nijholt, Teresa Romão, and Dennis Reidsma, editors, *Advances in Computer Entertainment*, pages 502–505, Berlin, Heidelberg, 2012. Springer Berlin Heidelberg.
- [17] Seki Inoue, Yasutoshi Makino, and Hiroyuki Shinoda. Scalable Architecture for Airborne Ultrasound Tactile Display. In *AsiaHaptics*, Lecture Notes in Electrical Engineering, pages 2035–2040, Singapore, 2016. Springer.
- [18] S Suzuki, R Takahashi, M Nakajima, K Hasegawa, Y Makino, and H Shinoda. Midair Haptic Display to Human Upper Body. In *2018 57th Annual Conference of the Society of Instrument and Control Engineers of Japan (SICE)*, pages 848–853, 2018.
- [19] Shun Suzuki, Keisuke Hasegawa, Yasutoshi Makino, and Hiroyuki Shinoda. Haptic tracing of midair linear trajectories presented by ultrasound bessel beams. In Domenico Prattichizzo, Hiroyuki Shinoda, Hong Z. Tan, Emanuele Ruffaldi, and Antonio Frisoli, editors, *Haptics: Science, Technology, and Applications*, pages 209–220, Cham, 2018. Springer International Publishing.
- [20] S. Suzuki, M. Fujiwara, Y. Makino, and H. Shinoda. Midair hand guidance by an ultrasound virtual handrail. In *2019 IEEE World Haptics Conference (WHC)*, pages 271–276, July 2019.
- [21] Stratos. <https://www.ultraleap.com/product/stratos-explore/>.
- [22] T. Kamigaki, A. Noda, and H. Shinoda. Thin and flexible airborne ultrasound phased array for tactile display. In *2017 56th Annual Conference of the Society of Instrument and Control Engineers of Japan (SICE)*, pages 736–739, Sep. 2017.
- [23] Takaaki Kamigaki, Yuki Ninomiya, and Hiroyuki Shinoda. Developing electrostatically driven ultrasound transducer with high sound intensity and

- high energy conversion efficiency (in japanese). *Transactions of the Society of Instrument and Control Engineers*, 54(3):340–345, 2018.
- [24] Benjamin Long, Sue Ann Seah, Tom Carter, and Sriram Subramanian. Rendering volumetric haptic shapes in mid-air using ultrasound. *ACM Transactions on Graphics*, 33(6):1–10, 2014.
- [25] Seki Inoue, Yasutoshi Makino, and Hiroyuki Shinoda. Mid-air ultrasonic pressure control on skin by adaptive focusing. In Fernando Bello, Hiroyuki Kajimoto, and Yon Visell, editors, *Haptics: Perception, Devices, Control, and Applications*, pages 68–77, Cham, 2016. Springer International Publishing.
- [26] R. R. Whymark. Acoustic field positioning for containerless processing. *Ultrasonics*, 13(6):251–261, 1975.
- [27] D. Foresti, M. Nabavi, M. Klingauf, A. Ferrari, and D. Poulikakos. Acoustophoretic contactless transport and handling of matter in air. *Proceedings of the National Academy of Sciences*, 110(31):12549–12554, 2013.
- [28] Yoichi Ochiai, Takayuki Hoshi, and Jun Rekimoto. Three-dimensional mid-air acoustic manipulation by ultrasonic phased arrays. *PLoS ONE*, 9(5):1–5, 2014.
- [29] Charles R. P. Courtney, Bruce W. Drinkwater, Christine E. M. Demore, Sandy Cochran, Alon Grinenko, and Paul D. Wilcox. Dexterous manipulation of microparticles using Bessel-function acoustic pressure fields. *Applied Physics Letters*, 102(12):123508, 2013.
- [30] Sue Seah, Bruce Drinkwater, Tom Carter, Rob Malkin, and Sriram Subramanian. Dexterous ultrasonic levitation of millimeter-sized objects in air. *IEEE Transactions on Ultrasonics, Ferroelectrics, and Frequency Control*, 61(7):1233–1236, 2014.
- [31] Asier Marzo, Sue Ann Seah, Bruce W. Drinkwater, Deepak Ranjan Sahoo, Benjamin Long, and Sriram Subramanian. Holographic acoustic elements for manipulation of levitated objects. *Nature Communications*, 6(May):8661, 2015.
- [32] Asier Marzo and Bruce W Drinkwater. Holographic acoustic tweezers. *Pro-*

- ceedings of the National Academy of Sciences*, 116(1):84–89, 2019.
- [33] Asier Marzo, Mihai Caleap, and Bruce W. Drinkwater. Acoustic Virtual Vortices with Tunable Orbital Angular Momentum for Trapping of Mie Particles. *Physical Review Letters*, 120(4):044301, 2018.
- [34] Seki Inoue, Shinichi Mogami, Tomohiro Ichiyama, Akihito Noda, Yasutoshi Makino, and Hiroyuki Shinoda. Acoustical boundary hologram for macroscopic rigid-body levitation. *The Journal of the Acoustical Society of America*, 145(1):328–337, 2019.
- [35] Marco A B Andrade, Anne L. Bernassau, and Julio C. Adamowski. Acoustic levitation of a large solid sphere. *Applied Physics Letters*, 109(4):1–5, 2016.
- [36] Marco A. B. Andrade, F?bio T. A. Okina, Anne L. Bernassau, and Julio C. Adamowski. Acoustic levitation of an object larger than the acoustic wavelength. *The Journal of the Acoustical Society of America*, 141(6):4148–4154, 2017.
- [37] Sadayuki Ueha, Yoshiki Hashimoto, and Yoshikazu Koike. Non-contact transportation using near-field acoustic levitation. *Ultrasonics*, 38(1):26 – 32, 2000.
- [38] Yoshiki Hashimoto, Yoshikazu Koike, and Sadayuki Ueha. Acoustic levitation of planar objects using a longitudinal vibration mode. *Journal of the Acoustical Society of Japan (E)*, 16(3):189–192, 1995.
- [39] Mark T Marshall, Tom Carter, Jason Alexander, and Sriram Subramanian. Ultra-Tangibles : Creating Movable Tangible Objects on Interactive Tables. *Proc. CHI 2012*, pages 2185–2188, 2012.
- [40] Yoshiki MITSUI, Koji TANAKA, Seki INOUE, Yasutoshi MAKINO, and Hiroyuki SHINODA. Object manipulation by using airborne ultrasound phased array (in japanese). *The Proceedings of JSME annual Conference on Robotics and Mechatronics (Robomec)*, 2016:1A2–14b3, 2016.
- [41] F. Ongaro, S. Pane, S. Scheggi, and S. Misra. Design of an electromagnetic setup for independent three-dimensional control of pairs of identical and nonidentical microrobots. *IEEE Transactions on Robotics*, 35(1):174–183, Feb 2019.

- [42] Peter Berkelman, Zack Butler, and Ralph Hollis. Design of a hemispherical magnetic levitation haptic interface device. *ASME International Mechanical Engineering Congress and Exposition*, 58:483–488, 12 1996.
- [43] Jinha Lee, Rehmi Post, and Hiroshi Ishii. ZeroN: Mid-air Tangible Interaction Enabled by Computer Controlled Magnetic Levitation. In *Proceedings of the 24th Annual ACM Symposium on User Interface Software and Technology*, UIST '11, pages 327–336, New York, NY, USA, 2011. ACM.
- [44] J. E. Rush, W. K. Stephens, and E. C. Ethridge. Properties of a constricted-tube air-flow levitator. *MRS Proceedings*, 9:131, 1981.
- [45] LeRoy H Berge, William A Oran, and John M Theiss. Gas levitator having fixed levitation node for containerless processing, March 29 1983. US Patent 4,378,209.
- [46] Toshiya Yui and Tomoko Hashida. Floatio: Floating tangible user interface based on animacy perception. In *Proceedings of the 29th Annual Symposium on User Interface Software and Technology*, UIST ' 16 Adjunct, page 43–45, New York, NY, USA, 2016. Association for Computing Machinery.
- [47] Tobias Alrøe, Jonas Grann, Erik Grönvall, Marianne Graves Petersen, and Jesper L. Rasmussen. Aerial tunes: Exploring interaction qualities of mid-air displays. In *Proceedings of the 7th Nordic Conference on Human-Computer Interaction: Making Sense Through Design*, NordiCHI ' 12, page 514–523, New York, NY, USA, 2012. Association for Computing Machinery.
- [48] Aaron Becker, Robert Sandheinrich, and Timothy Bretl. Automated manipulation of spherical objects in three dimensions using a gimbaled air jet. *2009 IEEE/RSJ International Conference on Intelligent Robots and Systems, IROS 2009*, pages 781–786, 2009.
- [49] Tomoo Kamakura. *Nonlinear Acoustics - Fundamentals and Applications (in Japanese)*. CORONA Publishing, 2014.
- [50] P J Westervelt. The Theory of Steady Forces Caused by Sound Waves. *The Journal of the Acoustical Society of America*, 23(3):312–315, 1951.
- [51] Takahi Hasegawa, Tohru Kido, Takeshi Iizuka, and Chihiro Matsuoka. A general theory of Rayleigh and Langevin radiation pressures, 2000.

- [52] Louis Vessot King. On the acoustic radiation pressure on spheres. *Proceedings of the Royal Society of London. Series A - Mathematical and Physical Sciences*, 147(861):212–240, 1934.
- [53] K Yosioka and Y Kawasima. Acoustic radiation pressure on a compressible sphere. *Acta Acustica United with Acustica*, 5(3):167–173, 1955.
- [54] Wesley L Nyborg. Radiation pressure on a small rigid sphere. *The Journal of the Acoustical Society of America*, 42(5):947–952, 1967.
- [55] Takahi Hasegawa and Katuya Yosioka. Acoustic-radiation force on a solid elastic sphere. *The Journal of the Acoustical Society of America*, 46(5B):1139–1143, 1969.
- [56] Oleg A. Sapozhnikov and Michael R. Bailey. Radiation force of an arbitrary acoustic beam on an elastic sphere in a fluid. *The Journal of the Acoustical Society of America*, 133(2):661–676, 2013.
- [57] Jungwoo Lee, Kanglyeol Ha, and K. Kirk Shung. A theoretical study of the feasibility of acoustical tweezers: Ray acoustics approach. *The Journal of the Acoustical Society of America*, 117(5):3273–3280, 2005.
- [58] Jungwoo Lee and K. Kirk Shung. Radiation forces exerted on arbitrarily located sphere by acoustic tweezer. *The Journal of the Acoustical Society of America*, 120(2):1084–1094, 2006.
- [59] H. E. Bass, L. C. Sutherland, A. J. Zuckerwar, D. T. Blackstock, and D. M. Hester. Atmospheric absorption of sound: Further developments. *The Journal of the Acoustical Society of America*, 97(1):680–683, 1995.
- [60] Cgal, computational geometry algorithms library. <https://www.cgal.org>.
- [61] John Underkoffler and Hiroshi Ishii. Illuminating Light: An Optical Design Tool with a Luminous-tangible Interface. In *Proceedings of the SIGCHI Conference on Human Factors in Computing Systems*, CHI '98, pages 542–549, New York, NY, USA, 1998. ACM Press/Addison-Wesley Publishing Co.
- [62] P. MILGRAM and Fumio Kishino. A taxonomy of mixed reality visual display. *IEICE Trans. Inf. & Sys.*, D, 77(12):1321–1329, 1994.
- [63] T P Caudell. Augmented reality: An application of heads-up display tech-

- nology to manual manufacturing processes. *2011 44th Hawaii International Conference on System Sciences*, 2:659, 1992.
- [64] Matthias Harders, Gerald Bianchi, and Benjamin Knoerlein. Multimodal augmented reality in medicine. In Constantine Stephanidis, editor, *Universal Access in Human-Computer Interaction. Ambient Interaction*, pages 652–658, Berlin, Heidelberg, 2007. Springer Berlin Heidelberg.
- [65] Hsin-Kai Wu, Silvia Wen-Yu Lee, Hsin-Yi Chang, and Jyh-Chong Liang. Current status, opportunities and challenges of augmented reality in education. *Computers & Education*, 62:41 – 49, 2013.
- [66] M R Mine, J van Baar, A Grundhofer, D Rose, and B Yang. Projection-Based Augmented Reality in Disney Theme Parks. *Computer*, 45(7):32–40, 2012.
- [67] Hololens. <https://www.microsoft.com/en-us/hololens>.
- [68] B. Leibe, T. Starner, W. Ribarsky, Z. Wartell, D. Krum, B. Singletary, and L. Hodges. The perceptive workbench: toward spontaneous and natural interaction in semi-immersive virtual environments. In *Proceedings IEEE Virtual Reality 2000 (Cat. No.00CB37048)*, pages 13–20, March 2000.
- [69] Jun Rekimoto and Masanori Saitoh. Augmented surfaces: A spatially continuous work space for hybrid computing environments. In *Proceedings of the SIGCHI Conference on Human Factors in Computing Systems, CHI '99*, pages 378–385, New York, NY, USA, 1999. ACM.
- [70] Maneesh Agrawala, Andrew C Beers, Ian McDowall, Bernd Fröhlich, Mark Bolas, and Pat Hanrahan. The Two-user Responsive Workbench: Support for Collaboration Through Individual Views of a Shared Space. In *Proceedings of the 24th Annual Conference on Computer Graphics and Interactive Techniques, SIGGRAPH '97*, pages 327–332, New York, NY, USA, 1997. ACM Press/Addison-Wesley Publishing Co.
- [71] Ismo Rakkolainen, Stephen DiVerdi, Alex Olwal, Nicola Candussi, Tobias Hüllerer, Markku Laitinen, Mika Piirto, and Karri Palovuori. The Interactive FogScreen. In *ACM SIGGRAPH 2005 Emerging Technologies, SIGGRAPH '05*, New York, NY, USA, 2005. ACM.

- [72] Yutaka Tokuda, Mohd Adili Norasikin, Sriram Subramanian, and Diego Martinez Plasencia. MistForm: Adaptive Shape Changing Fog Screens. In *Proceedings of the 2017 CHI Conference on Human Factors in Computing Systems*, CHI '17, pages 4383–4395, New York, NY, USA, 2017. ACM.
- [73] S Eitoku, T Tanikawa, and Y Suzuki. Display Composed of Water Drops for Filling Space with Materialized Virtual Three-dimensional Objects. In *IEEE Virtual Reality Conference (VR 2006)*, pages 159–166, 2006.
- [74] Peter C Barnum, Srinivasa G Narasimhan, and Takeo Kanade. A Multi-layered Display with Water Drops. *ACM Trans. Graph.*, 29(4):76:1—76:7, 2010.
- [75] Masahiro Nakamura, Go Inaba, Jun Tamaoki, Kazuhito Shiratori, and Jun'ichi Hoshino. Bubble Cosmos. *ACM SIGGRAPH 2006 Emerging technologies*, page 3, 2006.
- [76] Yoichi Ochiai, Takayuki Hoshi, and Jun Rekimoto. Pixie Dust: Graphics Generated by Levitated and Animated Objects in Computational Acoustic-potential Field. *ACM Trans. Graph.*, 33(4):85:1—85:13, 2014.
- [77] Themis Omirou, Asier Marzo, Sue Ann Seah, and Sriram Subramanian. LeviPath. *Proceedings of the 33rd Annual ACM Conference on Human Factors in Computing Systems - CHI '15*, pages 309–312, 2015.
- [78] Euan Freeman, Asier Marzo, Praxitelis B. Kourtelos, Julie R. Williamson, and Stephen Brewster. Enhancing physical objects with actuated levitating particles. In *Proceedings of the 8th ACM International Symposium on Pervasive Displays*, PerDis ' 19, New York, NY, USA, 2019. Association for Computing Machinery.
- [79] T. Omirou, A. M. Perez, S. Subramanian, and A. Roudaut. Floating charts: Data plotting using free-floating acoustically levitated representations. In *2016 IEEE Symposium on 3D User Interfaces (3DUI)*, pages 187–190, March 2016.
- [80] Myroslav Bachynskyy, Viktorija Paneva, and Jörg Müller. Levicursor: Dexterous interaction with a levitating object. In *Proceedings of the 2018 ACM International Conference on Interactive Surfaces and Spaces*, ISS ' 18, page

- 253–262, New York, NY, USA, 2018. Association for Computing Machinery.
- [81] Euan Freeman, Julie Williamson, Sriram Subramanian, and Stephen Brewster. Point-and-shake: Selecting from levitating object displays. In *Proceedings of the 2018 CHI Conference on Human Factors in Computing Systems*, CHI '18, New York, NY, USA, 2018. Association for Computing Machinery.
- [82] Rafael Morales, Asier Marzo, Sriram Subramanian, and Diego Martínez. Leviprops: Animating levitated optimized fabric structures using holographic acoustic tweezers. In *Proceedings of the 32nd Annual ACM Symposium on User Interface Software and Technology*, UIST '19, page 651–661, New York, NY, USA, 2019. Association for Computing Machinery.
- [83] Ryuji Hirayama, Diego Martinez Plasencia, Nobuyuki Masuda, and Sriram Subramanian. A volumetric display for visual, tactile and audio presentation using acoustic trapping. *Nature*, 575(7782):320–323, 2019.
- [84] Wataru Yamada, Hiroyuki Manabe, and Daizo Ikeda. Zerone: Safety drone with blade-free propulsion. In *Proceedings of the 2019 CHI Conference on Human Factors in Computing Systems*, CHI '19, pages 365:1–365:8, New York, NY, USA, 2019. ACM.
- [85] Xujing Zhang, Sean Braley, Calvin Rubens, Timothy Merritt, and Roel Vertegaal. LightBee: A Self-Levitating Light Field Display for Hologrammatic Telepresence. In *Proceedings of the 2019 CHI Conference on Human Factors in Computing Systems*, CHI '19, pages 12:1–12:10, New York, NY, USA, 2019. ACM.
- [86] Hiroaki Tobita, Shigeaki Maruyama, and Takuya Kuzi. Floating Avatar: Telepresence System Using Blimps for Communication and Entertainment. In *CHI '11 Extended Abstracts on Human Factors in Computing Systems*, CHI EA '11, pages 541–550, New York, NY, USA, 2011. ACM.
- [87] Hiroaki Tobita. Aero-Screen: Blimp-based ubiquitous screen for novel digital signage and information visualization. pages 976–980, 2014.
- [88] Sue Ann Seah, Diego Martinez Plasencia, Peter D Bennett, Abhijit Karnik, Vlad Stefan Otrocol, Jarrod Knibbe, Andy Cockburn, and Sriram Subramanian. SensaBubble: A Chrono-sensory Mid-air Display of Sight and Smell.

- In *Proceedings of the SIGCHI Conference on Human Factors in Computing Systems*, CHI '14, pages 2863–2872, New York, NY, USA, 2014. ACM.
- [89] Shio Miyafuji, Toshiki Sato, Zhengqing Li, and Hideki Koike. Qoom: An Interactive Omnidirectional Ball Display. In *Proceedings of the 30th Annual ACM Symposium on User Interface Software and Technology*, UIST '17, pages 599–609, New York, NY, USA, 2017. ACM.
- [90] Hrvoje Benko, Andrew D Wilson, and Ravin Balakrishnan. Sphere: Multi-touch Interactions on a Spherical Display. In *Proceedings of the 21st Annual ACM Symposium on User Interface Software and Technology*, UIST '08, pages 77–86, New York, NY, USA, 2008. ACM.
- [91] Stefanie Kettner, Christopher Madden, and Remo Ziegler. Direct Rotational Interaction with a Spherical Projection. In *Creativity & Cognition Symposium on Interaction: Systems, Practice and Theory*, 2004.
- [92] K S Arun, T S Huang, and S D Blostein. Least-Squares Fitting of Two 3-D Point Sets. *IEEE Transactions on Pattern Analysis and Machine Intelligence*, PAMI-9(5):698–700, 1987.
- [93] TS Huang, SD Blostein, and EA Margerum. Least-squares estimation of motion parameters from 3-d point correspondences. In *Proc. IEEE Conf. Computer Vision and Pattern Recognition*, volume 10, pages 112–115, 1986.
- [94] Opencv. <https://opencv.org>.
- [95] Duane C Brown. Close-range camera calibration. *PHOTOGRAMMETRIC ENGINEERING*, 37(8):855–866, 1971.
- [96] Z Zhang. A flexible new technique for camera calibration. *IEEE Transactions on Pattern Analysis and Machine Intelligence*, 22(11):1330–1334, 2000.
- [97] Thomas R. Nelson, J. Brian Fowlkes, Jacques S. Abramowicz, and Charles C. Church. Ultrasound biosafety considerations for the practicing sonographer and sonologist. *Journal of Ultrasound in Medicine*, 28(2):139–150, 2009.
- [98] W A McNeely. Robotic graphics: a new approach to force feedback for virtual reality. In *Proceedings of IEEE Virtual Reality Annual International*

- Symposium*, pages 336–341, 1993.
- [99] Susumu Tachi, Taro Maeda, Ryokichi Hirata, and Hiroshi Hoshino. A construction method of virtual haptic space. In *Proceedings of the 4th International Conference on Artificial Reality and Tele-Existence*, pages 131–138, Tokyo, 1994.
- [100] S Nakagawara, H Kajimoto, N Kawakami, S Tachi, and I Kawabuchi. An Encounter-Type Multi-Fingered Master Hand Using Circuitous Joints. In *Proceedings of the 2005 IEEE International Conference on Robotics and Automation*, pages 2667–2672, 2005.
- [101] R Sodhi, Poupyrev, M Glisson, and a Israr. AIREAL: interactive tactile experiences in free air. *ACM Transactions on Graphics*, 32(4):134, 2013.
- [102] Yuriko Suzuki and Minoru Kobayashi. Air jet driven force feedback in virtual reality. *IEEE Computer Graphics and Applications*, 25(1):44–47, 2005.
- [103] Tao Morisaki, Ryoma Mori, Ryosuke Mori, Yasutoshi Makino, Yuta Itoh, Yuji Yamakawa, and Hiroyuki Shinoda. Hopping-pong: Changing trajectory of moving object using computational ultrasound force. In *Proceedings of the 2019 ACM International Conference on Interactive Surfaces and Spaces, ISS '19*, page 123–133, New York, NY, USA, 2019. Association for Computing Machinery.
- [104] Sueishi Tomohiro, Keisuke Hasegawa, Kouhei Okumura, Hiromasa Oku, Hiroyuki Shinoda, and Masatoshi Ishiwaka. High-speed dynamic information environment with airborne ultrasound tactile display-camera system and the calibration method (in japanese). *The Transaction of the Virtual Reality Society of Japan*, 19(2):173–183, 2014.
- [105] Kasai Takumi, Takuro Furumoto, Masahiro Fujiwara, Yasutoshi Makino, and Hiroyuki Shinoda. Direction control of a floating plane using airborne ultrasound (in japanese). In *the 24th Annual Conference of the Virtual Reality Society of Japan*, pages 1C–09, 2019.

List of Publications

Journal Article

1. Takuro Furumoto, Keisuke Hasegawa, Yasutoshi Makino, Hiroyuki Shinoda: “Three-Dimensional Manipulation of a Spherical Object Using Airborne Ultrasound Plane Waves,” *IEEE Robotics and Automation Letters*, pp. 81-88, Volume: 4, Issue: 1, Jan. 2019, DOI:10.1109/LRA.2018.2880330.

International Referred Conference

1. Takuro Furumoto, Takaaki Kamigaki, Mitsuru Ito, Masahiro Fujiwara, Yasutoshi Makino, Hiroyuki Shinoda, ”Three-dimensional Interaction Technique Using an Acoustically Manipulated Balloon”, *SIGGRAPH ASIA '19 Emerging Technologies*, Brisbane, Australia, Nov. 17-20, 2019.
2. Takuro Furumoto, Masahiro Fujiwara, Yasutoshi Makino, Hiroyuki Shinoda, “BaLuna: Floating Balloon Screen Manipulated Using Ultrasound” , the 26th IEEE Conference on Virtual Reality and 3D User Interfaces, 221, Osaka, Japan, Mar. 22-27, 2019.
3. Takuro Furumoto, Yutaro Toide, Masahiro Fujiwara, Yasutoshi Makino and Hiroyuki Shinoda, “Encounter-type Haptic Feedback System Using an Acoustically Manipulated Floating Object,” *Asia Haptics 2018*, Incheon, Korea, Nov. 14-16, 2018.

Domestic Conference

1. 笠井 匠, 古本 拓朗, 藤原 正浩, 牧野 泰才, 篠田 裕之, “空中超音波による浮遊平面の方向制御,” 第 24 回バーチャルリアリティ学会大会, 1C-09, 東京大学本郷キャンパス, 東京, Sep. 11-13, 2019.
2. 古本 拓朗, 牧野 泰才, 篠田 裕之, “3次元位置制御可能なバルーン型ディスプレイ,” 第 23 回バーチャルリアリティ学会大会, 33B-1, 東北大学 青葉山新キャンパス, 仙台, Sep. 19-21, 2018.
3. 砥出悠太郎, 古本拓朗, 藤原正浩, 牧野 泰才, 篠田 裕之, “軽量浮遊物体による遭遇型接触感提示,” 第 23 回バーチャルリアリティ学会大会, 東北大学 青葉山新キャンパス, 仙台, Sep. 19-21, 2018.
4. 古本拓朗, 長谷川圭介, 牧野泰才, 篠田裕之, “空中平面超音波による浮遊物体の動的 position 制御,” 第 18 回システムインテグレーション部門講演会論文集, pp. 1984-1987, 仙台, Dec. 20-22, 2017.
5. 古本 拓朗, 長谷川 圭介, 牧野 泰才, 篠田 裕之, “空中超音波による浮遊物体の運動制御,” 第 22 回バーチャルリアリティ学会大会, 1E4-05, 徳島大学 常三島キャンパス, 徳島, Sep. 27-29, 2017.